CZECH TECHNICAL UNIVERSITY IN PRAGUE

Faculty of Nuclear Sciences and Physical Engineering

Department of Physics

Master's Thesis

Photoproduction of muon pairs in Pb-Pb collisions with ALICE experiment

Bc. Tomáš Herman

Supervisor: doc. Jesús Guillermo Contreras Nuño, Ph.D.

Prague, 2019

ČESKÉ VYSOKÉ UČENÍ TECHNICKÉ
V PRAZE
Fakulta jaderná a fyzikálně inženýrská
Katedra fyziky

Diplomová práce

Fotoprodukce mionových párů v Pb-Pb srážkách na experimentu ALICE

Bc. Tomáš Herman

Vedoucí práce: doc. Jesús Guillermo Contreras Nuño, Ph.D.

Praha, 2019

ČESKÉ VYSOKÉ UČENÍ TECHNICKÉ V PRAZE
FAKULTA JADERNÁ A FYZIKÁLNĚ INŽENÝRSKÁ
PRAHA 1 - STARÉ MĚSTO, BŘEHOVÁ 7 - PSČ 115 19

Katedra: fyziky *Akademický rok:* 2018/2019

ZADÁNÍ DIPLOMOVÉ PRÁCE

Student: Bc. Tomáš Herman

Studijní program: Aplikace přírodních věd

Obor: Experimentální jaderná a částicová fyzika

Název práce: (česky) Fotoprodukce mionových párů v Pb-Pb srážkách na experimentu ALICE

Název práce: (anglicky) Photoproduction of muon pairs in Pb-Pb collisions with ALICE experiment

Pokyny pro vypracování:

1) Zpracování rešerše o fotoprodukci mionových párů
2) Měření fotoprodukce mionových párů na ALICE v datech z Run 2 urychlovače LHC

Doporučená literatura:

[1] J. G. Contreras, J. D. Tapia Takaki: Ultra-peripheral heavy-ion collisions at the LHC, International Journal of Modern Physics A 30(8), 1542012 (2015)

[2] J. Adam, et al.: Measurement of an excess in the yield of J/Psi at very low pT in Pb–Pb collisions at sNN=2.76 TeV, Physical Review Letters 116(22) (2016)

[3] V. Khachatryan, et al.: Coherent J/Psi photoproduction in ultra-peripheral PbPb collisions at sNN = 2.76 TeV with the CMS experiment, Physics Letters B 772, 489–511 (2017)

[4] S. Afanasiev, et al.: Photoproduction of J/Psi and of high mass e+e- in ultra-peripheral Au + Au collisions at sNN=200GeV, Physics Letters B 679(4), 321–329 (2009)

Jméno a pracoviště vedoucího diplomové práce:

doc. Jesús Guillermo Contreras Nuño, Ph.D., Katedra fyziky, Fakulta jaderná a fyzikálně inženýrská ČVUT v Praze

Datum zadání diplomové práce: 22.10.2018

Termín odevzdání diplomové práce: 06.05.2019

Doba platnosti zadání je dva roky od data zadání.

....
garant oboru

....
vedoucí katedry *děkan*

ČESKÉ VYSOKÉ UČENÍ TECHNICKÉ V PRAZE
Fakulta jaderná a fyzikálně inženýrská
-1-

V Praze dne 22.10.2018

Prohlášení:

Prohlašuji, že jsem svou diplomovou práci vypracoval samostatně a použil jsem pouze podklady (literaturu, projekty, SW atd.) uvedené v přiloženém seznamu.

Nemám závažný důvod proti použití tohoto školního díla ve smyslu § 60 Zákona č.121/2000 Sb., o právu autorském, o právech souvisejících s právem autorským a o změně některých zákonů (autorský zákon).

V Praze dne ....

Tomáš Herman

Acknowledgments

I would like to express my deepest gratitude to my supervisor doc. Jesús Guillermo Contreras Nuño, Ph.D. for his invaluable guidance, advice and experience, passion for science and language corrections. I would also like to thank Mgr. Michal Broz, Ph.D. for providing the analysed nanoAOD data sets. Finally, a special thanks goes to my parents and my girlfriend Pavlínka for their never ending love.

Title:
Photoproduction of muon pairs in Pb-Pb collisions with ALICE experiment

Author: Tomáš Herman

Specialization: Experimental Physics and Particle Physics

Sort of project: Master's thesis

Supervisor: doc. Jesús Guillermo Contreras Nuño, Ph.D., Department of Physics, Faculty of Nuclear Sciences and Physical Engineering, Czech Technical University in Prague

Consultant: ———

Abstract: The phenomena associated with the proton and nucleus structure at high energies (small Bjorken x), i.e., gluon saturation and nuclear shadowing, can be studied experimentally by measuring cross sections of processes sensitive to their gluon distribution functions.

One of these processes is the coherent photoproduction of a J/ψ vector meson. One of the possible ways to theoretically describe this process is the colour dipole model. Experimentally it can be studied in ultra-peripheral collisions (UPC) where hadronic interactions are suppressed due to the impact parameter being larger than the sum of radii of the colliding particles.

Ultra-peripheral collisions of Pb ions at the LHC are capable of probing the gluon distribution function at very low Bjorken x. ALICE measurement of the cross section for J/ψ photoproduction in Pb-Pb UPC is presented. The results indicate the presence of moderate nuclear gluon shadowing.

Key words: ALICE, J/ψ, photoproduction, ultra-peripheral collisions, colour dipole model

Název práce:
Fotoprodukce mionových párů v Pb-Pb srážkách na experimentu ALICE

Autor: Tomáš Herman

Obor: Experimentální jaderná a částicová fyzika

Druh práce: Diplomová práce

Vedoucí práce: doc. Jesús Guillermo Contreras Nuño, Ph.D., Katedra fyziky, Fakulta jaderná a fyzikálně inženýrská, České vysoké učení technické v Praze

Konzultant: ———

Abstrakt: Jevy spojené se strukturou protonů a jader při vysokých energiích (nízkých Bjorkenových x), tj. gluonová saturace a jaderné stínění, mohou být experimentálně studovány měřením účinných průřezů procesů citlivých na jejich gluonové distribuční funkce.

Jedním z těchto procesů je koherentní fotoprodukce vektorového mezonu J/ψ. Jednou z možností, jak teoreticky popsat tento proces, je použít barevný dipólový model. Experimentálně jej lze studovat v ultra-periferálních srážkách (UPC), kde dochází k potlačení hadronové interakce kvůli tomu, že srážkový parametr je větší než suma poloměrů srážejících se částic.

Ultra-periferální srážky Pb iontů na LHC jsou schopny zkoumat gluonové distribuční funkce při velmi nízkých Bjorkenových x. V práci je prezentováno měření účinného průřezu pro fotoprodukci J/ψ v Pb-Pb UPC pomocí ALICE. Výsledky naznačují přítomnost mírného gluonového stínění.

Klíčová slova: ALICE, J/ψ, fotoprodukce, ultra-periferální srážky, barevný dipólový model

Contents

List of Figures

List of Tables

Preface

The structure of the proton is an actively researched topic. At low energies the proton seems to be composed from the three valence quarks (uud). However, when studied with a high energy probe (at low Bjorken x), the proton structure seems to be dominated by sea quarks and predominantly gluons. The number of gluons is observed to rise very steeply, but this growth cannot go indefinitely as it would the unitarity of the cross section. At some point gluon recombination is expected to start to play a role and stop the rise. This process is predicted by QCD and it is called saturation ,but it has not yet been conclusively observed. Moreover, when the nucleon (proton) structure is studied within a nucleus, it is found to be different than that of a single free nucleon. This phenomenon is called nuclear shadowing. All of these topics are introduced in Chapter 1.

It is possible to study the proton and nucleus structure with high energy probes in ultra-peripheral collisions. These are collisions where the strong interaction is suppressed by a large impact parameter and the colliding particles interact via an exchange of a quasi-real photon. Ultra-peripheral collisions are discussed in Chapter 2.

One process of interest in ultra-peripheral collisions is called vector meson photoproduction. One of the approaches to describe the cross section for such processes is called the colour dipole model. It treats the photon in the interaction as if it fluctuates into a quark-antiquark pair which then interacts with the target. Two papers using this model to predict vector meson photoproduction cross sections at the LHC are reviewed in Chapter 3.

To be able to measure the vector meson photoproduction cross section at small Bjorken x it is necessary to accelerate particles at high energies and measure the products of their ultra-peripheral collisions. To achieve this a large experimental infrastructure is necessary. The ALICE detector at the CERN Large Hadron Collider which is capable of such measurements is presented in Chapter 4.

The ALICE measurement of coherent J/ψ photoproduction cross section in Pb-Pb ultra-peripheral collisions at a centre-of-mass energy per nucleon pair $\sqrt{s_{NN}} = 2.76$ TeV is reviewed in Chapter 5.

The analysis procedure and the published results of coherent J/ψ photoproduction cross section measured in the forward rapidity region by ALICE in Pb-Pb ultra-peripheral collisions at a centre-of-mass energy per nucleon pair $\sqrt{s_{NN}} = 5.02$ TeV during the LHC Run 2 with data from 2015 and 2018 is discussed in Chapter 6. While Chapters 1 to 5 are an overview of the current state of the art in the field, Chapter 6 contains my own contribution to a measurement performed within the ALICE collaboration.

Chapter 1

The structure of proton

The most important experiment for understanding the structure of a proton is without a doubt deep-inelastic scattering (DIS) which can be regarded as the successor of the famous Rutherford experiment. As was the scattering of alpha particles on gold crucial for the understanding of the inner structure of the atom and establishing the idea of atomic nucleus, so was the scattering of leptons on proton essential in the formulation of the parton model and proving the existence of quarks. This chapter is drawing information from QCD lectures by Jana Bielčíková and the textbook "Quarks, partons and Quantum Chromodynamics" [1] by Jiří Chýla.

1.1 Kinematics

To describe lepton-proton scattering, the following definition will be used

$$l(k) + p(P) \rightarrow l'(k') + X(P'), \tag{1.1}$$

where l and l' can be electron, muon or their neutrinos, p is a proton, X is any hadronic final state allowed by conservation laws and k, p, k', P' are four-momenta of their respective states. A diagram of electron-proton DIS at the lowest order can be seen in Fig. 1.1.

Depending on the mediating particle there are two types of processes:

- Neutral current, where the lepton did not change ($l = l'$) and the mediator is either a photon or the Z boson.
- Charged current, where the initial (l) and final (l') lepton states differ by one unit of elementary electric charge and the mediator is the $W^{\pm}$ boson.

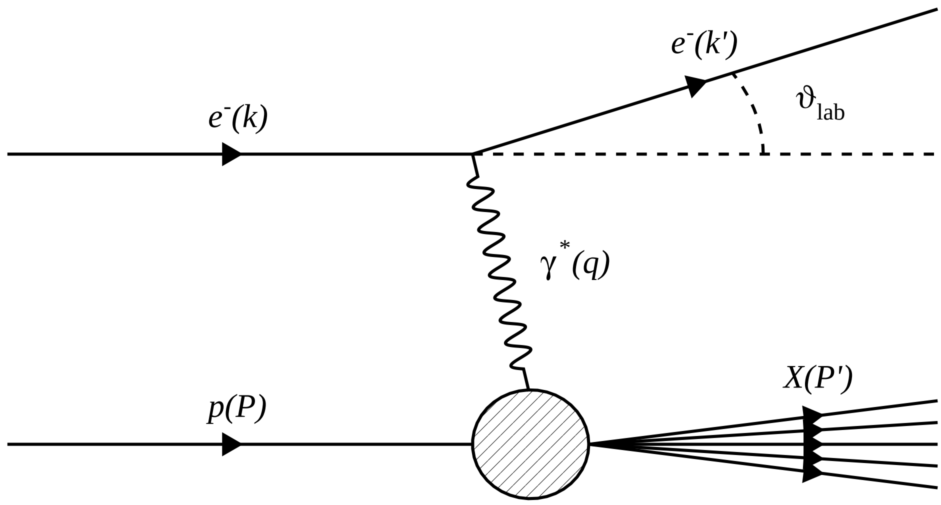

Figure 1.1: Diagram of deep-inelastic scattering at lowest order. An electron e^- interacts with a proton p via the exchange of a virtual photon γ^*, resulting in an electron e^- and a final hadronic state X.

To describe both of these processes the following variables are commonly used:

$$s \equiv (k+P)^2, \tag{1.2}$$

$$Q^2 \equiv -q^2 \equiv -(k-k')^2, \tag{1.3}$$

$$W^2 \equiv (q+P)^2, \tag{1.4}$$

$$x \equiv \frac{Q^2}{2Pq}. \tag{1.5}$$

$$y \equiv \frac{qP}{kP} \tag{1.6}$$

All of the above mentioned variables are relativistic invariants. The s is the Mandelstam variable and it is the centre-of-mass energy squared. The Q^2 is the virtuality of the exchanged particle, where the q is the four-momenta transferred in the collision. The W is the invariant mass of the hadronic final state X. The x describes the elasticity of the process, for values of $0 < x < 1$ the process is inelastic and for $x = 1$ the process is elastic. Later, the x will also gain the meaning of the fraction of the proton momentum carried by a constituent parton. The y corresponds to the fraction of energy lost by the incoming lepton.

To describe a DIS process at a given centre-of-mass energy only two other of the five variables defined above are necessary as the rest can be derived from them. Usually the pairs (x, y) or (x, Q^2) are used most often for describing the differential cross section.

For elastic scattering the variables x and W^2 are fixed to $x = 1$ and $W^2 = M_p^2$, where M_p is the proton mass. While for deep-inelastic scattering Q^2 and Pq are required to be large with respect to M_p.

An important limit, which is used for computation in DIS, is the Bjorken limit. For this limit one considers that Q^2 and Pq go to infinity, while their ratio $x = Q^2/Pq$ remains constant. In this approximation, the parton model can emerge and the x variable gains the meaning of the fraction of the proton momentum carried by the constituent parton.

1.2 Elastic scattering of an electron on a pointlike proton

When considering the elastic scattering of an electron (with negligible mass m) on a pointlike proton (with mass M), the cross section is

$$\frac{\mathrm{d}\sigma}{\mathrm{d}Q^2} = \frac{2\pi\alpha^2}{Q^4}\left[1 + (1-y)^2 - \frac{M^2 y}{kp}\right]. \tag{1.7}$$

When transformed to the laboratory frame, the cross section takes form

$$\frac{\mathrm{d}\sigma}{\mathrm{d}\Omega_{\mathrm{lab}}} = \frac{\alpha^2\cos^2(\vartheta_{\mathrm{lab}}/2)}{4E^2\sin^4(\vartheta_{\mathrm{lab}}/2)}\frac{E'}{E}\left[1 + \frac{Q^2}{2M^2}\tan^2\left(\frac{\vartheta_{\mathrm{lab}}}{2}\right)\right] \xrightarrow[M\to\infty]{} \frac{\alpha^2\cos^2(\vartheta_{\mathrm{lab}}/2)}{4E^2\sin^4(\vartheta_{\mathrm{lab}}/2)} = \sigma_{\mathrm{Mott}}, \tag{1.8}$$

where σ_{Mott} is a cross section for scattering of an electron on a proton with infinite mass, the factor $E'/E = 1 - Q^2/2ME < 1$ describes the the proton recoil. The Mott cross section is the relativistic generalisation of the Rutherford formula, except for the factor $\cos^2(\vartheta_{\mathrm{lab}}/2)$ which rises from taking into account the spin interaction for spin 1/2 fermions.

The cross section can also be computed for the case of a pointlike proton with spin 0. The generalised cross section takes the form

$$\frac{\mathrm{d}\sigma}{\mathrm{d}Q^2} = \frac{4\pi\alpha^2}{Q^4}\left[(1-y)^2 + \varepsilon\frac{y^2}{2} - \frac{M^2 y}{kp}\right] \xrightarrow[s\to\infty]{y\to 0} \frac{4\pi\alpha^2}{Q^4}, \tag{1.9}$$

where $\varepsilon = 1$ is for a pointlike fermion with spin 1/2 and $\varepsilon = 0$ is for a pointlike boson with spin 0. Therefore, to be able to differentiate between a spin 1/2 and spin 0 target, y has to be large.

1.3 Elastic scattering of an electron on a real proton

When rewriting the interaction for elastic scattering of an electron on a real proton, one has to take into account the structure of the proton and how it will affect the interaction. This is done via the elastic electromagnetic form factors $F_1(Q^2)$ and $F_2(Q^2)$. The cross section for this process is called the Rosenbluth formula

$$\frac{d\sigma}{d\Omega_{\text{lab}}} = \sigma_{\text{Mott}} \frac{E'}{E} \left\{ F_1^2(Q^2) + \frac{Q^2}{4M^2} \left[2\tan^2\left(\frac{\vartheta_{\text{lab}}}{2}\right) \left(F_1(Q^2) + \kappa F_2(Q^2)\right)^2 + \kappa F_2^2(Q^2) \right] \right\}. \tag{1.10}$$

For zero transferred four-momentum in the collision the electromagnetic form factors take values $F_1(0) = F_2(0) = 1$ and $\kappa = 1.793$ corresponds to the pointlike proton anomalous magnetic moment.

Instead of the form factors $F_1(Q^2)$ and $F_2(Q^2)$ there are often defined the electric $G_E(Q^2)$ and magnetic $G_M(Q^2)$ form factors as

$$G_E(Q^2) \equiv F_1(Q^2) - \frac{Q^2}{4M^2} \kappa F_2(Q^2) \Rightarrow G_E(0) = 1, \tag{1.11}$$

$$G_M(Q^2) \equiv F_1(Q^2) + \kappa F_2(Q^2) \Rightarrow G_M(0) = 1 + \kappa = \mu_p. \tag{1.12}$$

With these the cross section takes the form

$$\frac{d\sigma}{d\Omega_{\text{lab}}} = \sigma_{\text{Mott}} \frac{E'}{E} \left[\frac{G_E^2(Q^2) + \tau G_M^2(Q^2)}{1+\tau} + 2\tau G_M^2(Q^2) \tan^2\left(\frac{\vartheta_{\text{lab}}}{2}\right) \right], \tag{1.13}$$

where

$$\tau \equiv \frac{Q^2}{4M^2}. \tag{1.14}$$

1.4 Deep-inelastic scattering of an electron on a proton

Unlike for elastic scattering where the final state is uniquely described by one variable, for deep-inelastic scattering of an electron on a proton, two independent variables are needed to uniquely describe the final state. Therefore the derived cross section is double differential

$$\frac{d^2\sigma}{dx\,dQ^2} = \frac{4\pi\alpha^2}{Q^4} \left[\left(1 - y - \frac{M^2xy}{s}\right) \frac{F_2(x,Q^2)}{x} + \frac{1}{2} y^2 2F_1(x,Q^2) \right] \xrightarrow[s\to\infty]{y\to 0} \frac{4\pi\alpha^2}{Q^4} \frac{F_2(x,Q^2)}{x}. \tag{1.15}$$

When computed in the laboratory frame one gets

$$\frac{\mathrm{d}^2\sigma}{\mathrm{d}E'\,\mathrm{d}\Omega_{\mathrm{lab}}} = \sigma_{\mathrm{Mott}}\frac{1}{M}\left[W_2(x,Q^2) + 2W_1(x,Q^2)\tan^2\left(\frac{\vartheta_{\mathrm{lab}}}{2}\right)\right]. \tag{1.16}$$

The functions $F_i(x,Q^2)$ or $W_i(x,Q^2)$ are called inelastic electromagnetic form factors or structure functions and they are linked with the following relations

$$F_1 = W_1, \tag{1.17}$$

$$F_2 = \frac{E-E'}{M}W_2. \tag{1.18}$$

The fact that they are functions of x and Q^2 is a matter of convention as any two variables from x, y, Q^2 could be used to describe them.

When x is taken to correspond to the elastic cross section, i.e. $x = 1$, the following relations between the elastic and inelastic form factors can be derived

$$2F_1^{\mathrm{inel}}\left(x=1,Q^2\right) = \left(F_1^{\mathrm{el}}\left(Q^2\right) + \kappa F_2^{\mathrm{el}}\left(Q^2\right)\right)^2, \tag{1.19}$$

$$F_2^{\mathrm{inel}}\left(x=1,Q^2\right) = \left(F_1^{\mathrm{el}}\left(Q^2\right)\right)^2 + \frac{\kappa^2 Q^2}{4M^2}\left(F_2^{\mathrm{el}}\left(Q^2\right)\right)^2. \tag{1.20}$$

1.5 Results on the elastic electron-nucleus and electron-proton scattering

A group of physicists at the Stanford University, lead by Robert Hofstadter, conducted a series of systematic studies on nucleus and nucleon structure using an electron beam accelerated with a linear accelerator (Linac). The results they published earned Hofstadter a Nobel prize for physics in 1961.

The results of electron scattering on nuclei showed that they have finite size, in the order of several fermi, and that they do not have a sharp edge. The group continued with measuring the electron-proton scattering and the results proved that proton is not pointlike and that it has radius of approximately one fermi.

The success of the Stanford group lead to the foundation of the Stanford Linear Accelerator Centre (SLAC) which possessed a new Linac capable of delivering electrons with much higher energies. The group composed of physicists from SLAC and MIT intended to focus predominantly on further studies of the elastic scattering and the quasi-elastic scattering, i.e. the production of resonances. Only for completeness of their program they also looked into the inelastic continuum which was not accessible for the group lead by Hofstadter in the previous experiment. In hindsight this research turned out to be the breakthrough which lead to the formulation of the parton model.

The first results on elastic electron-proton scattering confirmed the results obtained by Hofstadter, showing the rapid decrease of the elastic form factors with increasing Q^2.

1.6 Results on the inelastic electron-proton scattering

The first results on inelastic electron-proton scattering hinted at the possibility of pointlike constituents within the proton. But this idea was at that time rejected by the majority of scientists. Even though the static quark model was already formulated, the quarks were thought to be only mathematical constructs and nobody expected them to play any role in high energy scattering experiments.

There were very few predictions for the behaviour of the inelastic form factors at that time. However, Bjorken derived a sum rule for the proton and neutron structure functions

$$\int \frac{\mathrm{d}x}{x} \left[F_2^p(x,Q^2) + F_2^n(x,Q^2)\right] \geq \frac{1}{2} \tag{1.21}$$

and Callan and Gross derived a similar one

$$\int \mathrm{d}x \left[F_2^p(x,Q^2) + F_2^n(x,Q^2)\right] \leq \frac{1}{2}. \tag{1.22}$$

Both of them assumed the limit of $Q^2 \to \infty$.

The most important question of the time was to determine the behaviour of the structure functions $F_i(x,Q^2)$ with Q^2. Bjorken suggested that instead of them going to zero very fast with increasing Q^2, as in the case of elastic structure functions, they would remain a nonzero functions of x. This hypothesis is known as Bjorken scaling.

The new data supported this hypothesis as the structure functions were changing only very slowly with increasing Q^2. But more precise measurements conducted later showed that his scaling is only approximate and for $Q^2 \to \infty$ the structure functions $F_i(x,Q^2)$ would go to zero, however they would do so very slowly. The approximate scaling behaviour of the structure function $F_2(x,Q^2)$ can be seen in Fig. 1.2 in the lower part of the figure, where the values of x correspond to the values of x which were accessible for the SLAC-MIT group at that time. The behaviour of the structure functions at very low x will be discussed later.

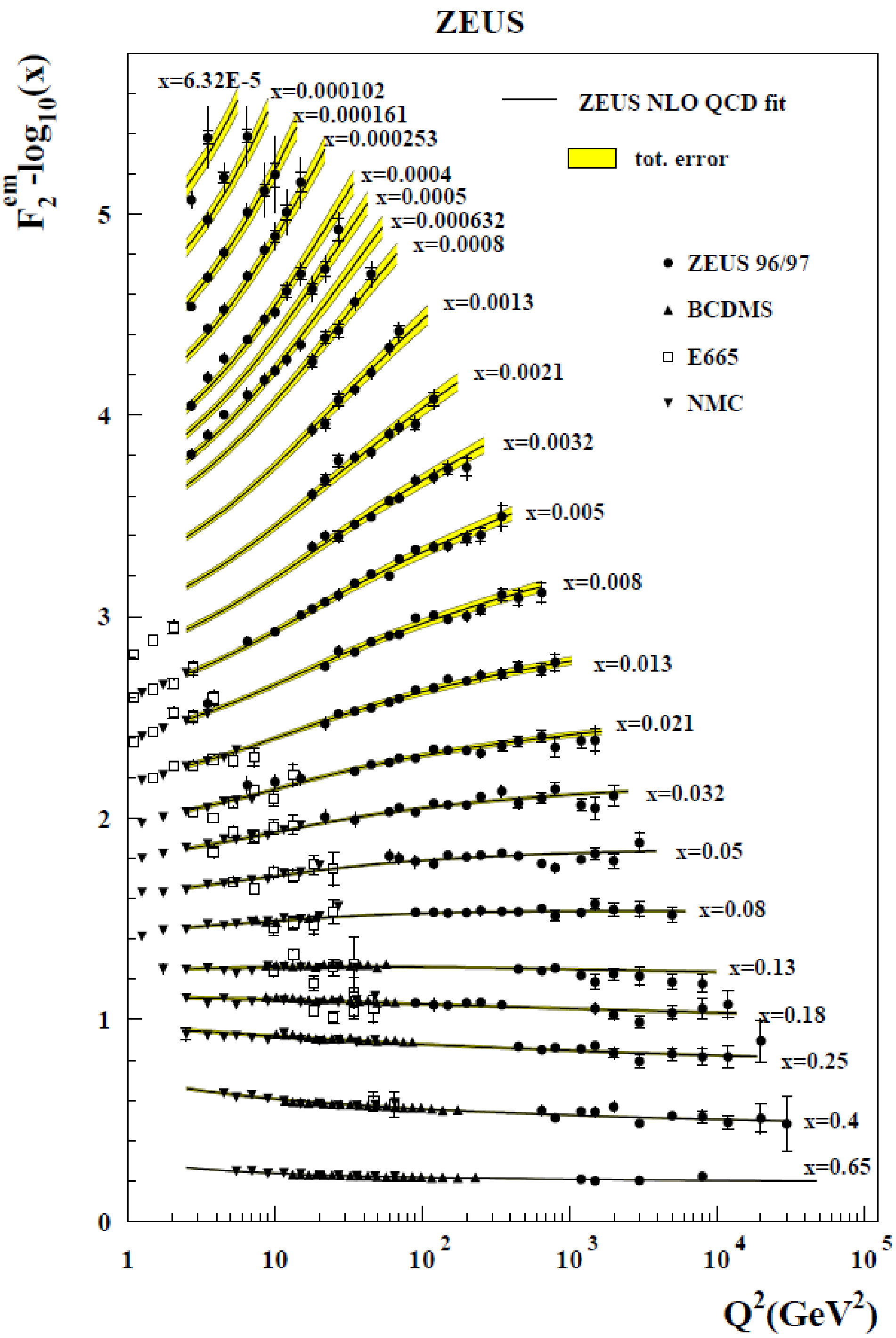

Figure 1.2: Dependence of the structure function $F_2(x,Q^2)$ on Q^2 for different values of x. The NLO QCD fit is compared to data measured by the ZEUS collaboration and the fixed target data measured at DESY [2].

1.7 The parton model

Based on these results and using the Bjorken limit of the infinite momentum frame Feynman first formulated the parton model. He stated that for deep-inelastic collisions the electron instead of scattering coherently on the whole proton scatters on its constituents as on quasi-free pointlike particles. The key component of the parton model is the infinite momentum frame. Because in this frame any transverse momentum of the partons inside the proton can be neglected as well as the masses of the partons. And the parton four-momentum can be written as $p = xP$, where x corresponds to the fraction of the proton momentum P carried by the parton. It is at this point that the momentum conservation in the collision shows that this x corresponds to the x defined in Eq. 1.5.

Feynman used the idea of parton distribution functions (PDF) to describe the structure function $F_2(x)$, now only dependent on x as we are in the infinite momentum frame and using the approximate scaling hypothesis

$$F_2(x) = x\sum_i e_i^2 f_i(x), \tag{1.23}$$

where e_i is the charge of the parton i and $f_i(x)$ is the probability of finding the parton i with momentum fraction x inside the proton. When assuming a simple model for the behaviour of the PDF one can assume the probability $P(N)$ of having N partons inside the proton and each of them carrying momentum fraction $x = 1/N$. With this in mind one can write

$$\int_0^1 \mathrm{d}x F_2(x) = \sum_N P(N) \frac{\langle \sum_{i=1}^N e_i^2 \rangle}{N}, \tag{1.24}$$

thus giving the integral on the left side the meaning of the mean square charge per parton in the proton. When this value is measured it is 0.17 ± 0.01, which is about half the value one would expect from the static quark model $1/3 = (4/9 + 4/9 + 1/9)/3$. This implies that there are some other neutral partons present in the proton. These were later identified as gluons of the Quantum Chromodynamics (QCD). Another prove for the existence of gluons can be found when looking into the momentum carried by the constituent quarks. The integral

$$\int_0^1 x\sum_i f_i(x)\,\mathrm{d}x, \tag{1.25}$$

summing over all valence and sea quarks in the proton, i.e. $(u,d,s,c$ and their corresponding antiquarks), gives the fraction of the proton momentum carried by these quarks. This value is measured to be approximately 0.5 serving as another proof for the existence of electrically neutral gluons within the proton.

In the limit of infinite collision energy the function $F_1(x,Q^2)$ is zero and therefore only the $F_2(x,Q^2)$ is measured but at finite energies it also possible to measure $F_1(x,Q^2)$. When this was done, the results were in good agreement with the Callan-Gross relation

$$F_2(x) = 2xF_1(x), \tag{1.26}$$

which proved that the partons are fermions with spin $1/2$. This is one of the measurements which brought up the idea of connecting partons with the quarks from the additive quark model. Indeed the partons and quarks are closely related therefore the names are often freely interchanged, however they are concepts based on different assumptions and therefore are not identical.

Note that the PDF values are not predicted by the parton model, however once extracted from experimental data they can be used to make predictions.

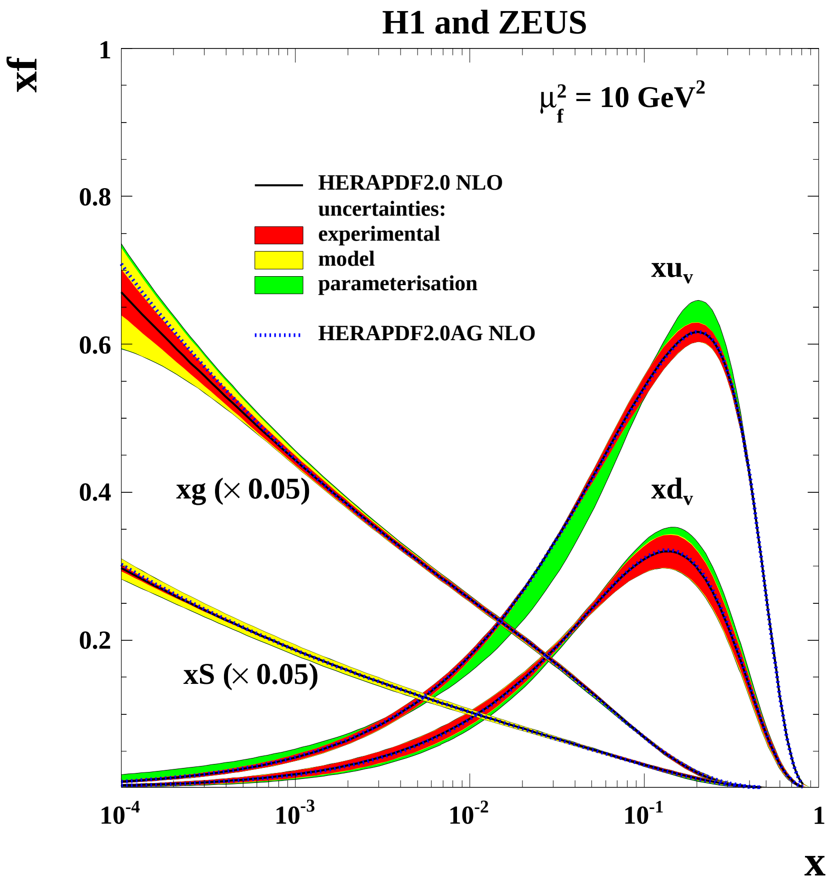

Figure 1.3: The parton distribution functions $xu_v, xd_v, xS = 2x(\bar{U}+\bar{D})$ and xg of HERAPDF2.0 NLO at $Q^2 = 10\ \mathrm{GeV}^2$ by the H1 and ZEUS collaboration at DESY. The gluon and sea distributions are scaled down by a factor of 20 [3].

1.8 Saturation

So far only the quark PDF were discussed but as hinted by several measurements there are also contributions from gluons. These cannot be measured directly with photons as they are electrically neutral, however they can be measured by their contribution to the scaling violation. This measurement was done by the H1 and ZEUS collaboration at DESY and their results can be seen in Fig. 1.3.

The interpretation of the observation of sea quarks and gluons within the proton is as follows. For probe with small energy, the proton seems to be composed of three valence quarks held together by a static gluon potential. This is visible in Fig. 1.3 for $x \approx 0.1$. However, a probe with high energy does not see a static quark potential but can resolve the exchanged virtual quarks which can also split into virtual quark antiquark pairs or radiate other virtual gluons. This idea is demonstrated in the diagram in Fig. 1.4. And the resulting image of the proton then corresponds to the low x region in Fig. 1.3.

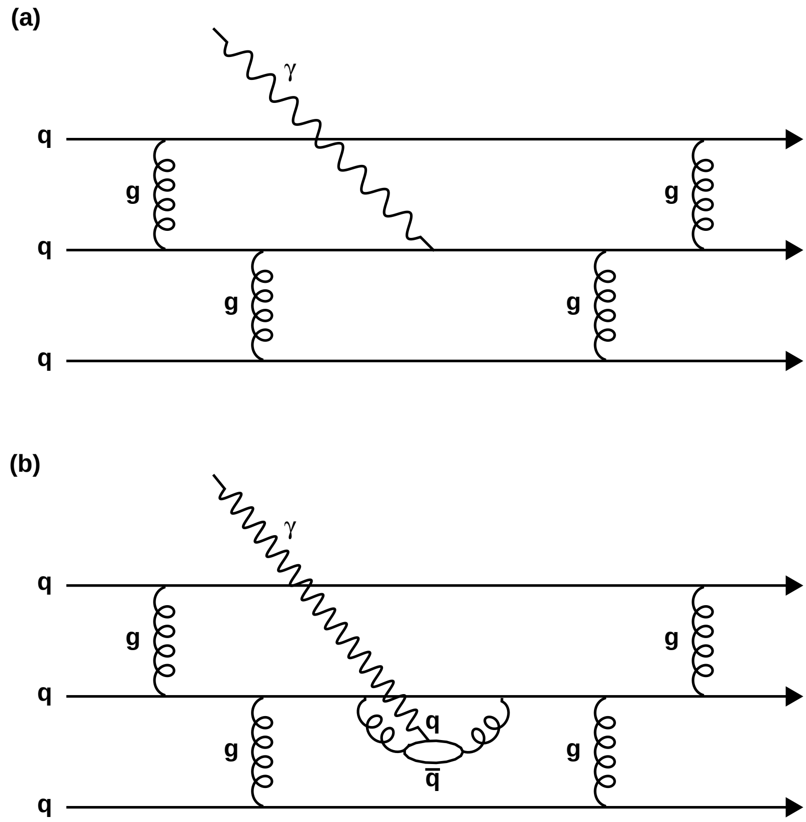

Figure 1.4: A schematic diagram of the difference in the structure of the proton as observed by a lower-energy probe (a) and a higher-energy probe (b).

The splitting and the radiating of gluons cannot go indefinitely, as at some point the density of the partons inside the proton would be so high that a process of gluon recombination would start to play a significant role and a balanced state will be reached. This state is called saturation and it is predicted by QCD, however it has not yet been conclusively observed.

1.9 Nuclear shadowing

When examining the the structure functions for nuclei, one can define the ratio $R^A_{F_2}(x,Q^2)$ of the nucleus structure function $F_2^A(x,Q^2)$ and the structure functions of its constituents $AF_2^{\text{nucleon}}(x,Q^2)$

$$R^A_{F_2}(x,Q^2) = \frac{F_2^A(x,Q^2)}{AF_2^{\text{nucleon}}(x,Q^2)}, \tag{1.27}$$

where A is the atomic mass number of the nucleus and $F_2^{\text{nucleon}}(x,Q^2)$ is taken as the average nucleon structure function from deuteron

$$F_2^{\text{nucleon}}(x,Q^2) = \frac{F_2^{\text{deuterium}}(x,Q^2)}{2}, \tag{1.28}$$

neglecting any nuclear effects there. This ratio can be measured and it has been shown that the nucleus is in fact not just a simple sum of its constituent nucleons. For the region of $x \lesssim 0.1$ this ratio turns out to be $R^A_{F_2} < 1$. This phenomenon is called nuclear shadowing.

The available experimental data show that shadowing decreases with increasing Q^2 and increases with increasing atomic number of the nucleus. Shadowing also increases with decreasing x, therefore for measurements of very low x structure functions of high mass nucleus one would expect very high shadowing. However, the available data show a mild decrease of shadowing which could be compatible with the onset of saturation occurring in the nucleus at higher x than in the deuteron. The expected dependence of the saturation scale on A and x can be seen in Fig. 1.5.

Commonly, the underlying reason causing nuclear shadowing is associated with multiple scattering of the virtual photon inside the nucleus. This results in a modification of the nucleus structure function with regard to the virtual photon-nucleus cross section [4]

$$F_A^2(x,Q^2) = \frac{Q^2(1-x)}{4\pi^2\alpha_{\text{em}}}\sigma_{\gamma^*-A}, \tag{1.29}$$

where α_{em} is the electromagnetic coupling constant.

The phenomenological handling of the multiple scattering of the photon inside the nucleus varies depending on the applied model. For example, the dipole model gives the hadronic part of the photon's wave function a partonic interpretation. The vector dominance model just takes a superposition of wave functions of hadrons with the photon quantum numbers. These models are further discussed in Sec. 2.4 and the dipole model is reviewed in Chapter 3. Moreover, what is seen as multiple scattering in the rest frame of the nucleus is seen as recombination in the infinite momentum frame, i.e. the saturation principle discussed in Sec. 1.8.

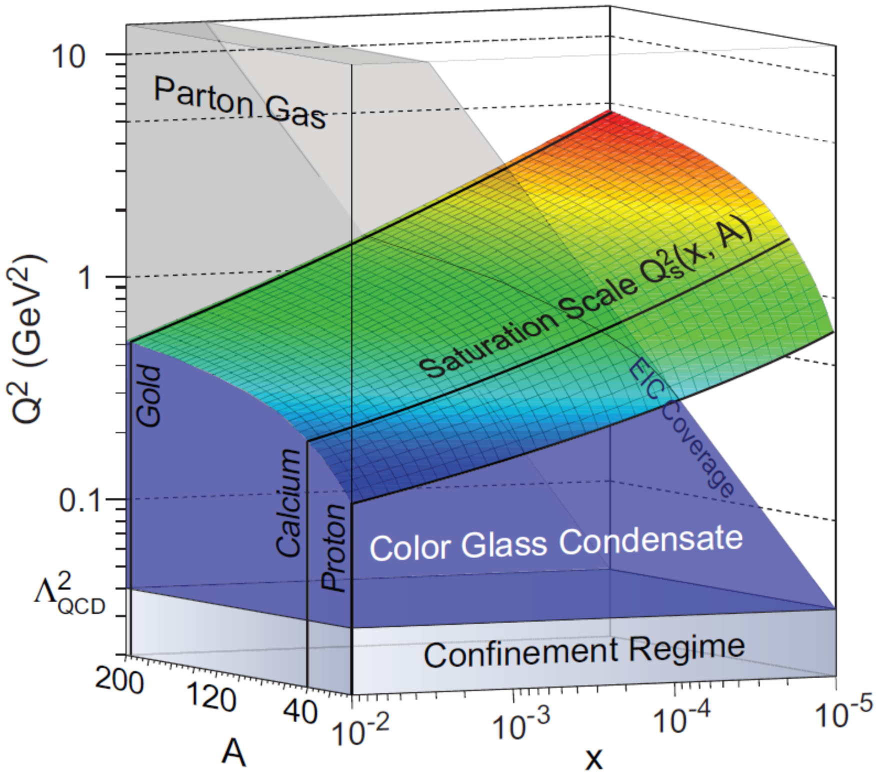

Figure 1.5: Theoretical model of the saturation scale at medium impact parameter as a function of the nuclear mass number A and x [5].

Chapter 2

Ultra-peripheral collisions

At hadron colliders it is not possible to collide leptons with hadrons and study their structure with DIS as was described in Chapter 1. Only hadron-hadron collisions are possible. However, in hadronic collisions the colliding particles interact mostly via the strong force and in such a case it is often complicated to compute the underlying processes from first principles of QCD. Nevertheless, it is possible to study the inner structure of hadrons using ultra-peripheral collisions (UPC) which are in a sense similar to deep-inelastic scattering. This chapter is loosely based on the article "Ultra-peripheral heavy-ion collisions at the LHC" [6] by J. G. Contreras and J. D. Tapia Takaki.

2.1 Photoproduction

Ultra-peripheral collisions utilise the fact that when electrically charged hadrons collide at large impact parameters b (larger than the sum of the radii of the colliding particles $R_1 + R_2$), the interaction via the strong force is heavily suppressed by their distance. In these collisions the hadrons can interact electromagnetically. A diagram of an ultra-peripheral collision can be seen in Fig. 2.1. When considering collisions of heavy ions or heavy ions with protons one can have a look at their electromagnetic field. This field is contracted due to the Lorentz boost of the particles and it can be described as a flux of virtual photons. For photoproduction processes the virtuality of the photons is very low and they are called quasi real, later in the text denoted γ. By taking the square of the Fourier transform of the electromagnetic form factor the photon flux per unit are can be described as [6]

$$n(k, \mathbf{b}_T) = \frac{\alpha_{\mathrm{em}} Z^2}{\pi^2 b^2} x^2 \left[K_1^2(x) + \frac{1}{\gamma} K_0^2(x) \right], \tag{2.1}$$

where k is the photon energy, Z is the charge of the ion, γ is the Lorentz boost, $x = kb/\gamma$ and K_i are the Bessel functions.

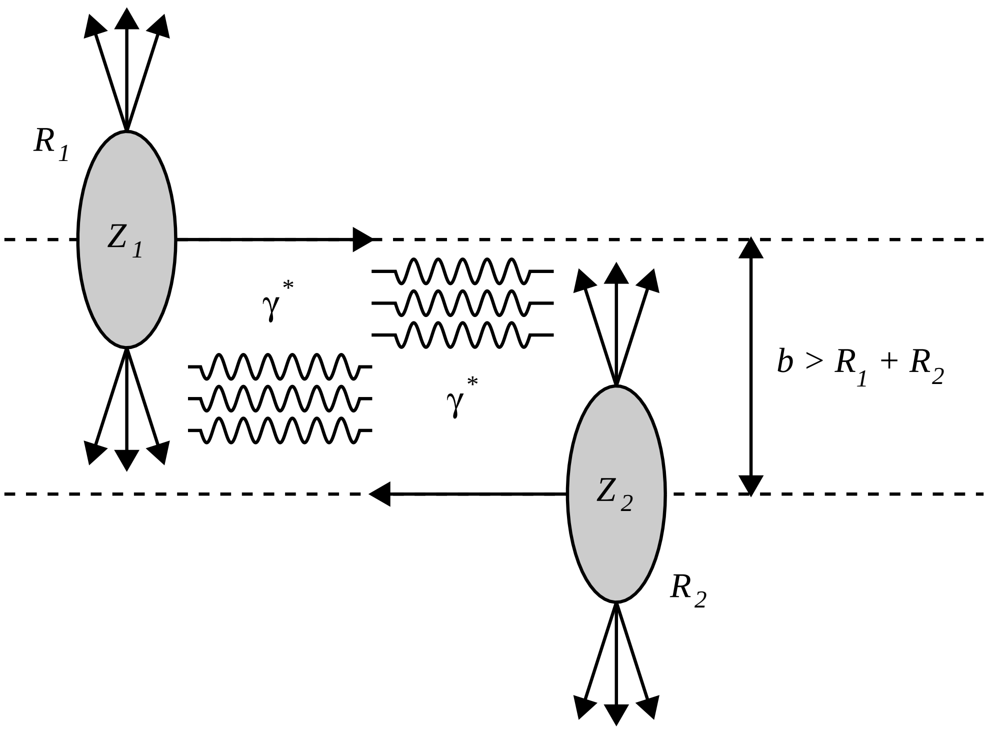

Figure 2.1: Diagram of an ultra-peripheral collision of two nuclei at an impact parameter b with charge $Z_i \cdot e$ and radii R_i, surrounded by a cloud of virtual photons γ^*.

If one considers the range from $b_{\text{min}} = R_1 + R_2$ to infinity, the following integral can be performed analytically

$$n(k) = \int \mathrm{d}^2\mathbf{b}_T \; n(k, \mathbf{b}_T), \tag{2.2}$$

and it is computed to be

$$n(k) = \frac{2\alpha Z^2}{\pi}\left[\xi K_0(\xi)K_1(\xi) - \frac{\xi^2}{2}(K_1^2(\xi) - K_0^2(\xi))\right], \tag{2.3}$$

where $\xi = kb_{\text{min}}/\gamma$. From this relation it is clear, that the intensity of the photon flux increases with Z^2, therefore heavy ions are a copious source of photons. The energy of these photons increases with increasing Lorentz boost of the particle, therefore high energy accelerators serve as a powerful source of energetic photons.

2.2 Two photon production of a dilepton pair

There are two types processes happening during UPC. The first one is a two photon production, for example of a dilepton pair

$$\gamma+\gamma \to l^{+}+l^{-}, \tag{2.4}$$

where $l = e, \mu$ (τ have not yet been measured). A diagram of this process can be seen in Fig. 2.2.

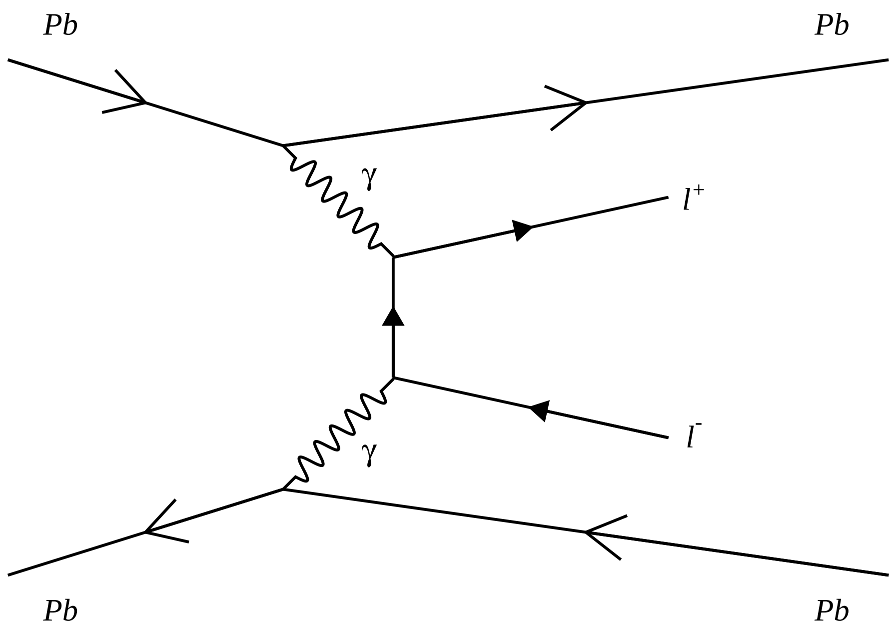

Figure 2.2: Diagram of a two photon production of a dilepton pair in a Pb-Pb ultra-peripheral collision.

In the lowest order of QED, the integrated cross section for this process is [7]

$$\sigma_{\gamma\gamma} = \frac{\pi\alpha_{\mathrm{em}}^{2}}{4s}\beta\left[\frac{3-\beta^{4}}{2\beta}\ln\frac{1+\beta}{1-\beta}-2+\beta^{2}\right], \tag{2.5}$$

where $\beta = \sqrt{1-4m_l^2/s}$, m_l is the mass of the lepton and $\sqrt{s}$ is the energy of the $\gamma\gamma$ system, which has to be above the threshold $2m_l$.

2.3 Exclusive vector meson photoproduction

A second process happening during UPC is exclusive vector meson photoproduction. A diagram of a photoproduction of a J/ψ can be seen in Fig. 2.4. In this process the photon interacts with the target, i.e. proton or ion (Pb in the diagram) and produces only a vector meson (it has to be a vector meson due to conservation of quantum numbers). When this vector meson is measured via its decay into dileptons, it provides a very clear experimental signature. An event display from ALICE of an ultra-peripheral collision with a vector meson candidate decaying into a dilepton pair can be see in Fig. 2.3 a) for a vector meson produced at central rapidity and b) for a vector meson produced at forward rapidity.

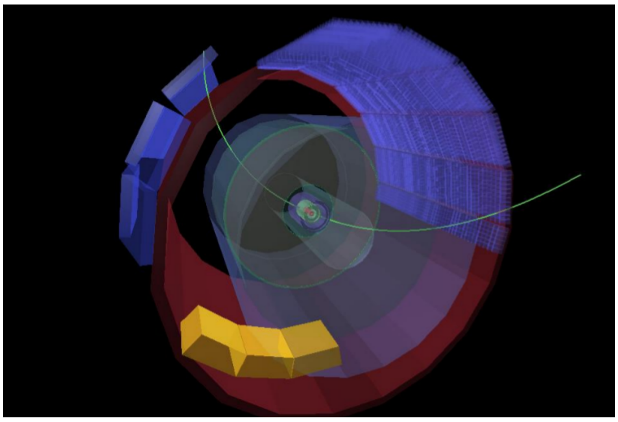

(a) Central rapidity ultra-peripheral collision.

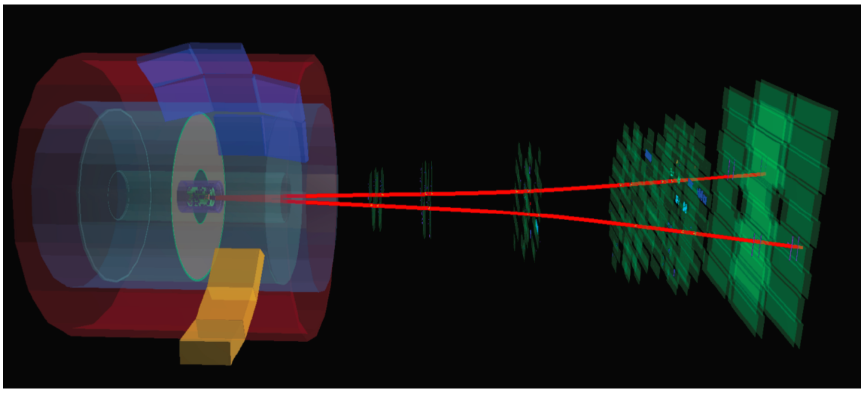

(b) Forward rapidity ultra-peripheral collision.

Figure 2.3: Event display of a candidate event for vector meson photoproduction at central rapidity (a) and forward rapidity (b).

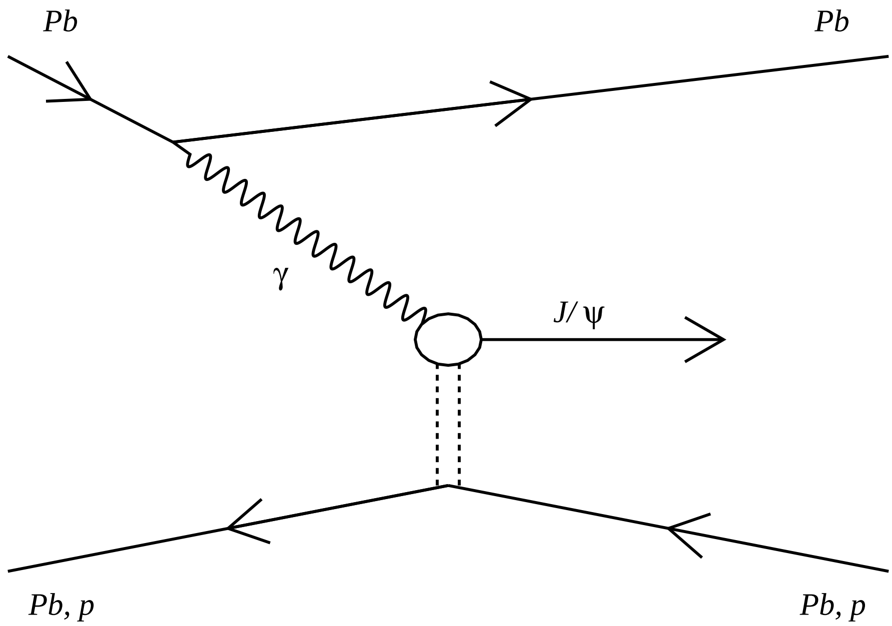

Figure 2.4: Diagram of the photoproduction of a J/ψ vector meson in a Pb-Pb or Pb-p ultra-peripheral collision.

2.3.1 Ultra-peripheral Pb-Pb collisions

When considering Pb-Pb collisions, the differential cross section for vector meson production is given by the product of the photon flux $N_{\gamma\mathrm{Pb}}$ produced by one of the nuclei and the photon-ion cross section $\sigma_{\gamma\mathrm{Pb}}$. However, as both ions may serve as the photon source or the target, the cross section is a sum of two symmetrical terms

$$\frac{\mathrm{d}\sigma_{\mathrm{PbPb}}(y)}{\mathrm{d}y} = N_{\gamma\mathrm{Pb}}(y,M)\sigma_{\gamma\mathrm{Pb}}(y) + N_{\gamma\mathrm{Pb}}(-y,M)\sigma_{\gamma\mathrm{Pb}}(-y), \tag{2.6}$$

where y is the rapidity of the vector meson.

The Pb-Pb collision can be divided into three possible categories:

- Coherent production, where the photon interacts coherently with the whole nucleus which stays intact after the collision. There is a coherence condition also for the photon itself, it is coherently produced by the electromagnetic field of the source ion. In such collisions, the typical transverse momenta of the produced vector meson is very low $p_T \approx 0.06$ GeV/c
- Coherent production with nuclear break up. Due to the intense electromagnetic fields the two colliding nuclei, producing the vector meson, can have another independent interaction via an exchange of low energy photons. This interaction causes one of the nucleus to transfer into an excited state. When the nuclei de-excites, it radiates forward neutrons.

- Incoherent production, where the photon does not interact with the whole nucleus, but only with a nucleon within the nucleus. Because the nucleon is much smaller than the nucleus, the average transverse momenta of the produced system is around $p_T \approx$ 0.3 GeV/c. Another consequence of the incoherent collisions is the break up of the target nucleus.

2.3.2 Ultra-peripheral Pb-p collisions

When considering the ion-proton collision, the differential cross section is basically the same apart form the fact that the proton is a much weaker source of photons. Taking into account the Z^2 dependence of the intensity of the photon flux, the term with the proton being the photon source can be safely neglected, resulting in a simpler formula

$$\frac{\mathrm{d}\sigma_{\mathrm{pPb}}(y)}{\mathrm{d}y} = N_{\gamma\mathrm{Pb}}(y,M)\sigma_{\gamma\mathrm{p}}(y). \tag{2.7}$$

The Pb-p collisions can be categorised into two groups:

- Exclusive production, where the photon interacts with the whole proton. This process has the same p_T characteristics as the incoherent case for Pb-Pb collisions, i.e. $p_T \approx$ 0.3 GeV/c.

- Dissociative production, where the proton is excited to a low mass diffractive state during the collision and the associated p_T reaches values above 1 GeV/c.

2.4 Photoproduction models

All models describing photoproduction cross sections in UPC are based on Eq. 2.6, hence they have two main components. The photon flux and the photon-nuclear cross section. The two main approaches concerning the photon flux are based on Eq. 2.1, the first one is the one leading to Eq. 2.3 and it is called the hard sphere approximation. The second one is integrating the Eq. 2.1 convoluted with the probability of no hadronic interaction. When considering the photon-nuclear cross section most of the models can be divided into three categories.

2.4.1 Vector dominance models

The vector dominance model (VDM) is based on approximating the γ + Pb/p $\rightarrow$ V + Pb/p collisions by the V + Pb/p $\rightarrow$ V + Pb/p collision, where the V is the produced vector meson. The rapidity dependent photon-lead cross section can be expressed as

$$\sigma_{\gamma\mathrm{Pb}}(y) = \left.\frac{\mathrm{d}\sigma_{\gamma\mathrm{Pb}}}{\mathrm{d}t}\right|_{t=0} \int_{t_{\min}}^{\infty} \mathrm{d}t\, |F(t)|^2\,, \tag{2.8}$$

where $F(t)$ is the nuclear form factor and t is the momentum transferred in the nucleus vertex.

Taking into account the VDM approximation, the optical theorem relates the photon-lead cross section with the total cross section $\sigma_{\mathrm{Tot}}(\mathrm{V}+\mathrm{Pb})$ as [6]

$$\left.\frac{\mathrm{d}\sigma_{\gamma\mathrm{Pb}}}{\mathrm{d}t}\right|_{t=0} = \frac{\alpha_{\mathrm{em}}\sigma^2_{\mathrm{Tot}}(\mathrm{V}+\mathrm{Pb})}{4 f_{\mathrm{V}}^2}, \tag{2.9}$$

where f_{V} is the vector meson-photon coupling. Then, using the Glauber model, the photon-lead cross section can be expressed by the photon-proton cross section as

$$\sigma_{\mathrm{Tot}}(\mathrm{V}+\mathrm{Pb}) = \int \mathrm{d}^2\mathbf{b}_T\,(1-\exp\left[-\sigma_{\mathrm{Tot}}(\mathrm{V}+\mathrm{p})T_{\mathrm{Pb}}(\mathbf{b}_T)\right])\,, \tag{2.10}$$

where T_{Pb} describes the thickness of the nucleus. The $\sigma_{\mathrm{Tot}}(\mathrm{V}+\mathrm{p})$ is obtained by using the optical theorem in the other direction for proton

$$\sigma^2_{\mathrm{Tot}}(\mathrm{V}+\mathrm{p}) = 16\pi \left.\frac{\mathrm{d}\sigma_{\mathrm{Vp}}}{\mathrm{d}t}\right|_{t=0}. \tag{2.11}$$

And again using the VDM approximation, the σ_{Vp} can be expressed by the photon-proton cross section as

$$\left.\frac{\mathrm{d}\sigma_{\mathrm{Vp}}}{\mathrm{d}t}\right|_{t=0} = \frac{f_{\mathrm{V}}^2}{4\pi\alpha_{\mathrm{em}}} \left.\frac{\mathrm{d}\sigma_{\gamma\mathrm{p}}}{\mathrm{d}t}\right|_{t=0}, \tag{2.12}$$

where the $\sigma_{\gamma\mathrm{p}}$ is parametrised by the following formula

$$\left.\frac{\mathrm{d}\sigma_{\gamma\mathrm{p}}}{\mathrm{d}t}\right|_{t=0} = b_{\mathrm{V}}\left(XW_{\gamma\mathrm{p}}^{\varepsilon} + YW_{\gamma\mathrm{p}}^{-\eta}\right). \tag{2.13}$$

The parameters $b_{\mathrm{V}}, X, \varepsilon, Y, \eta$ are obtained by fitting to experimental data. This is the model implemented in the STARlight Monte Carlo program [8].

2.4.2 Leading order perturbative QCD models

The models based on leading order perturbative QCD (LO pQCD) in the collinear approach compute the forward photon-nucleus cross section as

$$\left.\frac{\mathrm{d}\sigma_{\gamma\mathrm{Pb}}}{\mathrm{d}t}\right|_{t=0} = \frac{16\Gamma_{ee}\pi^3\alpha_s^2}{3M^5\alpha_{\mathrm{em}}}\left[xG_A(x,Q^2)\right]^2, \tag{2.14}$$

and use it as input for Eq. 2.8. The Γ_{ee} is the vector meson decay width to electrons, M is the mass of the vector meson and G_A is the nuclear gluon distribution function. This approach nicely demonstrates how the measurement of vector meson photoproduction cross section enables us to examine the gluon distributions.

The G_A is often parametrised as

$$G_A(x,Q^2) = g_p(x,Q^2)R_g^A(x,Q^2), \tag{2.15}$$

where $g_p(x,Q^2)$ is the proton gluon distribution function, which are fitted to HERA data, and $R_g^A(x,Q^2)$ is the nuclear modification factor introduced in Sec. 1.9.

2.4.3 Colour dipole models

The colour dipole models are based on the idea that the photon fluctuates into a quark-antiquark pair which forms a colour dipole. The models assume that the fluctuation happens long before the interaction of the dipole with the target and the formation of the vector meson happens long after the interaction. More details on the colour dipole model can be found in Chapter 3 where a discussion of two papers making predictions for vector meson photoproduction cross sections in UPC within the colour dipole model is presented.

Chapter 3

Colour dipole models of vector meson photoproduction in ultra-peripheral collisions

Predictions for vector meson photoproduction cross section in ultra-peripheral collisions within the colour dipole model from two papers are reviewed in this chapter. First, the predictions by T. Lappi and H. Mäntysaari [9] are presented. Then, the the predictions by V.P. Gonçalves and M.V.T. Machado [10] are presented.

3.1 J/ψ production in ultra-peripheral Pb-Pb and p+Pb collisions at energies available at the CERN Large Hadron Collider

"J/ψ production in ultra-peripheral Pb-Pb and p+Pb collisions at energies available at the CERN Large Hadron Collider" [9] is a paper by T. Lappi and H. Mäntysaari.

In the dipole picture the virtual photon emitted by the lead nucleus fluctuates into a quark-antiquark colour dipole which then can strongly interact with the target. The dipole model is valid only for small Bjorken x, thus an $x < 0.02$ condition is required for the target parton. The dipole-proton cross section can be expressed like

$$\frac{\mathrm{d}\sigma^{\mathrm{p}}_{\mathrm{dip}}}{\mathrm{d}^2\mathbf{b}_T}(\mathbf{b}_T, \mathbf{r}_T, x_{\mathbb{P}}) = 2\mathcal{N}(\mathbf{r}_T, \mathbf{b}_T, x_{\mathbb{P}}), \tag{3.1}$$

where $\mathbf{b}_T$ is the impact parameter of the γ-p collision, $\mathbf{r}_T$ is the transverse size of the dipole, $x_{\mathbb{P}}$ is the Bjorken variable of DIS in a diffractive event and $\mathcal{N}$ is the imaginary part of the forward dipole-proton scattering amplitude.

The dipole-proton amplitude $\mathcal{N}$ satisfies the Balitsky-Kovchegov (BK) evolution equation. The best approach would be to fit the initial conditions of the BK evolution equation to the available data from DIS, solve the BK equation and use the computed dipole amplitude.

For this calculation it is necessary to know the impact parameter dependence of the amplitude. However, when the impact parameter dependence is added to the BK equation, it leads to a non-physical growth of the size of the proton. Therefore, two phenomenological dipole cross section parametrisations, including realistic impact parameter dependence, were used.

First one is the IIM [11] dipole cross section which includes the most important features of the BK evolution. The values of the parameters for the cross section are taken from a fit to HERA data [12]. The second model is a factorised approximation of the IPsat model with eikonalised DGLAP (Dokshitzer–Gribov–Lipatov–Altarelli–Parisi) evolved gluon distribution [13, 14].

In the IIM model the impact parameter dependence is factorised as

$$\frac{\mathrm{d}\sigma_{\mathrm{dip}}^{\mathrm{p}}}{\mathrm{d}^2\mathbf{b}_T}(\mathbf{b}_T,\mathbf{r}_T,x) = 2T_p(\mathbf{b}_T)\mathcal{N}(\mathbf{r}_T,x). \tag{3.2}$$

Based on [15], the impact parameter profile function is chosen as

$$T_p(\mathbf{b}_T) = \exp\left(-b^2/2B_p\right), \tag{3.3}$$

where $B_p = 5.59\ \mathrm{GeV}^{-2}$.

In the IPsat model the impact parameter dependence is included in the saturation scale as

$$\frac{\mathrm{d}\sigma_{\mathrm{dip}}^{\mathrm{p}}}{\mathrm{d}^2\mathbf{b}_T}(\mathbf{b}_T,\mathbf{r}_T,x) = 2\left[1-\exp\left(-r^2F(x,r)T_p(\mathbf{b}_T)\right)\right], \tag{3.4}$$

where $r = |\mathbf{r}_T|$ and $T_p(\mathbf{b}_T)$ is defined same as in Eq. 3.3, but with $B_p = 4.0\ \mathrm{GeV}^{-2}$. $F(x,r)$ is proportional to the DGLAP evolved gluon distribution and is equal to

$$F(x,r) = \frac{1}{2\pi B_p}\frac{\pi^2}{2N_\mathrm{c}}\alpha_\mathrm{s}\left(\mu_0^2+\frac{C}{r^2}\right)xg\left(x,\mu_0^2+\frac{C}{r^2}\right), \tag{3.5}$$

where N_C is the number of colours, $C = 4$ and $\mu_0^2 = 1.17\ \mathrm{GeV}^2$ [14]. Following [16] Eq. 3.4 is replaced by a factorised approximation

$$\frac{\mathrm{d}\sigma_{\mathrm{dip}}^{\mathrm{p}}}{\mathrm{d}^2\mathbf{b}_T}(\mathbf{b}_T,\mathbf{r}_T,x) \approx 2T_p(\mathbf{b}_T)\left[1-\exp\left(-r^2F(x,r)\right)\right], \tag{3.6}$$

where $T_p(\mathbf{b}_T)$ and $F(x,r)$ stay the same. This approximation transforms the IPsat parametrisation to the form of Eq. 3.2 with $\mathcal{N}(r,x) = \left[1-\exp\left(-r^2F(x,r)\right)\right]$ and it is denoted as fIPsat.

The quasi-elastic (coherent and incoherent) vector meson production cross section in nuclear DIS is

$$\frac{\mathrm{d}\sigma^{\gamma^* A\to VA}}{\mathrm{d}t} = \frac{R_g^2(1+\beta^2)}{16\pi}\left\langle |\mathcal{A}(x_{\mathbb{P}},Q^2,\Delta_T)|^2\right\rangle_{\mathrm{N}}, \tag{3.7}$$

where $-Q^2$ is the virtuality of the photon, Δ_T is the transferred momentum, $1+\beta^2$ accounts for the real part of the amplitude and the R_g is a correction for the skewedness effect (gluons in the target having different x). The prescription for these factors is taken from [17]

$$\beta = \tan\frac{\pi\lambda}{2}, \tag{3.8}$$

$$R_g = \frac{2^{2\lambda+3}}{\sqrt{\pi}}\frac{\Gamma(\lambda+5/2)}{\Gamma(\lambda+4)}, \tag{3.9}$$

where

$$\lambda = \frac{\partial \ln \mathcal{A}}{\partial \ln 1/x_{\mathbb{P}}}. \tag{3.10}$$

The correction terms are important in the absolute normalisation of the cross section and are necessary to describe HERA data.

For the coherent cross section the amplitude $\mathcal{A}$ is squared after averaging ,$|\langle\mathcal{A}\rangle_{\mathrm{N}}|^2$, and for the incoherent cross section the variance is used $\left\langle|\mathcal{A}|^2\right\rangle_{\mathrm{N}} - |\langle\mathcal{A}\rangle_{\mathrm{N}}|^2$. To compute the average values the following formula is used [18]

$$\langle\mathcal{O}(\{\mathbf{b}_{Ti}\})\rangle_{\mathrm{N}} \equiv \int\prod_{i=1}^{A}\left[\mathrm{d}^2\mathbf{b}_{Ti}T_A(\mathbf{b}_{Ti})\right]\mathcal{O}(\{\mathbf{b}_{Ti}\}). \tag{3.11}$$

It is the average over the position of the nucleon in the nucleus. T_A is the Woods-Saxon distribution with nuclear radius $R_A = (1.12A^{1/3} - 0.86A^{-1/3})$ fm and surface thickness $d = 0.54$ fm.

The imaginary part of the scattering amplitude $\mathcal{A}$ is the Fourier transform of the dipole-target cross section σ_{dip} from impact parameter $\mathbf{b}_T$ to momentum transfer Δ_T, contracted with the overlap between the vector meson and the virtual photon wave function

$$\mathcal{A}(x_{\mathbb{P}},Q^2,\Delta_T) = \int\mathrm{d}^2\mathbf{r}_T\int\frac{\mathrm{d}z}{4\pi}\int\mathrm{d}^2\mathbf{b}_T[\Psi_V^*\Psi](r,Q^2,z)e^{-i\mathbf{b}_T\cdot\Delta_T}\frac{\mathrm{d}\sigma_{\mathrm{dip}}}{\mathrm{d}^2\mathbf{b}_T}(\mathbf{b}_T,\mathbf{r}_T,x_{\mathbb{P}}). \tag{3.12}$$

The Boosted Gaussian and the Gauss-LC parametrisations [14] are used to describe the overlap of the wave functions of the photon splitting into the quark-antiquark pair and of this pair forming the vector meson.

For a large and smooth nucleus the averaged amplitude is

$$\left\langle \mathcal{A}(x_{\mathbb{P}}, Q^2, \Delta_T) \right\rangle_{\mathrm{N}} = \int \frac{\mathrm{d}z}{4\pi} \mathrm{d}^2\mathbf{r}_T\, \mathrm{d}^2\mathbf{b}_T e^{-i\mathbf{b}_T\cdot\Delta_T} [\Psi_V^*\Psi](r, Q^2, z) \\ \times 2\left[1 - \exp\left\{-2\pi B_p A T_A(b)\mathcal{N}(r, x_{\mathbb{P}})\right\}\right]. \quad (3.13)$$

At large transferred momentum $-t = \Delta_T{}^2$ the cross section is strongly dominated by the incoherent contribution. Therefore the incoherent cross section at large $|t|$ is the total quasi-elastic cross section which can be computed as the average value of the squared amplitude $\left\langle |\mathcal{A}|^2 \right\rangle_{\mathrm{N}}$. This approach results in [16]

$$\left\langle \left|\mathcal{A}_{q\bar{q}}\right|^2 (x_{\mathbb{P}}, Q^2, \Delta_T) \right\rangle_N = 16\pi B_p A \int \mathrm{d}^2\mathbf{b}_T \int \mathrm{d}^2\mathbf{r}_T\, \mathrm{d}^2\mathbf{r}_T{}' \frac{\mathrm{d}z}{4\pi}\frac{\mathrm{d}z'}{4\pi} [\Psi_V^*\Psi](r, Q^2, z) \\ \times [\Psi_V^*\Psi](r', Q^2, z') e^{-B_p\Delta_T{}^2} e^{-2\pi B_p A T_A(b)[\mathcal{N}(r)+\mathcal{N}(r')]} \left(\frac{\pi B_p \mathcal{N}(r)\mathcal{N}(r') T_A(b)}{1 - 2\pi B_p T_A(b)\left[\mathcal{N}(r) + \mathcal{N}(r')\right]} \right). \quad (3.14)$$

Following [19] the vector meson production cross section in nucleus-nucleus (or proton-nucleus) collisions is factorised as the product of the photon flux generated by one of the nuclei and the photon-nucleus cross section

$$\sigma^{pA\to\mathrm{J}/\psi A} = \int \mathrm{d}\omega \frac{n(\omega)}{\omega} \sigma^{\gamma A\to\mathrm{J}/\psi A}(\omega), \quad (3.15)$$

where $\sigma^{\gamma A\to\mathrm{J}/\psi A}$ is the photon-nucleus cross section, $n(\omega)$ is the photon flux, $\omega = (M_V/2)e^y$ is the energy of the photon, M_V is the vector meson mass and y is the vector meson rapidity.

In nucleus-nucleus collision both of the nuclei can act as the photon source, therefore

$$\frac{\mathrm{d}\sigma^{A_1A_2\to\mathrm{J}/\psi A_1A_2}}{\mathrm{d}y} = n^{A_2}(y)\sigma^{\gamma A_1}(y) + n^{A_1}(-y)\sigma^{\gamma A_2}(-y). \quad (3.16)$$

In proton-nucleus collision the proton can also act as the photon source, but as the generated photon flux is proportional to the square of the electric charge of the emitting particle, the case when the photon is emitted from the nucleus dominates.

The Bjorken x of the probed gluon, denoted $x_{\mathbb{P}}$, is

$$x_{\mathbb{P}} = M_V e^{-y}/\sqrt{s_{\mathrm{NN}}}. \quad (3.17)$$

For forward and backward rapidity this means either a small energy photon scattering off a large-x gluon or a large energy photon scattering off a small-x gluon. At mid rapidity only a moderately small-x gluons are probed. The presented predictions should be most reliable in this region.

A comparison of the predictions of coherent J/ψ photoproduction cross section with the ALICE data [20, 21] can be seen in Fig. 3.1.

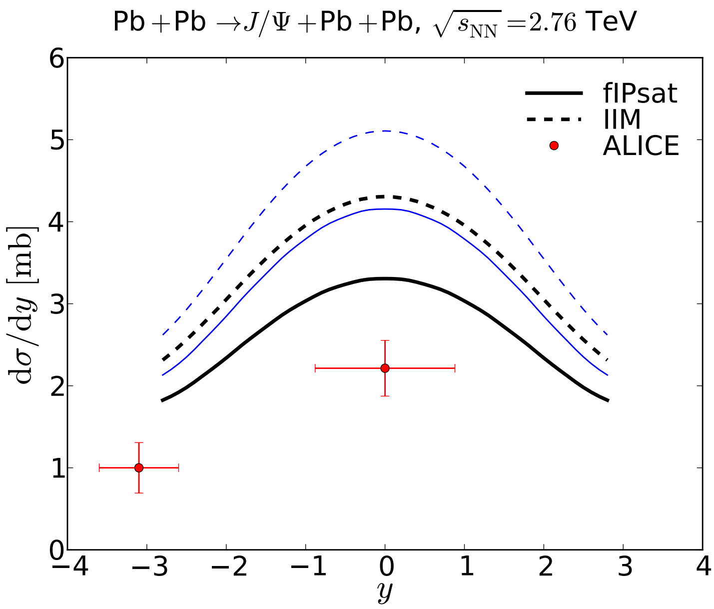

Figure 3.1: The coherent J/ψ photoproduction cross section prediction for Pb-Pb collisions at $\sqrt{s_{\rm NN}} = 2.76$ TeV computed with the fIPsat and IIM parametrisations and the Boosted Gaussian (thin blue lines) and Gauss-LC (thick black lines) wave functions compared with the ALICE data ([20, 21]) [9].

The ALICE data seems to favour the fIPsat model over the IIM model. With regard to this, the most important difference between the models is the impact parameter dependence. The IIM parametrisation uses $B_p = 5.59$ GeV^{-2}, which comes from a fit to inclusive J/ψ production and the IIM model is close to the value measured for the inclusive J/ψ production. The IPsat parametrisation has smaller $B_p = 4.0$ GeV^{-2}, which comes from a fit to exclusive J/ψ production measured by HERA, therefore the fIPsat model is considered more reliable for the exclusive J/ψ photoproduction.

The ALICE data also seems to favour the Gauss-LC wave function over the Boosted Gaussian, therefore the fIPsat model with the Gauss-LC wave function is considered to be the most reliable combination.

The PHENIX collaboration has measured the coherent J/ψ photoproduction cross section in Au+Au collisions at $\sqrt{s_{NN}} = 200$ GeV to be $\left.\frac{d\sigma_{J/\psi+Xn}}{dy}\right|_{|y|<0.35} = 76 \pm 31\,(\text{stat}) \pm 15\,(\text{syst})\ \mu\text{b}$ [22]. And the fIPsat dipole cross section parametrisation with the Gauss-LC wave function predicts 109 μb.

The presented results are slightly higher than the measured values, but the rapidity dependence is reproduced correctly. The fIPsat model with the Gauss-LC wave function is consistently above all data points by a factor of approximately 1.4. Note that all the parametrisations used are older than the ALICE data. They describe well the HERA data, but no nuclear data were used to constrain them. The normalisation error is most likely caused by the skewedness correction. The corrections is larger for ALICE data than for HERA data, making it less reliable.

The prediction for the incoherent J/ψ photoproduction cross section can be seen in Fig. 3.2.

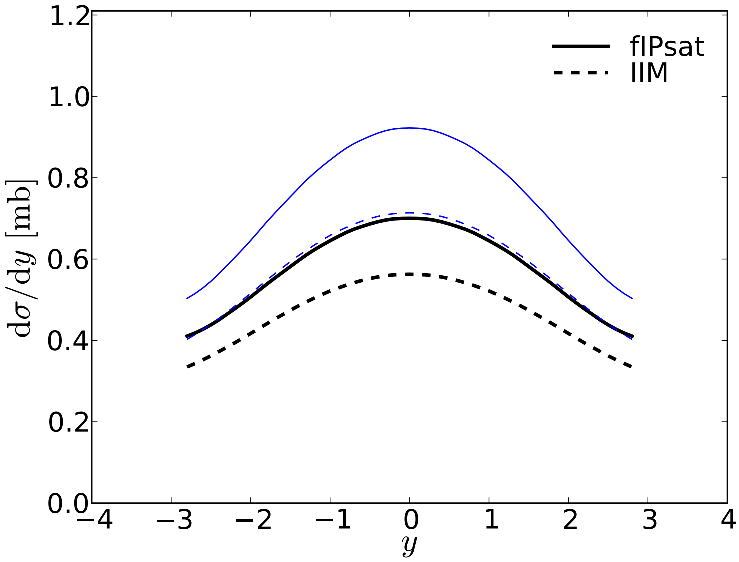

Figure 3.2: The incoherent J/ψ photoproduction cross section prediction for Pb-Pb collisions at $\sqrt{s_{NN}} = 2.76$ TeV computed with the fIPsat and IIM parametrisations and the Boosted Gaussian (thin blue lines) and Gauss-LC (thick black lines) wave functions [9].

The normalisation of the different models varies quite a lot again, but the rapidity dependence remains very similar. Now the normalisation is larger for the fIPsat model, this is due to different impact parameter parametrisation, see [16].

In Fig. 3.3 is presented the prediction for the t distribution of the J/ψ photoproduction at mid rapidity ($x_{\mathbb{P}} \approx 0.001$).

The t distribution for incoherent J/ψ production cross section directly measures the spatial distribution of partons (gluons) in the nucleon.

In Fig. 3.4 is presented the prediction for the rapidity dependence of the J/ψ photoproduction cross section in proton-lead collisions (the photon-nucleus scattering is required to be coherent). The difference between the model's normalisation is reduced, because the dominant process is now the photon-proton scattering, which is constrained by HERA data.

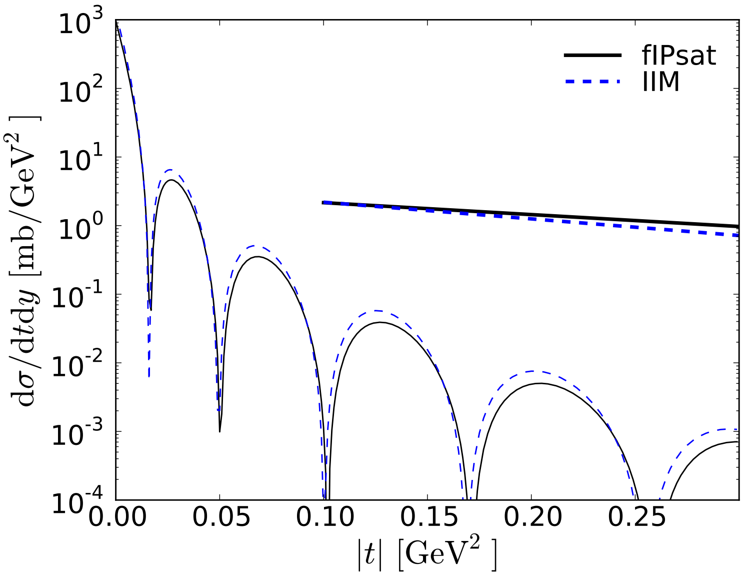

Figure 3.3: The coherent (thick lines) and incoherent (thin lines) J/ψ photoproduction cross section in lead-lead collision at $\sqrt{s_{\mathrm{NN}}} = 2.76$ TeV as a function of momentum transfer t at midrapidity $y = 0$ using the Gaus-LC wave function [9].

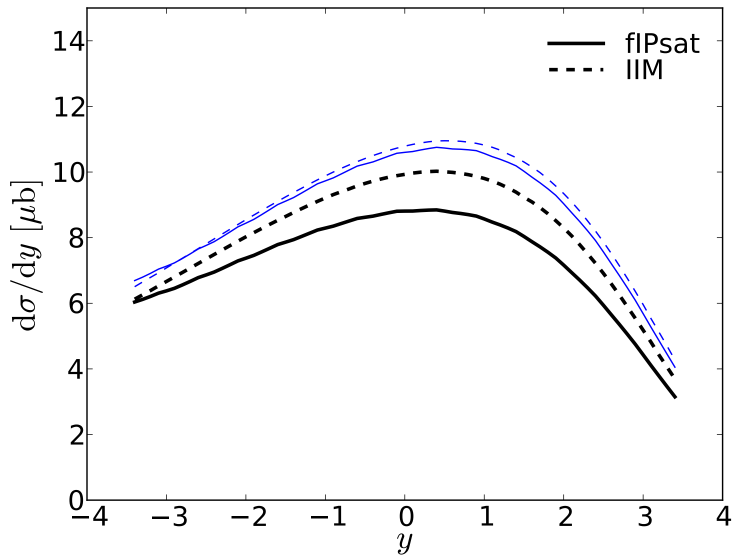

Figure 3.4: The J/ψ photoproduction cross section in proton-lead collisions at $\sqrt{s_{\mathrm{NN}}} = 5.02$ TeV computed using the fIPsat and IIM parametrisations and the Boosted Gaussian (thin blue lines) and Gauss-LC (thick black lines) wave functions. The proton is moving in the negative y direction [9].

In Fig. 3.5 the incoherent J/ψ photoproduction cross section in lead-lead collision is divided by A_{Pb} times the coherent J/ψ photoproduction cross section in proton-lead collision, both at $\sqrt{s_{NN}} = 2.76$. Because in proton-lead ultra-peripheral collisions the main process is a photon-proton collision, the above mentioned ratio is the nuclear transparency ratio, which measures the absorption of the colour dipole as it propagates through the nucleus.

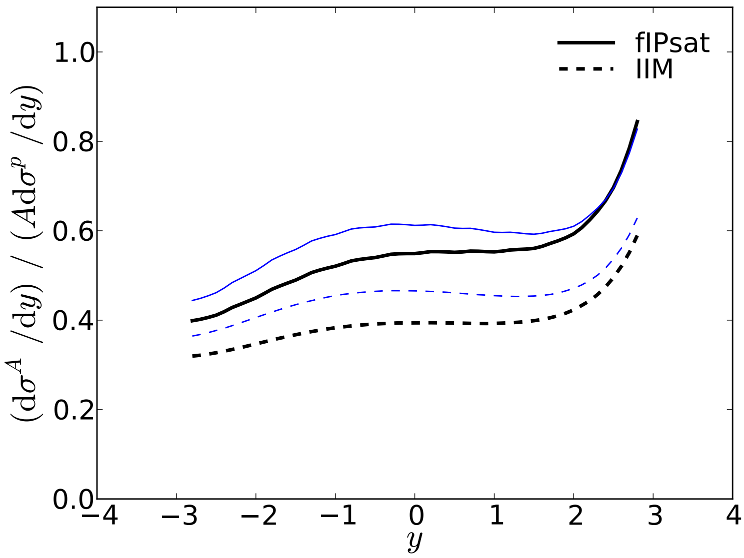

Figure 3.5: The nuclear transparency ratio at $\sqrt{s_{NN}} = 2.76$ TeV computed using the fIPsat and IIM parametrisations and the Boosted Gaussian (thin blue lines) and Gauss-LC (thick black lines) wave functions. The proton is moving in the negative y direction [9].

3.2 Vector Meson Production in Coherent Hadronic Interactions: An update on predictions for RHIC and LHC

"Vector Meson Production in Coherent Hadronic Interactions: An update on predictions for RHIC and LHC" [10] is a paper by V.P. Gonçalves and M.V.T. Machado.

The coherent vector meson (V) photoproduction cross section in a hadron-hadron collision is given by

$$\sigma(hh \to Vh) = 2 \int_{\omega_{min}}^{\infty} \mathrm{d}\omega \int \mathrm{d}t\, \frac{\mathrm{d}N_\gamma(\omega)}{\mathrm{d}\omega}\, \frac{\mathrm{d}\sigma}{\mathrm{d}t} \left(W_{\gamma h}, t\right) , \tag{3.18}$$

where $\frac{dN_\gamma(\omega)}{d\omega}$ is the equivalent photon flux, $\frac{d\sigma}{dt}\left(W_{\gamma h},t\right)$ is the differential cross section for the process $(\gamma h \to Vh)$, ω is the photon energy, $\omega_{min} = M_V^2/4\gamma_L m_p$ is the minimum photon energy with M_V being the vector meson mass, γ_L is the Lorentz boost of a single beam, m_p is the mass of a proton, $W_{\gamma h}^2 = 2\,\omega\sqrt{s_{\rm NN}}$ is the c.m.s energy of the photon-hadron system with $\sqrt{s_{\rm NN}}$ is the c.m.s energy of the hadron-hadron system and $t = -\Delta^2$, where Δ is the transferred transverse momentum.

For ultra-peripheral collisions the equivalent photon flux of a nuclei can be approximated as [23, 19, 24]

$$\frac{dN_\gamma(\omega)}{d\omega} = \frac{2Z^2\alpha_{em}}{\pi\,\omega}\left[\bar{\eta}\,K_0\,(\bar{\eta})\,K_1\,(\bar{\eta}) + \frac{\bar{\eta}^2}{2}\mathcal{U}(\bar{\eta})\right], \tag{3.19}$$

where Z is the charge of the hadron, α_{em} is the fine-structure constant, $K_0(\bar{\eta})$ and $K_1(\bar{\eta})$ are the modified Bessel functions, $\bar{\eta} = \omega\,(2R_h)/\gamma_L$ with R_h being the hadron radius and $\mathcal{U}(\bar{\eta}) = K_1^2\,(\bar{\eta}) - K_0^2\,(\bar{\eta})$. The factor 2 in Eq. 3.19 takes into account that both nuclei can act as the either the source or the target.

For proton-proton collisions the photon flux is given by [25]

$$\frac{dN_\gamma(\omega)}{d\omega} = \frac{\alpha_{\rm em}}{2\pi\,\omega}\left[1+\left(1-\frac{2\,\omega}{\sqrt{s_{NN}}}\right)^2\right]\left(\ln\Omega - \frac{11}{6} + \frac{3}{\Omega} - \frac{3}{2\Omega^2} + \frac{1}{3\Omega^3}\right), \tag{3.20}$$

where $\Omega = 1 + [\,(0.71\,{\rm GeV}^2)/Q_{\rm min}^2\,]$ and $Q_{\rm min}^2 = \omega^2/[\,\gamma_L^2\,(1-2\,\omega/\sqrt{s_{NN}})\,] \approx (\omega/\gamma_L)^2$.

Within the colour dipole approach, the vector meson (V) production amplitude is calculated as [26, 27, 14]

$$\mathcal{A}_{T,L}^{\gamma^* h \to Vh}\,(x,Q^2,\Delta) = \int dz\, d^2\mathbf{r}\,(\Psi^{V*}\Psi)_{T,L}\,\mathcal{A}_{q\bar{q}}(x,\mathbf{r},\Delta)\,, \tag{3.21}$$

where x is the Bjorken variable, Q^2 is the photon virtuality, z $(1-z)$ is the longitudinal momentum fraction of the quark (antiquark), $\mathbf{r}$ is the transverse size of the dipole, $(\Psi^{V*}\Psi)_{T,L}$ is the photon-vector meson wave function overlap and $\mathcal{A}_{q\bar{q}}$ is the dipole-target elastic scattering amplitude, which is connected to the scattering amplitude $\mathcal{N}(x,\mathbf{r},\mathbf{b})$ by [14]

$$\mathcal{A}_{q\bar{q}}(x,\mathbf{r},\Delta) \;\; = \;\; i\int d^2\mathbf{b}\,e^{-i\mathbf{b}.\Delta}\,2\mathcal{N}(x,\mathbf{r},\mathbf{b})\,, \tag{3.22}$$

where $\mathbf{b}$ is the impact parameter. With Eq. 3.22 the amplitude for the exclusive vector meson photoproduction can be expressed as

$$\mathcal{A}_{T,L}^{\gamma^* h\to Vh}(x,Q^2,\Delta) \;=\; i\int \mathrm{d}z\,\mathrm{d}^2\mathbf{r}\,\mathrm{d}^2\mathbf{b}e^{-i[\mathbf{b}-(1-z)\mathbf{r}]\Delta}(\Psi_V^*\Psi)_T\,2\mathcal{N}(x,\mathbf{r},\mathbf{b}), \tag{3.23}$$

where the $[i(1-z)\mathbf{r}]\Delta$ factor arises from non-forward corrections to the wave functions [28].

The differential cross section for exclusive vector meson photoproduction is given by

$$\frac{\mathrm{d}\sigma_{T,L}}{\mathrm{d}t}(\gamma^* h\to Vh) = \frac{1}{16\pi}|\mathcal{A}_{T,L}^{\gamma^* p\to Vh}(x,Q^2,\Delta)|^2\,(1+\beta^2)\,, \tag{3.24}$$

where β is the ratio of the real to imaginary part of the scattering amplitude. The skewedness corrections are also taken into account, for details see [14, 27].

The scattering amplitude $\mathcal{N}(x,\mathbf{r},\mathbf{b})$ contains all information about the target and the strong interaction physics. For the photon-nucleus collision the scattering amplitude can be assumed to be given by [29]

$$\mathcal{N}(x,\mathbf{r},\mathbf{b}) = \left\{1-\exp\left[-\frac{1}{2}AT_A(\mathbf{b})\,\sigma_{dip}(x,\mathbf{r})\right]\right\}\,, \tag{3.25}$$

where $T_A(\mathbf{b})$ is the nuclear profile function and $\sigma_{dip}(x,\mathbf{r})$ is the IIM [11] parametrisation of the dipole-nucleon cross section.

For the photon-proton collision the scattering amplitude can be described by the MPS [30] non-forward saturation model, which describes well the dependence on energy, photon virtuality and momentum transfer in HERA data. The dipole-target elastic scattering amplitude in the MPS model is given by

$$\mathcal{A}_{q\bar{q}}(x,r,\Delta) = \sigma_0\,e^{-B|t|}\mathcal{N}\left(rQ_{\mathrm{sat}}(x,|t|),x\right)\,, \tag{3.26}$$

where σ_0 is the normalisation parameter, the B parameter has value $B = 3.754$ GeV^{-2} [30] and

$$Q^2_{\mathrm{sat}}\,(x,|t|) = Q_0^2(1+c|t|)\left(\frac{1}{x}\right)^{\lambda}\,. \tag{3.27}$$

The rapidity distribution of the coherent vector meson photoproduction can be computed as

$$\frac{\mathrm{d}\sigma\;[h+h\to h\otimes V\otimes h]}{\mathrm{d}y} = \omega\frac{\mathrm{d}N_\gamma(\omega)}{\mathrm{d}\omega}\,\sigma_{\gamma h\to V\,h}\,(\omega)\,, \tag{3.28}$$

where $\otimes$ represents a rapidity gap.

The prediction for the rapidity distribution of J/ψ and Υ photoproduction cross section in p+p collisions at $\sqrt{s} = 7$ TeV at the LHC is presented in Fig. 3.6.

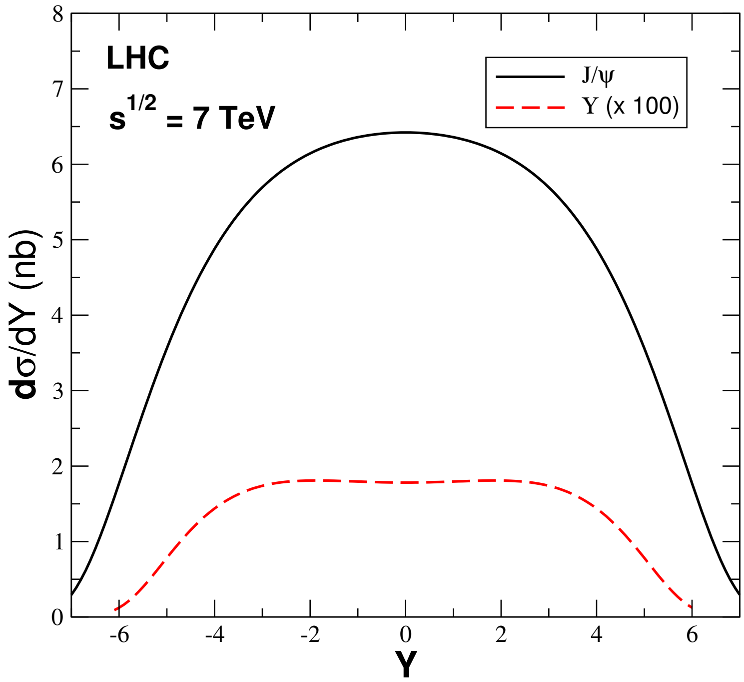

Figure 3.6: Prediction for the rapidity distribution of J/ψ and Υ photoproduction cross section in p+p collisions at $\sqrt{s} = 7$ TeV at the LHC [10].

At central rapidity the photoproduction cross section is $\frac{d\sigma}{dy}(y = 0) \simeq 6.5$ nb (18 pb) for J/ψ (Υ). In Table 3.1 are presented predictions for the integrated photoproduction cross sections (production rates) assuming a luminosity $\mathscr{L}^{\mathrm{pp}}_{\mathrm{LHC}} = 10^7$ mb^{-1}s^{-1}.

The prediction for the rapidity distribution of the ρ and J/ψ photoproduction cross sections in Au+Au collisions at $\sqrt{s} = 200$ GeV at RHIC is presented in Fig. 3.7. In Table 3.1 are presented predictions for the integrated photoproduction cross sections (production rates) assuming a luminosity $\mathscr{L}^{\mathrm{AuAu}}_{\mathrm{RHIC}} = 0.4$ mb^{-1}s^{-1}.

In Fig. 3.8 is presented the prediction for the rapidity dependence of the ratio between the J/ψ and ρ photoproduction cross sections. The presented prediction is without the correction for mutual nuclear excitation, which is rapidity dependent and for the integrated cross section gives an overall suppression factor of 1/10 [31]. The presented ratio J/ψ/ρ should have small sensitivity to the correction and at mid rapidity $\frac{d\sigma(\rho^0)}{dy} / \frac{d\sigma(J/\psi)}{dy} \simeq 1.2 \times 10^3$.

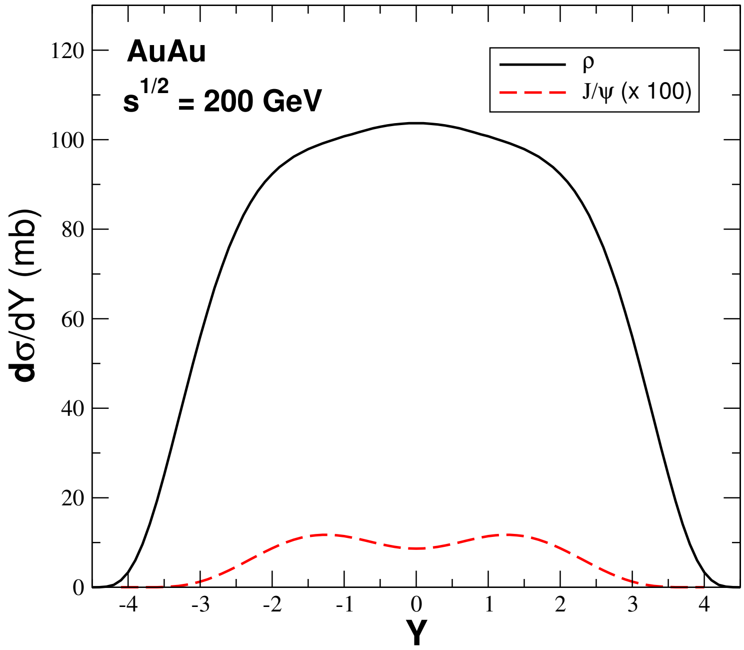

Figure 3.7: Prediction for the rapidity distribution of ρ and J/ψ photoproduction cross section in Au+Au collisions at $\sqrt{s} = 200$ GeV at the RHIC [10].

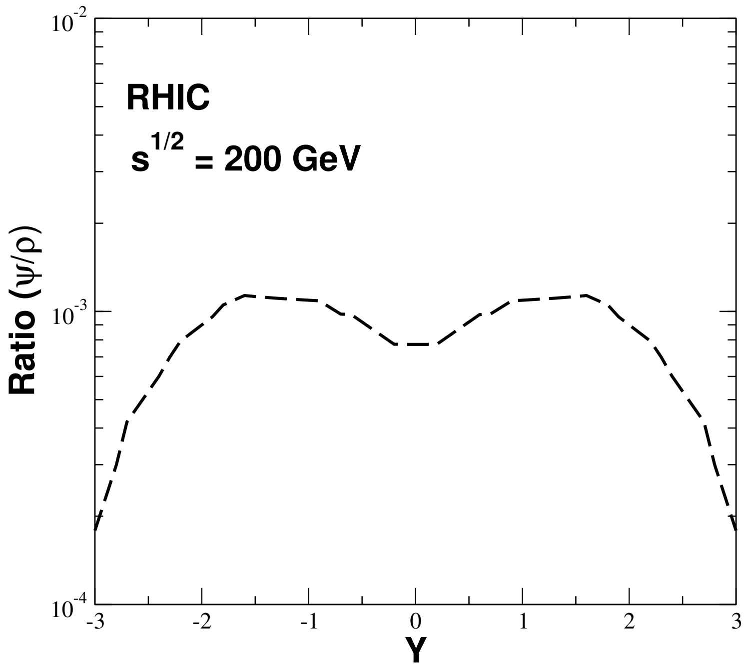

Figure 3.8: Prediction for the rapidity dependence of the ratio between the J/ψ and ρ photoproduction cross sections [10].

The prediction for the rapidity distribution of ρ and J/ψ photoproduction cross section in Pb-Pb collisions at $\sqrt{s_{NN}} = 2.76$ TeV at the LHC is presented in Fig. 3.9.

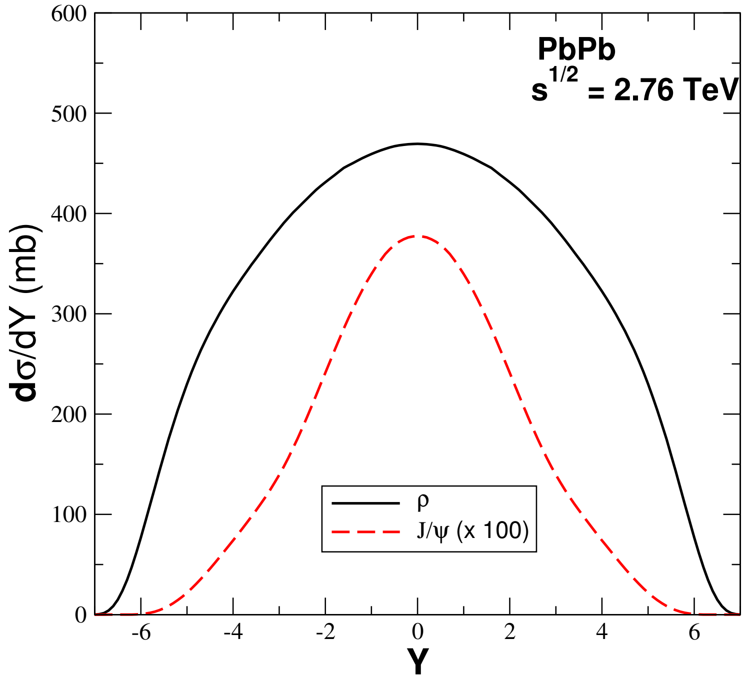

Figure 3.9: Prediction for the rapidity distribution of ρ and J/ψ photoproduction cross section in Pb-Pb collisions at $\sqrt{s_{NN}} = 2.76$ TeV at the LHC [10].

At central rapidity the photoproduction cross section is $\frac{d\sigma}{dy}(y=0) \simeq 3.8$ mb (470 mb) for J/ψ (ρ). And in Table 3.1 are presented predictions for the integrated photoproduction cross sections (production rates) assuming a luminosity $\mathscr{L}_{\mathrm{LHC}}^{\mathrm{PbPb}} = 0.42\ \mathrm{mb}^{-1}\mathrm{s}^{-1}$.

Meson	**RHIC (Au+Au)**	**LHC (Pb-Pb)**	**LHC (p+p)**
ρ	609.7 mb (256.0)	4276 mb (1796.0)	—
J/ψ	0.51 mb (0.20)	20 mb (8.40)	63.70 nb (637.0)
Υ	—	—	0.18 nb (1.80)

Table 3.1: The integrated cross section (events rate/second) for vector meson photoproduction in p+p and A+A collisions at RHIC and LHC energies [10].

Chapter 4

The ALICE experiment

To be able to make measurements of the cross section for vectors meson photoproduction at the energies discussed above, a vast experimental infrastructure is necessary. The ALICE experiment at CERN used to measure the data analysed and presented in this thesis is discussed in this chapter. The technical information presented in this chapter are taken from [32].

4.1 The Large Hadron Collider at CERN

The European Organisation for Nuclear Research (CERN) is a research organisation founded in 1954. It has 23 Member States, 7 Associate Members States and it has various co-operating scientific agreements with many other countries. More then 17 500 people of 110 nationalities are working together on the CERN scientific program.

The main goal of CERN is to provide scientist with an unique infrastructure necessary for their research. The primary focus of CERN is to maintain the CERN accelerator complex which can be seen in Fig. 4.1.

The Large Hadron Collider (LHC) is the largest particle accelerator in the world and it is the last link in the CERN accelerator complex. It has two beam pipes with a circumference of 27 kilometres. The particles in the beam pipes are guided by 1 232 dipole magnets and 392 quadrupole magnets, all of which are cooled by super liquid helium to $-271.3°$C. The particles are circulating in opposite directions in the two vacuumed beam pipes before they are collided at the four experimental sites (ATLAS, CMS, ALICE, LHCb).

The LHC provides collisions of protons on protons, protons on Pb ions, and Pb on Pb. It also provided collisions of Xe on Xe. All these collisions have been performed at the highest energies ever in the laboratory.

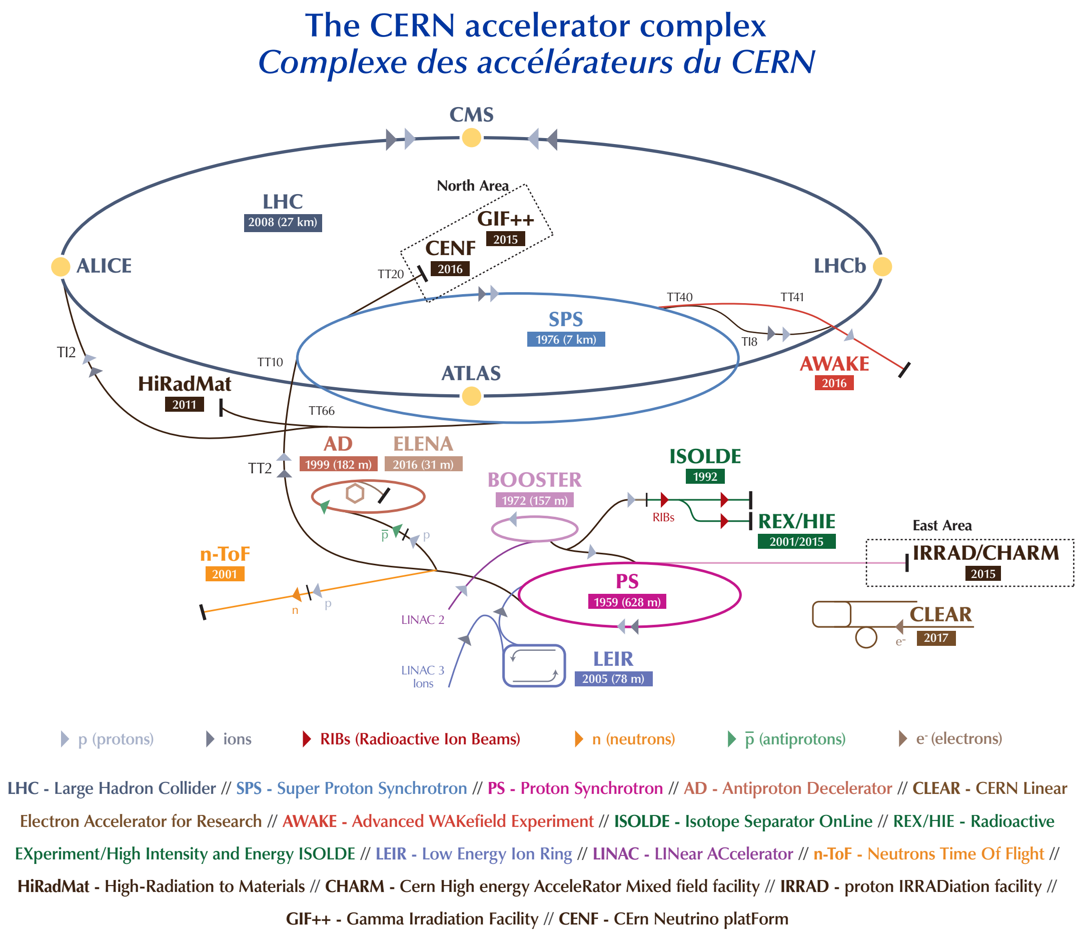

Figure 4.1: Schematic layout of the CERN accelerator complex with all of its accelerators, experiments and their connections [33].

4.2 ALICE

A Large Ion Collider Experiment (ALICE) is a general-purpose heavy ion detector. Its main goal is to study the quark-gluon plasma at extremely high temperatures and densities reached in heavy ion collisions. However, it can also be used to measure ultra-peripheral collisions. The ALICE detector is taking data also during proton-proton collisions to serve as a reference for the heavy ions measurements. The ALICE detector was build and is maintained by a collaboration consisting of more than 1 500 scientists from 37 countries.

A schema of the ALICE detector can be seen in Fig. 4.2, its dimensions are $16 \times 16 \times 26$ m^3 and its overall weight is approximately 10 000 tuns. The detector is composed of a central part measuring hadrons, electron and photons, and a forward spectrometer focused on muons.

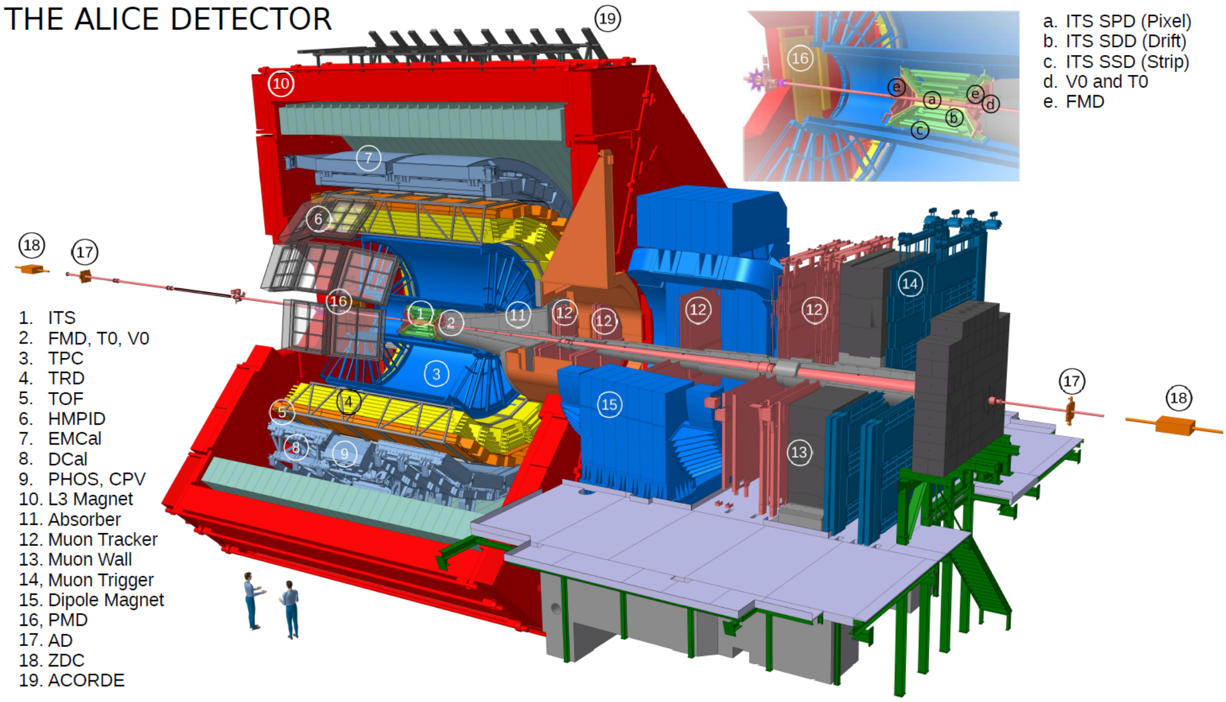

Figure 4.2: Cross section schema of the ALICE detector with the description of all of its subdetectors [34].

The central barrel has coverage in polar angle from 45°to 135°and full in azimuthal angle. It is located inside a solenoid magnet, reused from the L3 experiment, which provides a magnetic field of 0.5 T. The central barrel is composed of an Inner Tracking System (ITS) with six layers of high precision silicon pixel (SPD), strip (SSD) and drift (SDD) detectors, a Time Projection Chamber (TPC), a Time-of-Flight (TOF), a High Momentum Particle Identification Detector (HMPID) based on Ring Imaging Cherenkov (RICH) counters, a Transition Radiation Detector (TRD) and two electromagnetic calorimeters (PHOS and EMCal).

Several detectors measuring at small angles (ZDC, PMD, FMD, T0, V0, AD) are used for triggering and event characterisation. Some of which are discussed in more detail in this chapter.

The forward muon spectrometer is covering polar angles from 171°to 178°and full in azimuthal. It is composed of absorbers, tracking plates, magnet and trigger plates.

4.2.1 Muon spectrometer

The muon spectrometer was designed with the intention to measure the complete spectrum of heavy vector mesons, i.e., heavy quarkonia such as $J/\psi, \psi', \Upsilon, \Upsilon', \Upsilon''$ as well as the lighter ϕ, via its dimuon decay. Moreover, the unlike-sign continuum can be measured up to masses of 10 GeV/c^2. Since this continuum is mainly coming from open flavour mesons, it enables studying the production mechanisms of these mesons.

As the main limitation for the accuracy of these measurements is the small size of the corresponding cross section, the acceptance of the detector was designed to be as large as possible. The muon spectrometer coverage when expressed in pseudorapidity is $-4.0 < \eta < -2.5$. The semi-forward pseudorapidity region $-2.5 < \eta < -1.0$ can cover charmonium production when one of the decay products is detected in the central barrel and one in the forward muon spectrometer. The longitudinal cross section of the muon spectrometer can be seen in Fig. 4.3.

To be able to resolve the Υ resonances a resolution of 100 MeV/c^2 in the 10 GeV/c^2 region is necessary. This requirement governs the strength of the magnetic field and the granularity of the tracking plates in the tracking system. Moreover, to minimise multiple scattering the material of the absorbers and the detectors was carefully optimised.

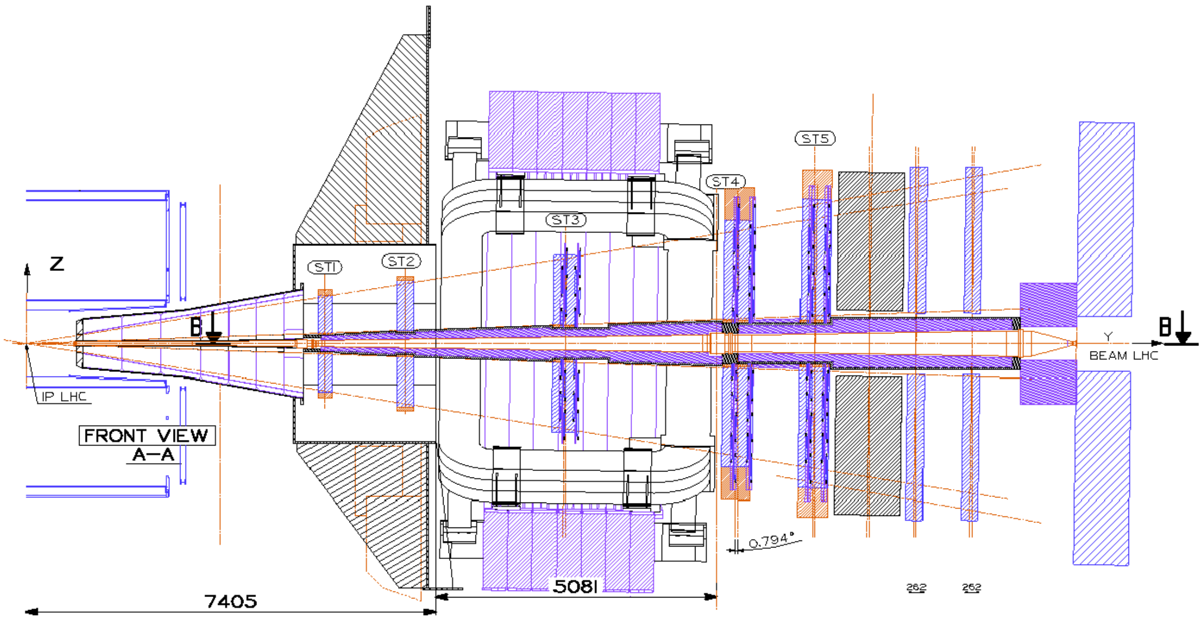

Figure 4.3: Blueprint of the longitudinal cross section of the forward ALICE Muon spectrometer and all of its parts [32].

Absorbers

The front absorber, made out of carbon and concrete, is located inside the solenoid magnet and it is 4.13 m long corresponding to $\sim 10\ \lambda_{\text{int}}$ and $\sim 60\ X_0$. The spectrometer is protected from the background caused by residual gas interactions by a dense beam pipe shield made of tungsten, lead and steel. To shield the trigger chambers a 1.2 m thick muon wall made out of iron is installed in front of them. The size of the muon filter corresponds to $\sim 7.2\ \lambda_{\text{int}}$ and together with the front absorbers it stops muons with momentum smaller than 4 GeV/c.

Tracking system

A space resolution of 100 μm is necessary in order to achieve the required invariant mass resolution. Cathode pad chambers were used to accomplish this. They are organised in five stations composed of two planes in order to get two dimensional location information. The first two stations are located before the dipole magnet and as they are closer to the interaction point (IP) they have finer granularity. This is done with quadrant structure where the readout electronics is located on the surface of the pads. A photo of the first station can be seen in Fig. 4.4 where pads as small as 4.2×6.3 mm^2 were used.

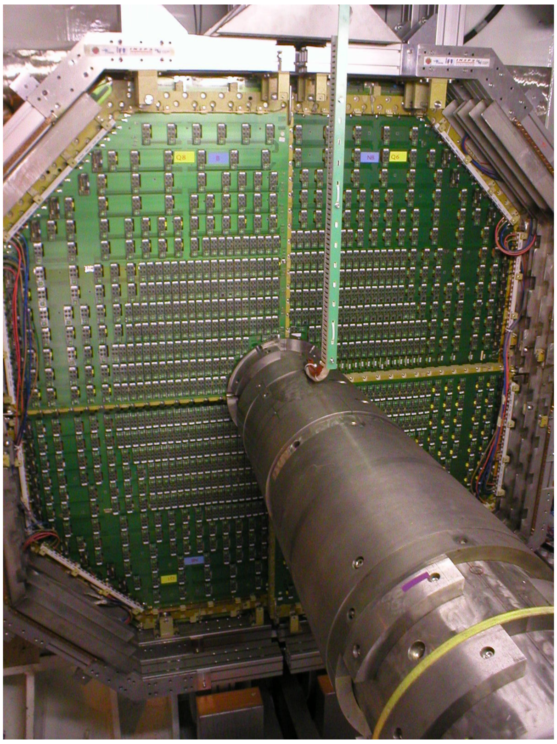

Figure 4.4: Photo of the first tracking station of the ALICE Muon spectrometer with the individual cathode pads visible [35].

The third station is located inside the 0.7 T dipole magnet and the last two stations are placed behind the magnet. These stations do not require such a fine granularity and therefore they are made with the slat architecture where the electronics is situated on the sides of the slats. The photo of the dipole and the fourth and fifth tracking station can be seen in the left part of Fig. 4.5, where the largest slats have dimensions of 40×280 cm^2. Both the slats and the quadrants overlap in order to avoid dead space in the detector.

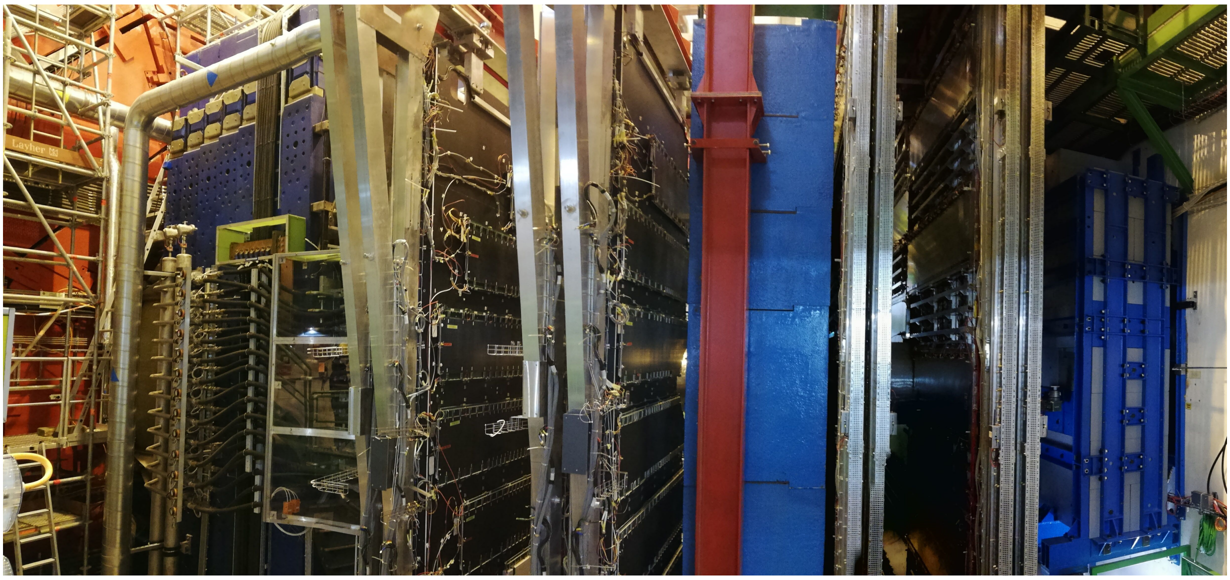

Figure 4.5: Photo of the ALICE Muon spectrometer. From left, the magnet surrounding the third tracking station, the fourth and fifth tracking station and the absorber protecting the two stations of muon trigger.

Trigger system

For heavy ion collisions with high multiplicity the muon spectrometer is hit by approximately eight low p_T muons from π and K decays per event. In order to be able to measure the high p_T muons coming from quarkonia decays a trigger is necessary.

The trigger is constructed from Resistive Plate Chambers (RPC) with spatial resolution better than 1 cm. The RPC are arranged in four planes grouped in two stations located behind the muon filter, this can be seen on the right side of Fig. 4.5. Each plane consists of 18 RPC with the approximate size of each module being 70×300 cm^2.

The trigger can perform two p_T cuts (high and low) in the range from ~ 0.5 GeV/c to ~ 2 GeV/c. This allows to produce six trigger signals: at least one muon track above the high/low p_T cut, at least two unlike-sign muon tracks above the high/low p_T cut and at least two like-sign muon tracks above the high/low p_T cut.

4.2.2 Zero-Degree Calorimeter

The Zero-Degree Calorimeter (ZDC) can detect the non-interacting spectator nucleons in a heavy ion collision and thus help to measure the centrality of the collision. There are two sets of hadronic ZDC located 112.5 m from the interaction point on both sides of the ALICE detector.

The spectator protons are deflected by the magnetic field of the LHC dipoles from the spectator neutrons. Therefore, two detectors are necessary to measure all spectator nucleons. For neutrons the detector (ZN) is located between the two beam pipes at 0°angle with respect to the LHC beam. For protons which are deflected the detector (ZP) is located externally on the side where the positive particles are deflected. A diagram (left) and a photo (right) of the ZDC with respect to he LHC beamline can be seen in Fig. 4.6.

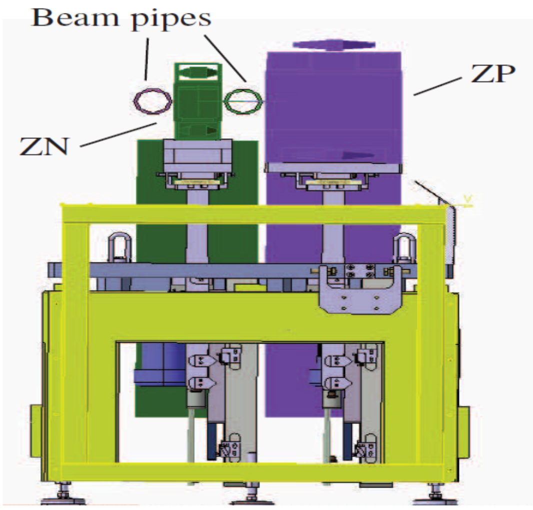

Figure 4.6: Schema (left) and photo (right) of the frontal view of the Zero-Degree Calorimeter. [32, 36].

The ZN and the ZP are sampling calorimeters using a passive material to evolve a shower which then produces Cherenkov radiation in quartz fibres embedded in the passive material. The quartz fibres were selected due to their radiation hardness, as the ZDC is subjected to high radiation environment. Due to space limitations of the beam pipes the ZN is made out of a dense tungsten alloy with dimensions of $7.04 \times 7.04 \times 100$ cm^3. The ZP is not a subject to such stringent constrains and therefore it is made out of brass, moreover the spacial distribution of the protons is wider than for neutrons and therefore the dimensions of the ZP are $12 \times 22.4 \times 150$ cm^3. Both the ZN and the ZP are located on moving platforms which can retract them from the beam horizontal plane when not in use.

The passive material of the ZDC is made out of metallic stacks with groves in the beam direction which are nested with the quartz fibres. The spacing of the fibres is smaller than the radiation length of the absorber material resulting in 1936 fibres for the ZN and 1690 for the ZP. For each hadronic ZDC there are five photomultiplier tubes (PMTs), the ZDC is divided into four quadrants on readout and every other fibre is connected to the PMT corresponding to its quadrant while the rest are connected to one common PMT for the whole detector. This makes the detector also position sensitive and enables to make estimations on the centroid of the incoming nucleons. Photos of the ZN (left) and ZP (right) can be seen in Fig. 4.7.

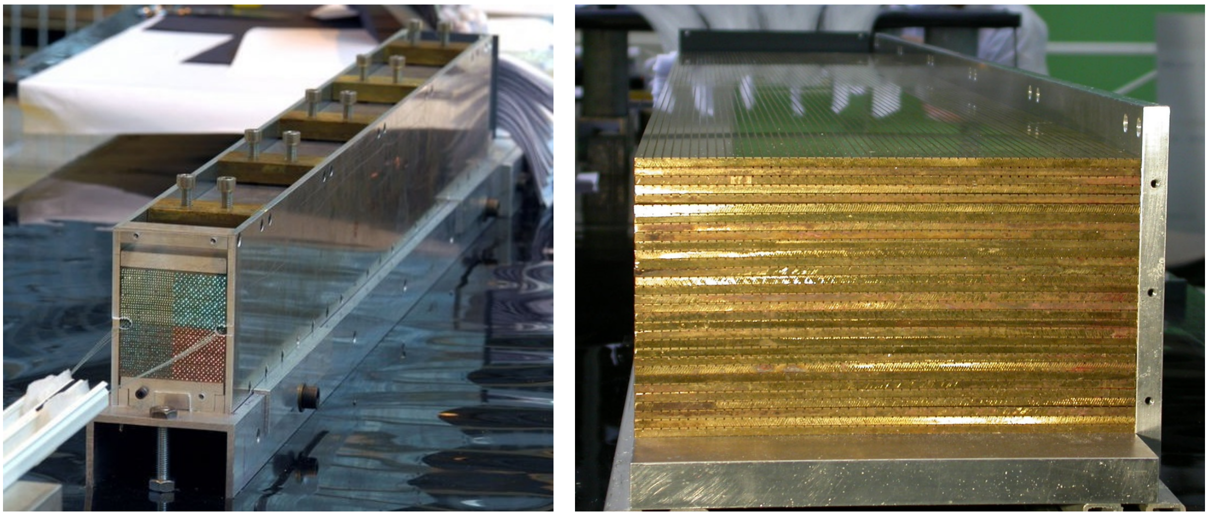

Figure 4.7: Photos of the ZN (left) and ZP (right) detectors [37, 38].

4.2.3 V0 detector

The V0 detector serves as a minimum bias trigger by measuring primary and secondary particles produced during both proton and ion collisions. As the number of detected particles is linearly proportional to the number of produced primary particles, the V0 enables centrality estimation by measuring the collision multiplicity. The V0 detector can help to identify false events, e.g., from collisions with the residual gas in the LHC beamline. This is especially important for the muon spectrometer as the muon trigger alone has a high background triggering rate and when combined with the V0 trigger the background is strongly suppressed. Lastly, the V0 detector also serves for luminosity measurement.

The V0 detector is a scintillator counter. It consists of two scintillating arrays on the opposite sides from the interaction point called V0A and V0C. The V0A is located 340 cm from the interaction point on the opposite side from the muon spectrometer. The V0C is located 90 cm from the interaction point and it is fixed to the face of the forward absorber. The pseudorapidity coverage of the V0A and V0C detectors is $2.8 < \eta_{V0A} < 5.1$ and $-3.7 < \eta_{V0C} < -1.7$ respectively. Each of the two arrays is divided into 32 cells arranged into four concentric rings. And each of these cells is measuring the signal produced by the incoming particles as well as the time of arrival of the signal. Photos of both of the V0A (left) and V0C (right) detectors can be seen in Fig. 4.8.

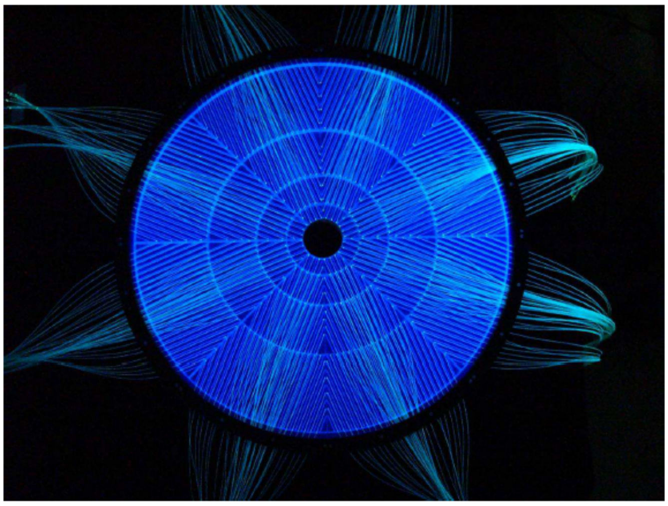 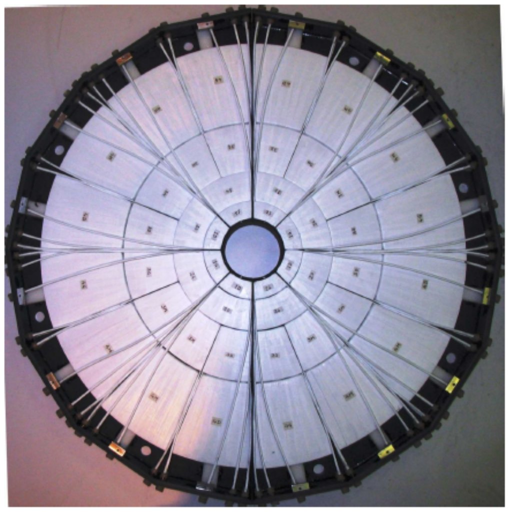

Figure 4.8: Photos of the V0A (left) and V0C (right) detectors [32].

The V0A detectors is made out of a 2.5 cm thick scintillating material with 1 mm diameter Wavelength Shifting (WLS) fibres spaced out by 1 cm and embedded into the faces of the 32 arrays. The 32 arrays are spaced in four concentric rings each divided into eight symmetric sectors. The PMTs for the V0A are located on the V0A support in groups of four and they are connected directly to the WLS fibres.

The V0C detectors is made out of a 2.0 cm thick scintillating material with 1 mm diameter WLS fibres glued to the radial sides of the individual cells in groups of nine. There are 48 cells of this type arranged in two inner rings of eight counters and two outer rings of sixteen counters coupled in pairs to make a single detection element. The PMTs for the V0C are located on the forward absorber in groups of eight and they are connected to the WLS fibres by 3.22 m long optical fibres.

4.2.4 The ALICE Diffractive detector

The ALICE Diffractive (AD) detector was installed between the years 2013 and 2014 during the Long Shutdown 1 and substantially extended the pseudorapidity coverage of the ALICE detector in Run 2. This enabled to significantly increase the trigger efficiency for diffractive and forward processes and suppress their contamination with background. The AD detector is also used to measure luminosity.

The AD detector consists of two stations (ADA, ADC) installed on opposite sides from the interaction point. The ADA is installed 16.95 m from the interaction point covering rapidity range $4.8 < \eta < 6.3$ and the ADC is installed 19.57 m from the IP covering rapidity range $-7.0 < \eta < -4.9$.

The ADA and ADC are composed of eight cells of scintillating plastic with dimensions of 216 mm $\times$ 181 mm $\times$ 25 mm. These cells are grouped in two layers of four quadrants around the beamline with WLS bars attached (not glued) to two sides of each cell. Each WLS bar is connected via 96 optical fibres to a PMT. The AD measures the intensity of the detected signal as well as the time of arrival of the signal. A schema and a photo of one station of the AD detector can be seen in Fig. 4.9.

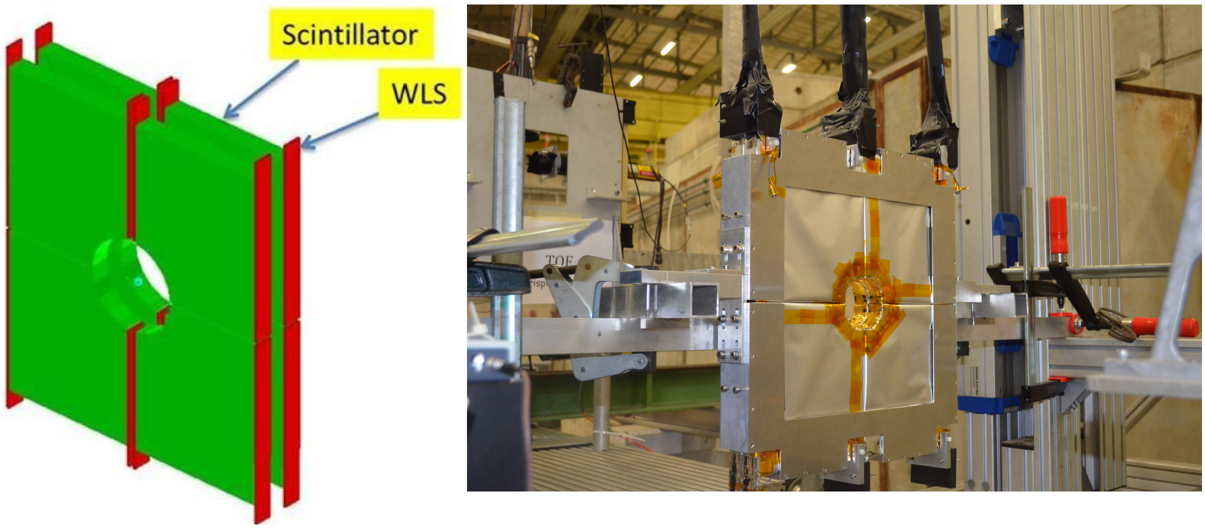

Figure 4.9: Schema (left) and photo (right) of the ALICE Diffractive detector [39].

4.2.5 UPC triggers

The interaction rate at the ALICE detector is so high that we cannot record every collision. ALICE is limited by the bandwidth of the electronics, by the storage necessary to save the data and by the processing power necessary to process the data. Therefore, we want to measure only events which have signatures of processes which we are interested in. For UPC events, where a dilepton pair is produced, the signature is very clear as shown in Fig. 2.3. Therefore, we want to measure only events with two lepton tracks in an otherwise empty detector. Triggers solve both of the problems discusses above.

The triggers used in data taking are composed as logical combinations of requirements based on information coming from different detectors. For the UPC muon triggers the following trigger elements are used:

- 0VBA = signal in V0A in beam-beam timing
- 0VBC = signal in V0C in beam-beam timing
- 0UBA = signal in ADA in beam-beam timing

- 0UBC = signal in ADC in beam-beam timing
- 0MSL = single muon over low p_T threshold in muon trigger
- 0MUL = unlike sign di-muon over low p_T threshold in muon trigger
- 0MLL = like sign di-muon over low p_T threshold in muon trigger

When the triggers are constructed they are created by joining the trigger elements with logical ”and” denoted by ”&”. Besides the trigger elements defined above, also their logical opposites are used which are denoted by ”!” before the name of the trigger element.

UPC triggers for the muon spectrometer for 2015 data taking of Pb-Pb collisions were defined as:

- CMUP10-B-NOPF-MUFAST = !0VBA & !0UBA & !0UBC & 0MSL
- CMUP11-B-NOPF-MUFAST = !0VBA & !0UBA & !0UBC & 0MUL
- CMUP13-B-NOPF-MUFAST = !0UBA & !0UBC & 0MUL

UPC triggers for the muon spectrometer for 2018 data taking of Pb-Pb collisions were defined as:

- CMUP6-B-NOPF-MUFAST = !0VBA & 0MUL
- CMUP11-B-NOPF-MUFAST = !0VBA & !0UBA & !0UBC & 0MUL
- CMUP26-B-NOPF-MUFAST = !0VBA & !0UBA & !0UBC & 0MLL

4.3 Software

4.3.1 AliRoot framework

The AliRoot framework is being developed continuously since 1998 by the ALICE collaboration. It is using ROOT as its foundation and it is build using object oriented techniques. It is fully written in C++ except few external programs hidden from the users which are still in FORTRAN. This is complemented by the AliEn environment which grants access to the computing grid, enabling physicist to use computing resources necessary for their analysis.

The main ideas taken into account for the development of the AliRoot framework were reusability and modularity. The modularity is manifested through independence of different parts of the code and by the possibility to easily exchange a given module (e.g. transport Monte Carlo model) without affecting the analysis process. The reusability is complemented by the modularity and it is further assured by focusing on maximum backward compatibility as the system develops over time.

The AliRoot framework contains Monte Carlo event generators, the description of the geometry of the ALICE detector to simulate the detector response for passing particles, the data coming from the different ALICE subdetectors, the analysis tools, such as ROOT, used for data processing and more. This enables physicists to use the AliRoot for a vast range of tasks.

4.3.2 ROOT and RooFit

ROOT is an object oriented toolkit written in C++ and developed at CERN. It enables data processing, data analysis, data visualisation and storage. It is designed to be able to process large amounts of data very efficiently. Roofit is an extension to ROOT mainly focused on modelling and fitting of physics data distributions. It enables to easily construct toy Monte Carlo data sets, use unbinned maximum likelihood fits and work with probability density functions.

4.3.3 LEGO trains and nano-AOD

The data recorded by ALICE is stored in a raw format. After calibrations an intermediate data format is created, called the ESD (event summary data). From this data, the final format to be used by physics analyses is created, the AOD (analysis object data).

To analyse effectively the large amount of data, there is a system called LEGO-train, where each wagon is an analysis task. In the case of UPC data, the LEGO-train is used to extract the UPC triggered events, that is, there is no analysis, just the production of files which have exclusively UPC triggered events. As the events are very small, the final set of data (called UPC nano-AOD) can be analysed by each user individually without incurring in a large overhead. The UPC nano-AOD are the initial input for my analysis.

Chapter 5

Previous measurement of coherent J/ψ photoproduction in Pb-Pb collisions with ALICE

This chapter summarises the direct predecessor of the measurement presented in this thesis. The Run 1 measurement from 2011 UPC Pb-Pb data measured with ALICE is presented.

Other papers involving photoproduction have been reviewed in my previous works: ”Photoproduction of J/ψ and of high mass e^+e^- in ultra-peripheral Au+Au collisions at $\sqrt{s_{\mathrm{NN}}} = 200$ GeV” [22] a paper by the PHENIX collaboration. ”Coherent J/ψ photoproduction in ultra-peripheral PbPb collisions at $\sqrt{s_{\mathrm{NN}}} = 2.76$ TeV with the CMS experiment [40] paper by the CMS collaboration. And ”Measurement of an excess in the yield of J/ψ at very low p_{T} in Pb-Pb collisions at $\sqrt{s_{\mathrm{NN}}} = 2.76$ TeV” [41] by the ALICE collaboration. All of the above are summarised in the Research project [42]. And the paper ”Charmonium and e^+e^- pair photoproduction at mid-rapidity in ultra-peripheral Pb-Pb collisions at $\sqrt{s_{\mathrm{NN}}}$=2.76 TeV” [43] by the ALICE collaboration is summarised in the Bachelor thesis [44].

5.1 Coherent J/ψ photoproduction in ultra-peripheral Pb-Pb collisions at $\sqrt{s_{\mathrm{NN}}}$ = 2.76 TeV

”Coherent J/ψ photoproduction in ultra-peripheral Pb-Pb collisions at $\sqrt{s_{NN}} = 2.76$ TeV” [45] is a paper by the ALICE collaboration and it is the direct predecessor of the measurement presented in this thesis.

The data presented in this paper were collected during 2011 in Pb-Pb ultra-peripheral collisions at $\sqrt{s_{\mathrm{NN}}} = 2.76$ TeV. The data were selected with a dedicated UPC trigger (FUPC) corresponding to integrated luminosity of 55 $\mu\mathrm{b}^{-1}$.

The FUPC trigger was defined as:

- A single muon with p_T above 1 GeV/c threshold in the muon trigger.
- At least one hit in the V0C detector with beam-beam timing. This corresponds to the produced muons and vetoes the beam-gas events.
- No hits in the V0A detector to reject hadronic collisions.

The following offline selection criteria were requested (number of events after selection):

- Two reconstructed tracks in the muon arm (432 422 events).
- Due to multiple scattering in the front absorber, the DCA distribution (Distance of Closest Approach) of the tracks coming from the interaction point can be described by a Gaussian, whose width depends on the absorber material and is proportional to $1/p$, where p is the momentum of the muon. The beam-gas background does not follow this distribution and was removed by applying a cut on the product $p\times$DCA, at 6 times the standard deviation. Additional uncertainty in the position of the primary vertex is negligible when compared to the multiple scattering effect (26 958 events).
- At least one of the muon track candidates was required to match a trigger track above the p_T threshold in the muon trigger chambers (10 172 events).
- Both tracks within the pseudorapidity range $-3.7 < \eta < -2.5$, to match the V0C acceptance (5 100 events).
- The tracks exit from the absorber in the range 17.5 cm $< R_{abs} <$ 89.5 cm, corresponding the angular acceptance of the spectrometer. Where R_{abs} is the radial coordinate of the track at the end of the front absorber (5 095 events).
- Dimuon rapidity in the range –3.6 $< y <$ –2.6, to ensure that the acceptance edges of the V0C were avoided in the muon spectrometer (4 919 events).
- Two tracks with opposite charges (3 209 events).
- Neutron ZDC signal below 6 TeV on each side. This cut did not remove any events with a J/ψ with p_T below 0.3 GeV/c, but reduces hadronic contamination at higher p_t (817 events).
- Dimuons with $p_t <$ 0.3 GeV/c and invariant mass 2.8 $< M_{inv} <$ 3.4 GeV/c^2 (122 events).
- V0 offline timing compatible with beam-beam timing (117 events).

The acceptance times efficiency correction (Acc$\times\varepsilon$) for the analysis was calculated using the STARlight generator passed through the Monte Carlo simulated detector response. Misalignment and variation of time dependent variables was taken into account. The muon trigger chambers efficiency was estimated from data and used in the total acceptance times efficiency correction. The estimated correction factors $(\mathrm{Acc}\times\varepsilon)_{\mathrm{J}/\psi}$ were 16.6 % and 14.3 % for the coherent and the incoherent J/ψ contributions respectively. The relative systematic error of the $(\mathrm{Acc}\times\varepsilon)_{\mathrm{J}/\psi}$ coming from the uncertainty of the muon trigger efficiency was estimated to be 4 %. From the reconstruction efficiency a 6 % contribution to the error was calculated. And the uncertainty coming from the generator selection was also studied making a less than 3 % contribution to the systematic error. The activity in the central barrel was checked and the signal was found to be compatible with noise.

The invariant mass distribution for the selected events can be seen in Fig. 5.1. There is a clearly visible J/ψ peak and a continuum coming from the two photon process. The combinatorial background in the J/ψ invariant mass range has been estimated to be less than 2 %.

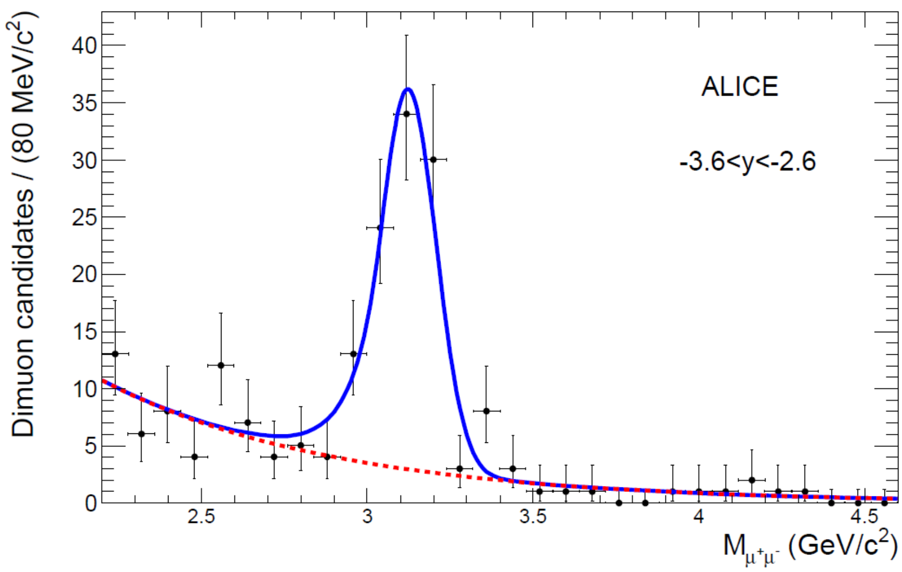

Figure 5.1: Invariant mass distribution of unlike-sign dimuons measured with the ALICE detector at $\sqrt{s_{NN}}$ = 2.76 TeV satisfying the criteria described in the text. The blue line describes the J/ψ peak and the red line describes the $\gamma\gamma$ continuum [45].

The distribution has been fitted with an exponential for the continuum and a Crystal Ball function for the peak. The parameters for the tail of the Crystal Ball have been fixed to values obtained from a fit to Monte Carlo data. The extracted number of J/ψ is $N_{\mathrm{yield}} = 96 \pm 12(\mathrm{stat}) \pm 6(\mathrm{syst})$.

The contribution to the number of J/ψ coming from the decay of $\psi' \to$ J/ψ + anything was computed from a sample of coherently produced ψ' simulated by STARlight and their decay to J/ψ was simulated with PYTHIA. The detector response was also simulated. Contribution from the incoherent ψ' was considered to be negligible for the $p_T < 0.3$ GeV/c region. The fraction of the events coming from the ψ' decay can be written as

$$f_D = \frac{\sigma_{\psi'} \cdot BR(\psi' \to \mathrm{J}/\psi + \text{anything}) \cdot (\mathrm{Acc} \times \varepsilon)_{\psi' \to \mathrm{J}/\psi}}{\sigma_{\mathrm{J}/\psi} \cdot (\mathrm{Acc} \times \varepsilon)_{\mathrm{J}/\psi}}, \tag{5.1}$$

where σ are the respective cross sections and BR are the respective branching ratios. The (Acc$\times\varepsilon$) factors were calculated for $p_T < 0.3$ GeV/c. The resulting feed down ratio is $f_D = (11 \pm 6)\%$, where different polarisations of the J/ψ and different models were considered.

In Fig. 5.2 is the transverse momentum distribution for the J/ψ invariant mass range $2.8 < M_{\mathrm{inv}} < 3.4$ GeV/c^2. The coherent J/ψ peak at low p_T is clearly visible, the incoherent peak has lower statistics and it extends over to higher p_T.

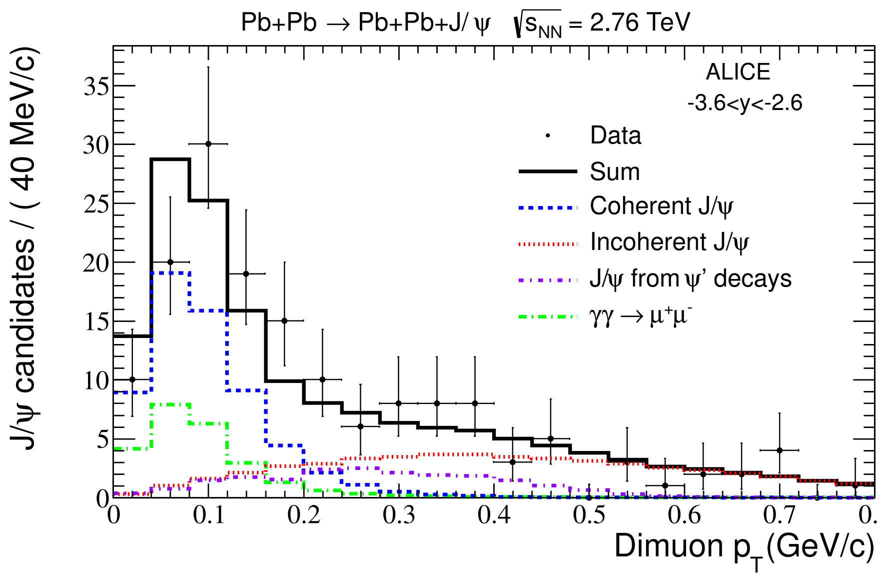

Figure 5.2: Transverse momentum distribution of unlike-sign dimuons measured with the ALICE detector at $\sqrt{s_{NN}}$ = 2.76 TeV satisfying the criteria described in the text. The blue line describes the coherent J/ψ, the red line describes the incoherent J/ψ, the purple line describes the feed down contribution from ψ' and the green line describes the $\gamma\gamma$ continuum [45].

The p_T distribution is fitted with four Monte Carlo templates based on STARlight and folded with the detector response. The contributions are from the coherent and incoherent J/ψ, the J/ψ from the ψ' decay and the two photon process. The contribution from the ψ' decay was constrained via the f_D ratio discussed above and the two photon contribution was fixed to value obtained from fit to the invariant mass distribution in Fig. 5.1. The normalisation for the coherent and the incoherent contributions was left free.

Due to possible hadronic contaminations the incoherent cross section is complicated to determine and the yield provided by the fit is only the upper constrain of the contribution. Therefore, to calculate the incoherent over coherent ratio f_I in the $p_T < 0.3$ GeV/c region, the $\sigma_{\mathrm{inc}}/\sigma_{\mathrm{coh}}$ fraction folded with the detector (Acc$\times\varepsilon$) was simulated. Taking into account simulations based on two different models and the results obtained from data the incoherent over coherent contribution ratio was calculated to be $f_I = 0.12^{+0.14}_{-0.04}$.

Based on the analysed data sample and results of hadronic J/ψ production, the contribution of hadronic events in the $p_T < 0.3$ GeV/c region is estimated to be negligible. Therefore the number of coherently produced J/ψ in the p_T range can be calculated as

$$N^{coh}_{\mathrm{J}/\psi} = \frac{N_{yield}}{1 + f_I + d_D}, \tag{5.2}$$

and resulting in $N^{coh}_{\mathrm{J}/\psi} = 75 \pm 10(\mathrm{stat})^{+7}_{-11}(\mathrm{syst})$.

The coherent J/ψ photoproduction cross section is then calculated as

$$\frac{\mathrm{d}\sigma^{coh}_{\mathrm{J}/\psi}}{\mathrm{d}y} = \frac{N^{coh}_{\mathrm{J}/\psi}}{(\mathrm{Acc}\times\varepsilon)_{\mathrm{J}/\psi} \cdot \varepsilon_{trig} \cdot BR(\mathrm{J}/\psi \to \mu^+\mu^-) \cdot \mathscr{L}_{int} \cdot \Delta y}, \tag{5.3}$$

where $(\mathrm{Acc}\times\varepsilon)_{\mathrm{J}/\psi}$ is the muon spectrometer acceptance times efficiency correction, ε_{trig} is the V0 trigger efficiency, $\mathscr{L}_{int}$ is the integrated luminosity and Δy is the rapidity bin size. Due to the settings for the V0 detector during the 2011 Pb-Pb run, the trigger efficiency calculation would require very precise simulation of the detector response and therefore the two photon continuum was used to normalise the coherent J/ψ cross section instead of Eq. 5.3. However, due to several theoretical uncertainties and uncertainties coming from the model, the STARlight two photon cross section has been estimated to have uncertainty of 20%.

When the two photon continuum is used for normalisation, the coherent J/ψ photoproduction cross section can be expressed as independent on the V0 trigger efficiency and the data sample luminosity

$$\frac{\mathrm{d}\sigma^{coh}_{\mathrm{J}/\psi}}{\mathrm{d}y} = \frac{1}{BR(\mathrm{J}/\psi \to \mu^+\mu^-)} \cdot \frac{N^{coh}_{\mathrm{J}/\psi}}{N_{\gamma\gamma}} \cdot \frac{(\mathrm{Acc}\times\varepsilon)_{\gamma\gamma}}{(\mathrm{Acc}\times\varepsilon)_{\mathrm{J}/\psi}} \cdot \frac{\sigma_{\gamma\gamma}}{\Delta y}, \tag{5.4}$$

where $N_{\gamma\gamma}$ is the number of events in the invariant mass intervals $2.2 < M_{inv} < 2.6$ GeV/c^2 ($N_{\gamma\gamma} = 43 \pm 7(\mathrm{stat})$) and $3.5 < M_{inv} < 6$ GeV/c^2 ($N_{\gamma\gamma} = 15 \pm 4(\mathrm{stat})$), in order to avoid contribution from the J/ψ peak. The cross sections and the acceptance times efficiency corrections for the corresponding intervals were calculated using Monte Carlo simulations.

As the $(\mathrm{Acc}\times\varepsilon)$ correction for the J/ψ photoproduction and the $\gamma\gamma$ process are computed for different kinematic regions, their uncertainty does not exactly cancel out in Eq. 5.4. Therefore a

50% correlation factor has been used for the uncertainty of the ratio. A summary of all source of systematic uncertainties can be found in Table 5.1.

Source	Value
Theoretical uncertainty in $\sigma_{\gamma\gamma}$	20 %
Coherent signal extraction	$^{+9}_{-14}$ %
Reconstruction efficiency	6 %
RPC trigger efficiency	5 %
J/ψ acceptance calculation	3 %
Two-photon e^+e^- background	2 %
Branching ratio	1 %
Total	$^{+24}_{-26}$ %

Table 5.1: Summary of the contributions to the systematic uncertainty for the integrated J/ψ cross section measurement. The error for the coherent signal extraction includes the systematic error in the fit of the invariant mass spectrum and the systematic errors on f_D and f_I [45].

The final cross section for the coherent J/ψ photoproduction is then computed to be $\mathrm{d}\sigma^{coh}_{\mathrm{J}/\psi}/\mathrm{d}y = (1.00 \pm 0.18(\mathrm{stat})^{+0.24}_{-0.26}(\mathrm{syst}))$ mb. This result is compared to several theoretical predictions in Fig. 5.3.

The models in Fig. 5.3 can be divided into three categories:

I. Models with no nuclear effects (AB-MSTW08), where all nucleons are contributing to the scattering.

II. Models using the Glauber approach to estimate the number of interacting nucleons (STARlight, GM, and CSS).

III. Perturbative QCD models (AB-EPS08, AB-EPS09, AB-HKN07, and RSZ-LTA), where the cross section is proportional to the nuclear gluon distribution squared.

As stated in Chapter 2 and Chapter 3 in Pb-Pb UPC both of the ions can act as the photon source. When using Eq. 3.17 the presented results are sensitive to gluon distribution functions at $x = 5 \cdot 10^{-5}$ and $x = 2 \cdot 10^{-2}$. However, STARlight predicts that the overall photoproduction cross section is dominated with 94% by the $x = 2 \cdot 10^{-2}$ contribution.

Figure 5.4 shows the integrated cross section compared to the models. A significant deviation of about 3 sigma is found for the AB-MSTW08 model and for STARlight prediction. Best agreement is found with the models based on pQCD involving moderate nuclear gluon shadowing.

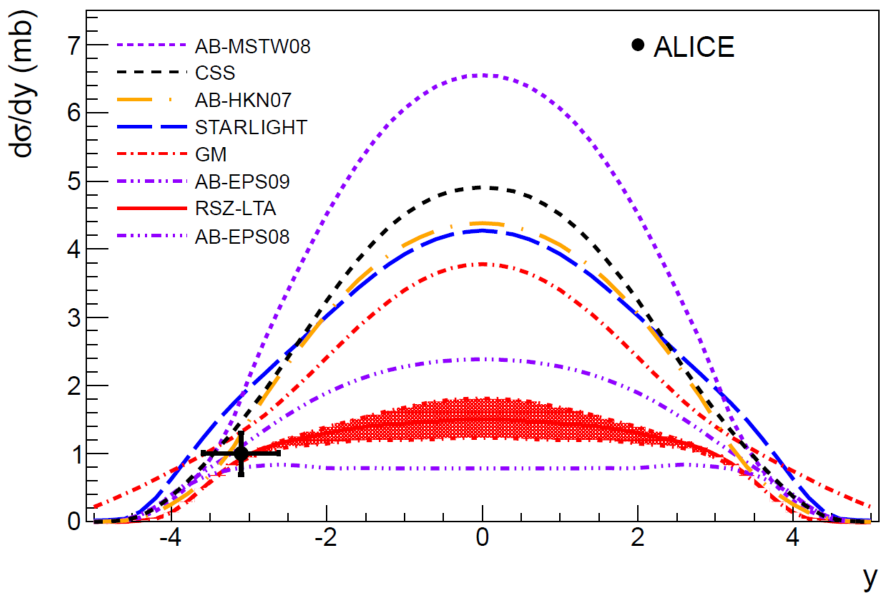

Figure 5.3: Rapidity distribution of the measured coherent differential cross section of J/ψ photoproduction in ultra-peripheral Pb-Pb collisions at $\sqrt{s_{NN}} = 2.76$ TeV. The error is the quadratic sum of the statistical and systematic errors. The theoretical predictions are also shown [45].

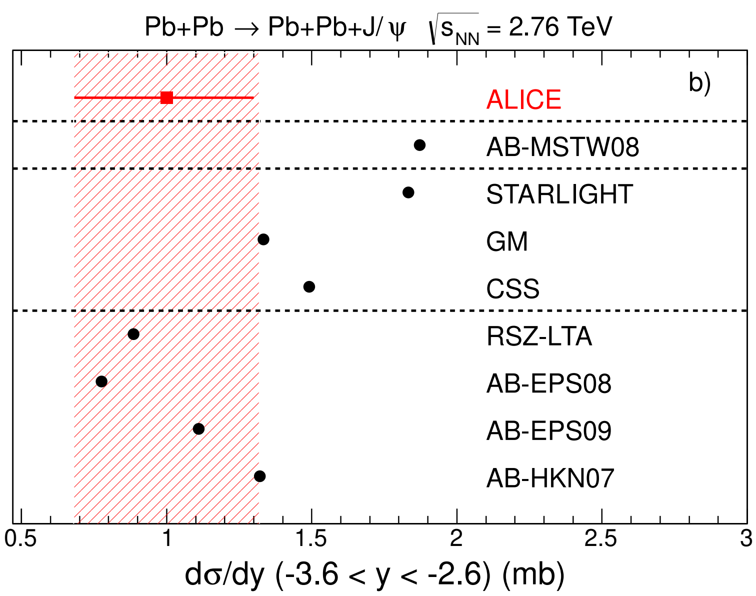

Figure 5.4: Integrated coherent J/ψ photoproduction cross section measured in ultra-peripheral Pb-Pb collisions at $\sqrt{s_{NN}} = 2.76$ TeV. The cross section is integrated over rapidity region $-3.6 < y < -2.6$. The error is the quadratic sum of the statistical and systematic errors. The theoretical predictions are also shown [45].

Chapter 6

Data analysis

The analysis described in this chapter is a successor of the paper based on the Run 1 ALICE data described in Chapter 5. The presented analysis is done on data collected in 2015 and 2018 during Run 2 at a centre-of-mass energy per nucleon pair $\sqrt{s_{NN}} = 5.02$ TeV. With increased statistic the data allowed a more precise measurement and it was also possible to use the luminosity to normalise the cross section, unlike in the previous paper where the $\gamma\gamma$ process simulated by STARlight was used for normalisation. This lead to a significant decrease in both the systematic and statistical uncertainties of the measurement.

The analysis was published in the paper "Coherent J/ψ photoproduction at forward rapidity in ultra-peripheral Pb-Pb collisions at $\sqrt{s_{NN}}$ = 5.02 TeV" [46] by the ALICE collaboration.

Both my own results and the published results are presented in this chapter. My results served mainly as cross checks for the official results.

6.1 Data selection

The presented analysis is based on data recorded during LHC Run 2 at a centre-of-mass energy per nucleon pair $\sqrt{s_{NN}}$ = 5.02 TeV in 2015 and 2018 Pb-Pb periods. The data was measured with the ALICE muon spectrometer in the forward rapidity region. Other detectors used for triggering, event characterisation and background suppression were AD and V0.

The analysis described below was done with ROOT scripts based on the ALICE Analysis Task library and they were executed within the AliEn environment using the ALICE computing GRID. The fitting and Toy Monte Carlo models were done using RooFit macros.

6.1.1 Run selection

The runs listed in Appendix A were selected by the ALICE Data Preparation Group (DPG) as good runs for physics analysis. This ensures that the analysed data were measured with good performing conditions of the necessary detectors and that the data reconstruction and detector calibration was performed correctly.

6.1.2 Trigger selection

The analysed events were selected with the following UPC triggers (see def. in Sec. 4.2.5):

- CMUP10-B-NOPF-MUFAST = !0VBA & !0UBA & !0UBC & 0MSL
- CMUP11-B-NOPF-MUFAST = !0VBA & !0UBA & !0UBC & 0MUL

The two triggers were merged by offline requirement of 0MUL for all events, which is the unlike sign di-muon over low p_T threshold in muon trigger.

6.1.3 Track selection

Listed below is the summary of requirements requested to ensure high quality of the selected events with characteristic typical for ultra-peripheral collisions.

Event selection criteria:

- No signal in V0A - to suppress hadronic events and ensure exclusive production of the dimuon.
- Maximum of two cells fired in V0C - corresponding to the maximum of two muon tracks expected in the forward spectrometer. However, as the acceptance of the V0C detector is smaller than the acceptance of the muon spectrometer, it is possible that some of the muon tracks are not seen by the V0C detector, hence only the maximum limit is required.
- No signal in ADA and ADC - to suppress hadronic events and ensure exclusive production of the dimuon.
- Exactly two unlike-sign tracks in the muon spectrometer - to suppress hadronic events and ensure exclusive production of the dimuon.

Track selection criteria:

- Pseudorapidity of muon tracks: $-4.0 < \eta < -2.5$ - to fit within the acceptance of the muon spectrometer.
- Both of the muon tracks matched to the muon trigger above the p_T threshold 1 GeV/c - to make sure that the reconstructed muons are coming from vector meson decay as such muons are characterised with higher p_T when compared to background.

- Cut on six σ for p$\times$DCA passed for both muon tracks - events coming from the interaction point in beam-beam timing have a Gaussian distribution in this variable unlike the beam-gas background which is suppressed by this requirement.
- Radial position of the muon tracks at the end of the absorber: $17.5.cm < R_{abs} < 89.5cm$ - to assure that the track lies within the muon spectrometer acceptance.

Dimuon selection criteria:

- Rapidity of dimuon: $-4.0 < y < -2.5$ - corresponding to the forward muon spectrometer acceptance.
- Transversal momentum of dimuon: $p_T < 0.25$ GeV/c for mass fit - to enrich the analysed sample with coherently produced J/ψ which are characterised by low p_T.
- Mass of dimuon: $2.85 < m < 3.35$ GeV/c^2 for p_T fit - the obtain the p_T spectra within the J/ψ invariant mass range.

6.2 Models for signal extraction

6.2.1 Invariant mass spectrum

Vector meson peak description

The J/ψ and ψ' peaks in the invariant mass spectrum were described with Crystal Ball function[47] which is defined as

$$\begin{aligned} f(x;\alpha,n,\bar{x},\sigma) &= e^{-\frac{1}{2}\left(\frac{x-\bar{x}}{\sigma}\right)^2} && \text{for} \quad \frac{x-\bar{x}}{\sigma} > -\alpha, \\ &= \left(\frac{n}{|\alpha|}\right)^n e^{-\frac{|\alpha|^2}{2}} \left(\frac{n}{|\alpha|} - |\alpha| - \frac{x-\bar{x}}{\sigma}\right)^{-n} && \text{for} \quad \frac{x-\bar{x}}{\sigma} \leq -\alpha. \end{aligned} \tag{6.1}$$

The function is composed from a Gaussian core with a power law times exponential tail. The tail is parametrised by two parameters α and n and it corrects for the radiation losses of the particles within the detector.

Dimuon continuum description

The dimuon continuum caused by the two photon process is described with the function [48]

$$\begin{aligned} f(x;\lambda,x_0,a_2,a_3,a_4) &= e^{\lambda x} && \text{for} \quad x > x_0, \\ &= e^{\lambda x}[1+a_2(x-x_0)^2+a_3(x-x_0)^3+a_4(x-x_0)^4] && \text{for} \quad x \leq x_0, \end{aligned} \tag{6.2}$$

where $x_0 = 4$ GeV/c^2. The background continuum has a typical exponential shape. However, at lower invariant masses the spectrum is modified due to decreasing efficiency of the ALICE trigger for this kinematic region. This decrease is parametrised by a fourth order polynomial and the transitions is determined by the x_0 variable.

6.2.2 Transverse momentum spectrum

The transverse momentum distribution was described by templates based on distributions simulated with the STARlight Monte Carlo generator. The generated events were passed through a simulation of the ALICE detector including time varying variables throughout different runs. The processes simulated by STARlight were coherent J/ψ photoproduction, incoherent J/ψ photoproduction, coherent feed-down contribution from ψ' photoproduction, incoherent feed-down contribution from ψ' photoproduction and $\gamma\gamma$ process producing dimuons.

The incoherent J/ψ production with subsequent nucleon dissociation cannot be modelled with STARlight. Therefore, to describe this part of the spectrum a parametrisation from the H1 collaboration describing J/ψ photoproduction with proton dissociation was used [49]

$$\frac{d\sigma}{dt} = N_{pd} p_T (1 + \frac{b_{pd}}{n_{pd}} p_T^2)^{-n_{pd}}, \tag{6.3}$$

where N_{pd} is the normalisation parameter, $n_{pd} = 3.58 \pm 0.15$ and $b_{pd} = 1.79 \pm 0.12$ (GeV/c)$^{-2}$, which are values measured by the H1 collaboration [49].

6.3 Invariant mass fit

For the J/ψ and ψ' peaks were used two Crystal Ball functions. The tail parameters α and n_{cb} were the same for both functions and they were left free. The mass of the ψ' was fixed to the J/ψ mass as

$$m_{\psi'} = m_{J/\psi} + 3.68609 - 3.096916, \tag{6.4}$$

where 3.68609 and 3.096916 are the masses of the respective resonances taken from Particle Data Group (PDG) [50]. The width of the ψ' peak was fixed to

$$\sigma_{\psi'} = \sigma_{\mathrm{J}/\psi} \cdot (\sigma_{\psi'}^{MC} / \sigma_{\mathrm{J}/\psi}^{MC}), \tag{6.5}$$

where the ratio $\sigma_{\psi'}^{MC} / \sigma_{\mathrm{J}/\psi}^{MC} \sim 1.09$ is from the STARlight simulation. The mass ($m_{\mathrm{J}/\psi}$) and width ($\sigma_{\mathrm{J}/\psi}$) for the J/ψ peak are left as free parameters. The normalisations for both of the Crystal Ball functions are left as a free parameter.

The $\gamma\gamma$ continuum is fitted with the function in Eq. 6.2. The parameters a_1, a_2 and a_3 were fixed to values obtained from a fit to Monte Carlo data. The parameter λ and the normalisation parameter were left free.

The invariant mass fit was done with the cut $p_T < 0.25$ GeV/c to enrich the sample with coherent events. The invariant mass fit for full rapidity range can be seen in Fig. 6.1 and for six rapidity intervals in Fig. 6.2. The number of extracted events, denoted in the plots, is in agreement with the results presented in [46].

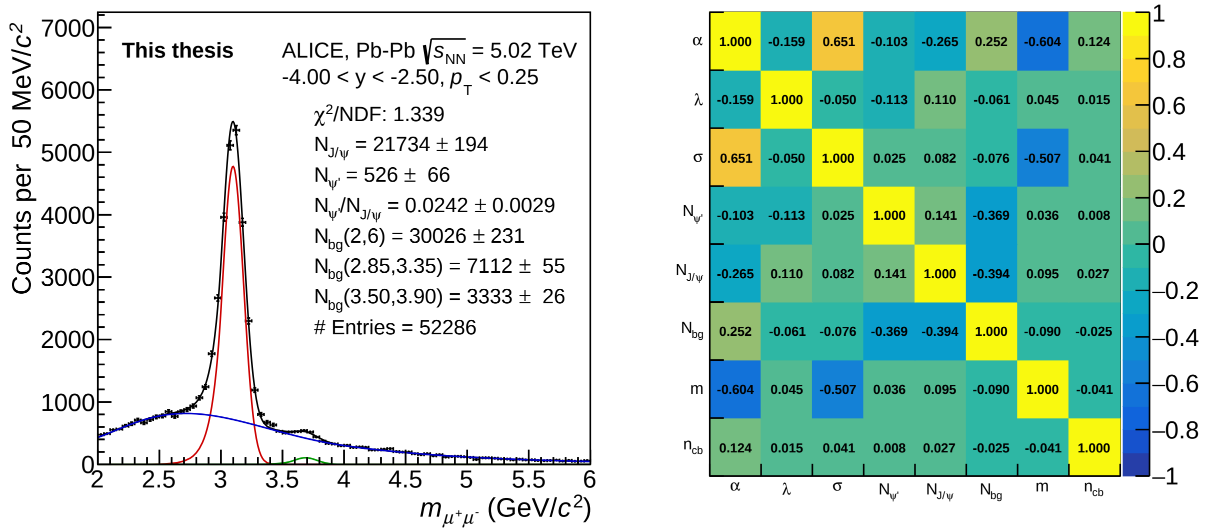

Figure 6.1: Invariant mass distribution of unlike-sign dimuons in the full rapidity range measured with the ALICE detector at $\sqrt{s_{NN}}$ = 5.02 TeV satisfying the criteria described in the text. The blue line describes the two photon continuum, the red line describes the J/ψ peak and the green line describes the ψ' peak. The number of J/ψ, ψ' and background events in different intervals is denoted in the graph. On the right side is the correlation matrix of the fit parameters.

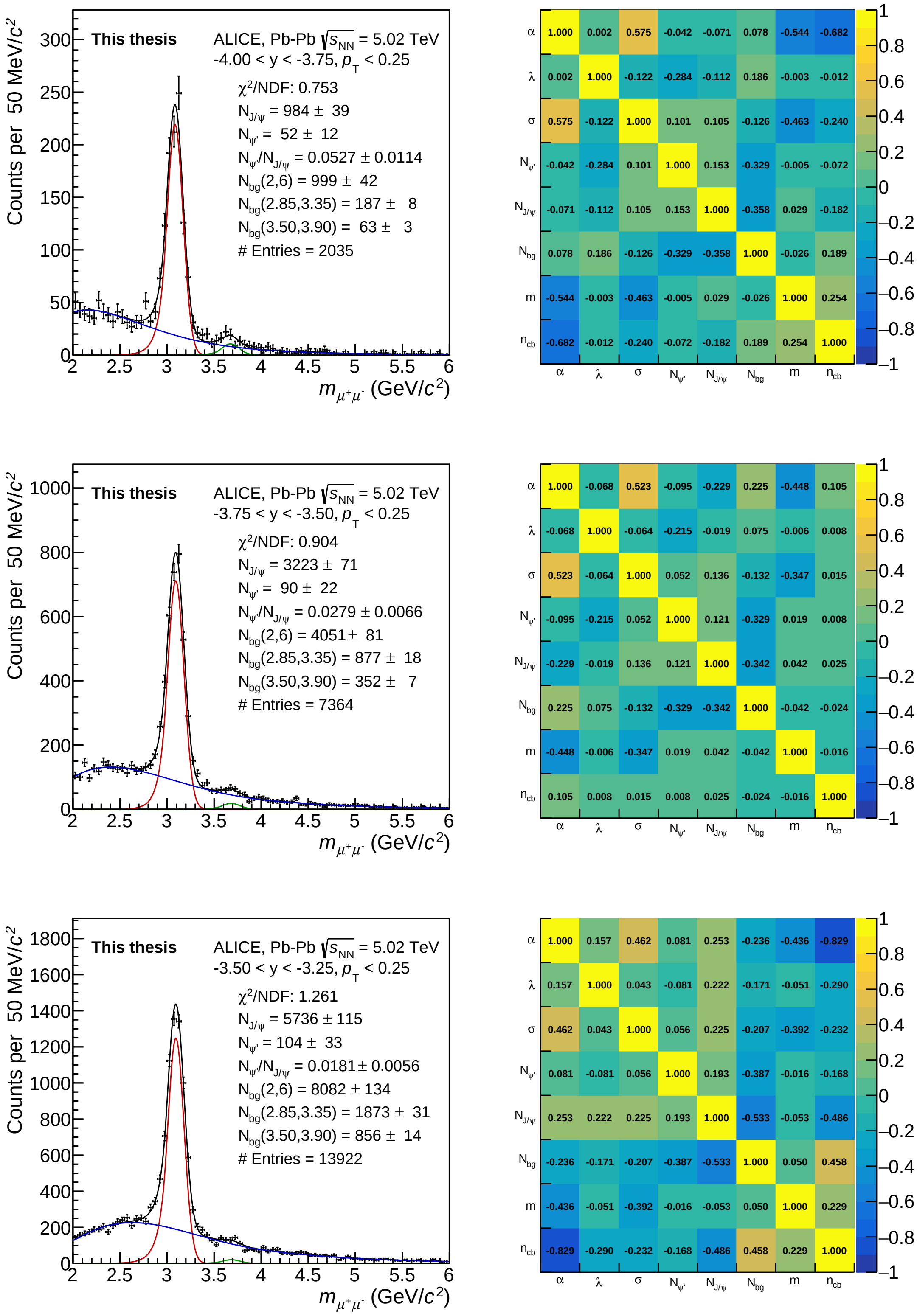

Figure 6.2: Invariant mass distribution of unlike-sign dimuons in the first three rapidity bins measured with the ALICE detector at $\sqrt{s_{NN}}$ = 5.02 TeV satisfying the criteria described in the text.

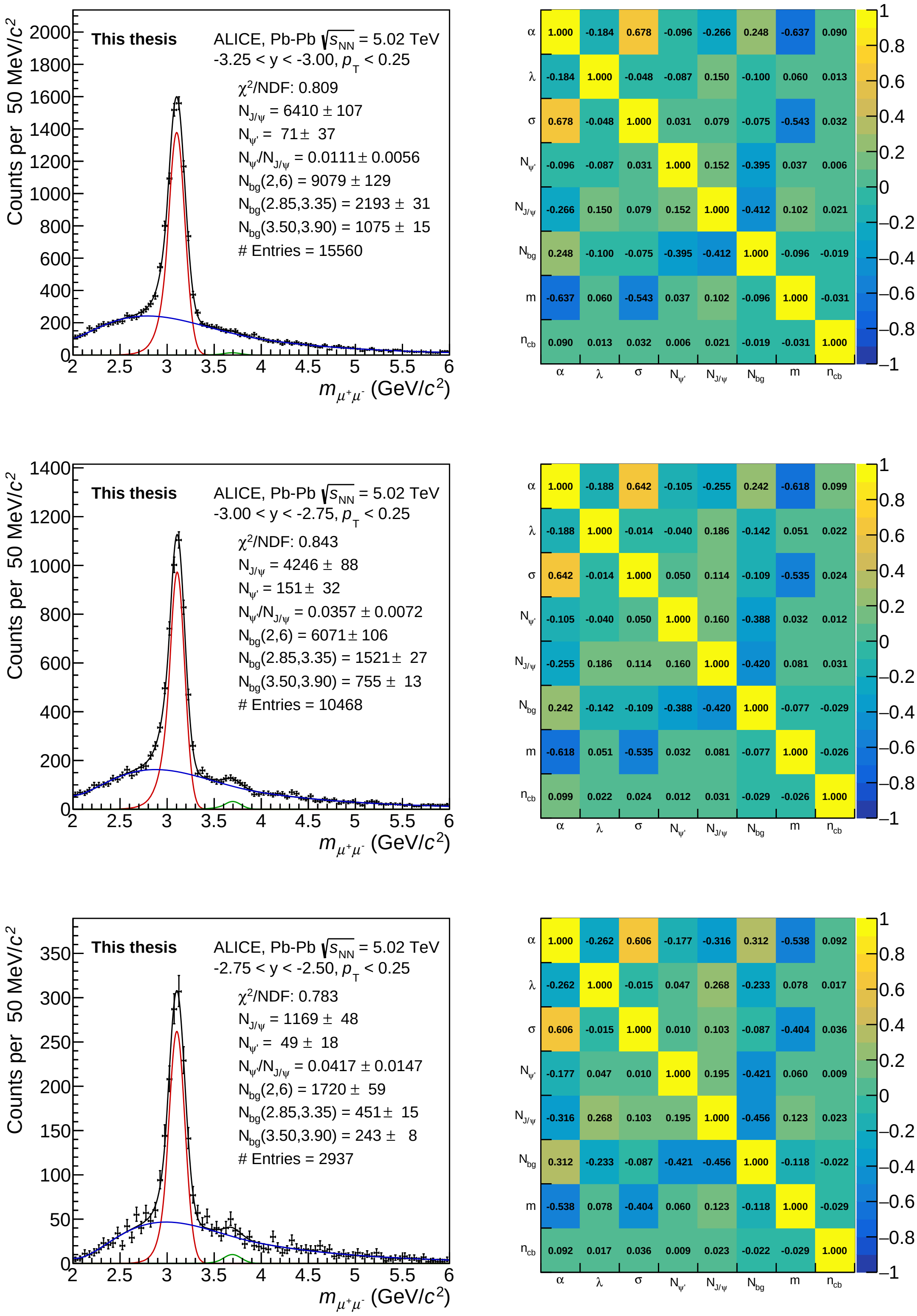

Figure 6.2: Invariant mass distribution of unlike-sign dimuons in the second three rapidity bins measured with the ALICE detector at $\sqrt{s_{NN}}$ = 5.02 TeV satisfying the criteria described in the text.

6.3.1 Ratio of ψ' to J/ψ

The ratio of the number of ψ' to J/ψ events depending on the selected rapidity bin can be seen in left part of Fig. 6.3. No strong dependence of the ratio on rapidity is expected for the involved processes. However, there is a decease of the ratio observed in the middle of our rapidity interval and an increase of the ratio for the edges of our rapidity interval when compared to the ratio obtained from the fit to the full rapidity range.

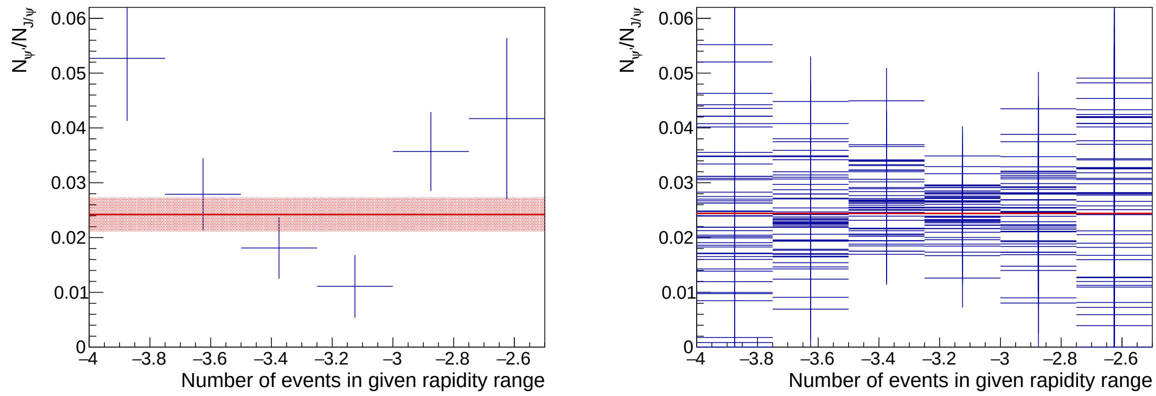

Figure 6.3: Ratio of the number of ψ' to J/ψ events depending on the number of events in the selected rapidity bin. Left: For real data with the read line denoting the measured value for the whole rapidity range 0.0242 ± 0.0029. Right: For Toy Monte Carlo data sample with number of events corresponding to the number of events in real data in the relevant rapidity bins. Each rapidity bin has been simulated and extracted 50 times. The red line denotes the input value for the ratio in the model.

To examine this variation a Toy Monte Carlo data sample was simulated with RooFit. This models consists of two Crystal Ball functions with parameters consistent with those seen in data for the full rapidity range and a background function also having the same parameters as in the full rapidity range data. This results in the ratio of the number of ψ' to J/ψ events being fixed in the model to value 0.0244.

With this model were simulated six data samples each containing the same number of events as is the number of events seen in real data in the six rapidity bins. These data samples were then fitted and the ratio of ψ' to J/ψ events was extracted. This process was repeated 50 times and the results can be seen on the right side of Fig. 6.3.

The results shows that the observed fluctuation is within the statistical precision of the extraction method. Unfortunately, this does not exclude the possibility of a systematic effect being the cause of such a behaviour.

6.3.2 Feed down contribution

The number of extracted J/ψ events is not the number of primary J/ψ created in the photoproduction process. There is a feed down contribution coming from decays $\psi' \to \mathrm{J}/\psi$+anything. To compute this contribution one first computes the ratio of ψ' to J/ψ events. The value from the fit to the full rapidity range is

$$R_N = \frac{N_{\psi'}}{N_{\mathrm{J}/\psi}} = 0.0242 \pm 0.0029, \tag{6.6}$$

which is consistent with the value found in [46]. This ratio in data can be expressed as the ratio of the primary ψ' events decaying to dimuons and the sum of primary J/ψ events decaying to dimuons together with the ψ' decaying to J/ψ which is decaying to dimuons. When the efficiencies are also taken into account one can express the R_N as

$$\begin{aligned} R_N = & \frac{N(\psi' \to \mu\mu)}{N(\mathrm{J}/\psi \to \mu\mu) + N(\psi' \to \mathrm{J}/\psi \to \mu\mu)} = \\ = & \frac{\sigma(\psi')BR(\psi' \to \mu\mu)\varepsilon(\psi')}{\sigma(\mathrm{J}/\psi)BR(\mathrm{J}/\psi \to \mu\mu)\varepsilon(\mathrm{J}/\psi) + \sigma(\psi')BR(\psi' \to \mathrm{J}/\psi)\varepsilon(\psi' \to \mathrm{J}/\psi)BR(\mathrm{J}/\psi \to \mu\mu)}, \end{aligned} \tag{6.7}$$

where the values for the branching taken from PDG [50] ratios are $BR(\mathrm{J}/\psi \to \mu\mu) = (5.961 \pm 0.033)\%$, $BR(\psi' \to \mu\mu) = (0.80 \pm 0.06)\%$, $BR(\psi' \to \mathrm{J}/\psi + \text{anything}) = (61.4 \pm 0.6)\%$ and the values for the efficiency correction are determined using the STARlight data sets. The values taken from [46] are $\varepsilon(\mathrm{J}/\psi) = 12.0\%$, $\varepsilon(\psi') = 15.8\%$ and $\varepsilon(\psi' \to \mathrm{J}/\psi) = 7.2\%$. With all the above values known, it is possible to compute the ratio of the primary ψ' and J/ψ photoproduction cross section ratio as

$$R = \frac{\sigma(\psi')}{\sigma(\mathrm{J}/\psi)} = \frac{R_N BR(\mathrm{J}/\psi \to \mu\mu)\varepsilon(\mathrm{J}/\psi)}{BR(\psi' \to \mu\mu)\varepsilon(\psi') + R_N BR(\psi' \to \mathrm{J}/\psi)\varepsilon(\psi' \to \mathrm{J}/\psi)BR(\mathrm{J}/\psi \to \mu\mu)}. \tag{6.8}$$

The ratio of feed down and primary J/ψ is then computed as

$$f_{\mathrm{D}} = \frac{N(\text{feed down J}/\psi)}{N(\text{primary J}/\psi)} = \frac{\sigma(\psi')\varepsilon(\psi' \to \mathrm{J}/\psi)BR(\psi' \to \mathrm{J}/\psi)}{\sigma(\mathrm{J}/\psi)\varepsilon(\mathrm{J}/\psi)} = (5.3 \pm 0.7)\%, \tag{6.9}$$

which is value for the full rapidity range and it is consistent with the value presented in [46].

6.4 Transverse momentum fit

Templates made from the Monte Carlo data sets were used to describe the different contributions in the transverse momentum spectrum. RooFit Probability Density Functions (PDF) were created by fitting the STARlight simulated distributions.

The fitting model for the p_T spectrum consists of a sum of templates for the coherent J/ψ, incoherent J/ψ, coherent feed down from ψ', incoherent feed down from ψ', $\gamma\gamma \rightarrow \mu\mu$ and the incoherent J/ψ production with nucleon dissociation distribution from Eq. 6.3.

The normalisation for the coherent and incoherent feed-down contributions from ψ' were fixed to the values of primary coherent and incoherent J/ψ by the feed down ratio f_D. However, the value for f_D for the p_T fit has to be computed without the $p_T < 0.25$ GeV/c cut. The corresponding value was taken from [46] and it is $f_D = (8.5 \pm 1.5)\%$.

The $\gamma\gamma$ template normalisation was fixed to the number of background events in the invariant mass fit. The parameters of the incoherent J/ψ production with nucleon dissociation distribution were fixed to values $n_{pd} = 3.58 \pm 0.15$ and $b_{pd} = 1.79 \pm 0.12$ (GeV/c)$^{-2}$ measured by the H1 collaboration [49].

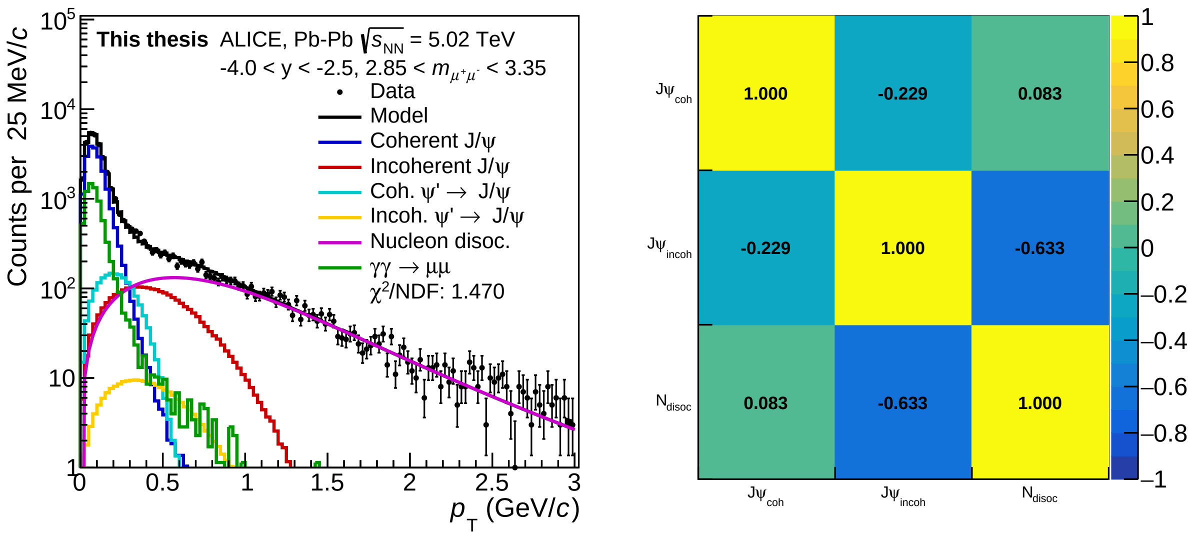

Figure 6.4: Transverse momentum distribution of unlike-sign dimuons in the full rapidity range measured with the ALICE detector at $\sqrt{s_{NN}}$ = 5.02 TeV satisfying the criteria described in the text. The blue line describes the coherent J/ψ, the red line describes the incoherent J/ψ, the cyan line describes the coherent feed down from ψ', the orange line describes the incoherent feed down from ψ', the magenta line describes the incoherent J/ψ with nucleon dissociation and the green line describes the two photon process. On the right side is the correlation matrix of the fit parameters.

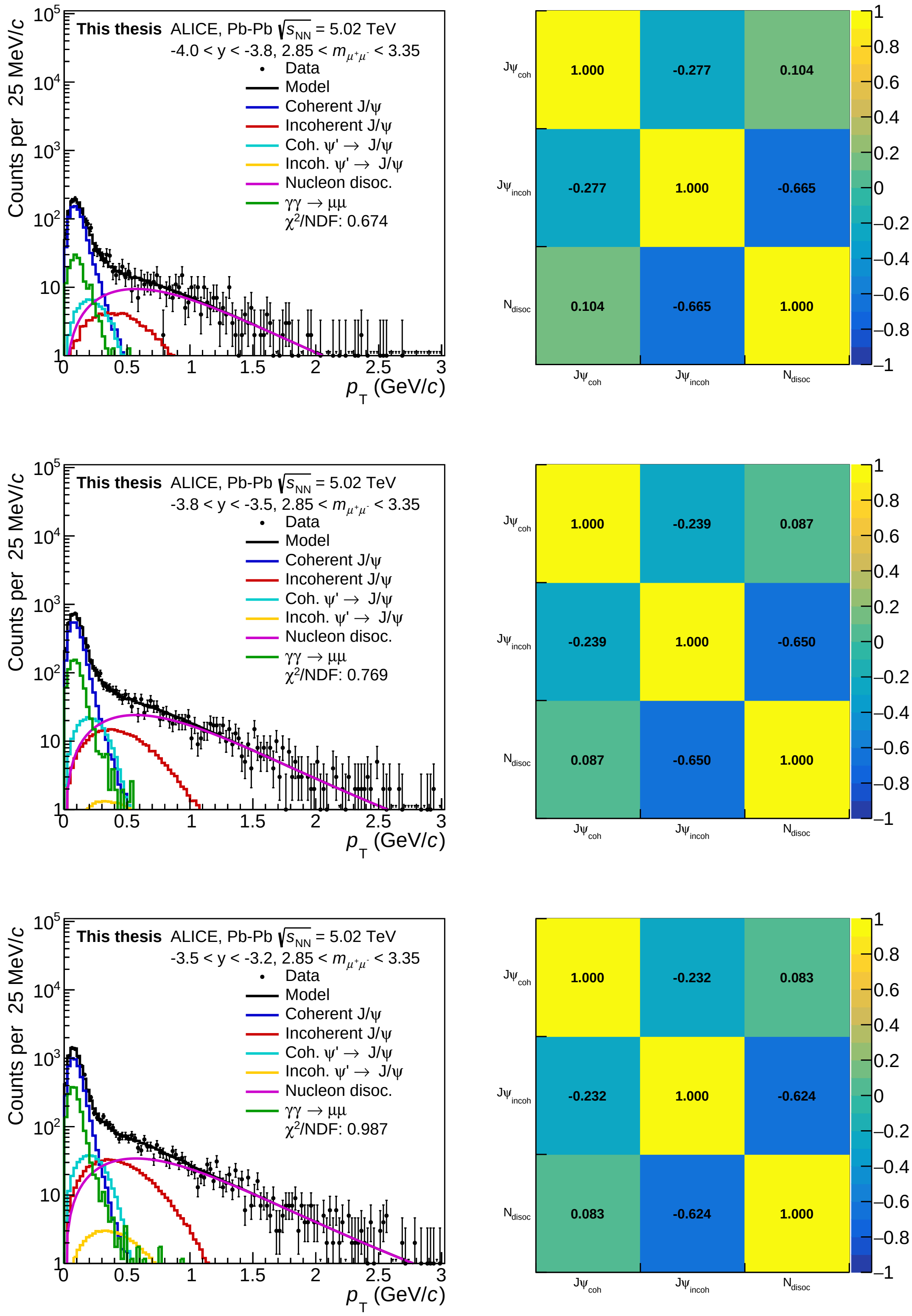

Figure 6.5: Transverse momentum distribution of unlike-sign dimuons in the first three rapidity bins measured with the ALICE detector at $\sqrt{s_{NN}}$ = 5.02 TeV satisfying the criteria described in the text.

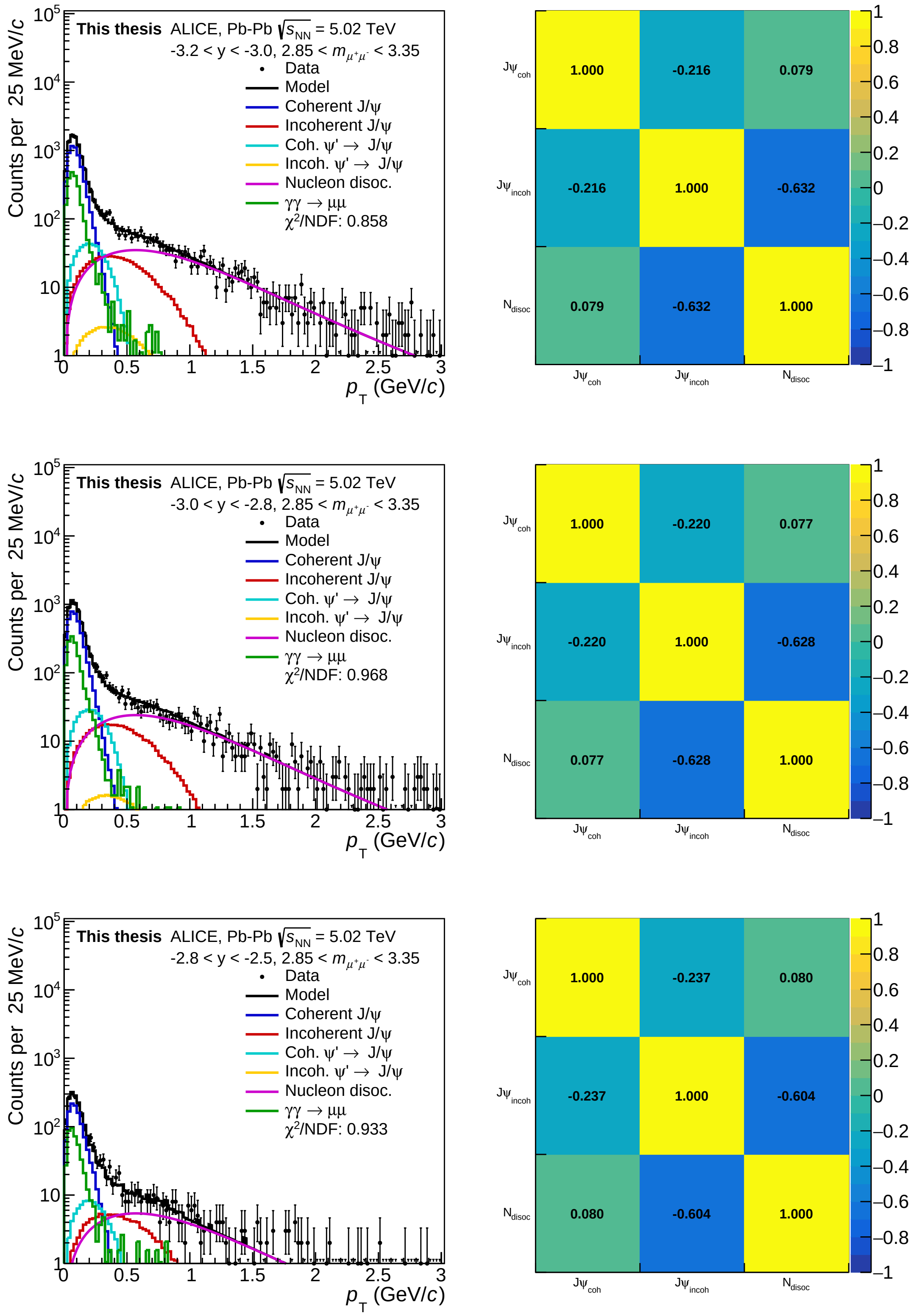

Figure 6.5: Transverse momentum distribution of unlike-sign dimuons in the second three rapidity bins measured with the ALICE detector at $\sqrt{s_{NN}}$ = 5.02 TeV satisfying the criteria described in the text.

The only parameters left free in the transverse momentum distribution fit were the normalisations of the coherent J/ψ contribution, incoherent J/ψ contribution and the incoherent production with nucleon dissociation. These three processes are well separated by the p_T distribution shapes.

The p_T fit in the J/ψ invariant mass range $2.85 < m < 3.35$ GeV/c^2 for the full rapidity interval can be seen in Fig. 6.4 and for six rapidity intervals in Fig. 6.5.

6.4.1 Incoherent contribution

The number of J/ψ events extracted from the invariant mass fit is not the number of coherent J/ψ events. There are also contributions form the incoherent events. The fraction of the incoherent over coherent events can be computed as

$$f_{\mathrm{I}} = \frac{N(\mathrm{incoh}\ J/\psi)}{N(\mathrm{coh}\ J/\psi)} = \frac{J/\psi_{\mathrm{incoh}} + \text{feed down } J/\psi_{\mathrm{incoh}} + \text{dissociative } J/\psi_{\mathrm{incoh}}}{J/\psi_{\mathrm{coh}} + \text{feed down } J/\psi_{\mathrm{coh}}} = (5.1 \pm 0.3)\%, \tag{6.10}$$

for $p_T < 0.25$ GeV/c. This value is compatible with the one found in [46].

6.5 Cross section

The cross section for coherent J/ψ photoproduction can be computed as

$$\frac{\mathrm{d}\sigma^{\mathrm{coh}}_{J/\psi}}{\mathrm{dy}} = \frac{N(J/\psi)}{(1 + f_{\mathrm{I}} + f_{\mathrm{D}})\varepsilon(J/\psi)\mathrm{BR}(J/\psi \to \mu\mu)\varepsilon_{\mathrm{veto}}\mathrm{L_{int}}\Delta\mathrm{y}}, \tag{6.11}$$

where $N(J/\psi)$ is the number of extracted J/ψ events from the invariant mass fit, $(1 + f_{\mathrm{I}} + f_{\mathrm{D}})$ account for the fraction of feed down and incoherent events, $\varepsilon_{\mathrm{veto}}$ is the veto efficiency, $\mathrm{L_{int}}$ is the integrated luminosity and Δy is the size of the rapidity interval.

The integrated luminosity values are taken from [46] as 216 $\mu\mathrm{b}^{-1}$ for 2015 data and 538 $\mu\mathrm{b}^{-1}$ for 2018 data. The veto inefficiency due to electromagnetic pileup was studied with unbiased trigger only on the timing of bunch crossing in the interaction point. The final veto inefficiency was determined by luminosity weighting the veto rejection probabilities over periods with different pileup. The average veto efficiency correction factor is taken from [46] as $\varepsilon_{\mathrm{veto}} = 95.0\%$.

Taking the abovementioned values the coherent J/ψ photoproduction cross section is computed to be $\frac{\mathrm{d}\sigma^{\mathrm{coh}}_{J/\psi}}{\mathrm{dy}} = (2.561 \pm 0.023)$ mb. This value is consistent with the value presented in [46].

A summary of the published results for the J/ψ yields, efficiencies, f_{I} and f_{D} fractions and the coherent J/ψ cross sections for all the rapidity intervals taken from the paper [46] can be found in Table 6.1.

rapidity range	$N_{J/\psi}$	ε	f_D	f_I	$d\sigma^{coh}_{J/\psi}/dy$ (mb)
$(-4.00, -2.50)$	21747 ± 190	0.120	0.055	0.055	2.549 ± 0.022 (stat.) $^{+0.209}_{-0.237}$ (syst.)
$(-4.00, -3.75)$	974 ± 36	0.051	0.055	0.060	1.621 ± 0.061 (stat.) $^{+0.135}_{-0.148}$ (syst.)
$(-3.75, -3.50)$	3217 ± 70	0.140	0.055	0.059	1.936 ± 0.042 (stat.) $^{+0.166}_{-0.190}$ (syst.)
$(-3.50, -3.25)$	5769 ± 98	0.204	0.055	0.061	2.376 ± 0.040 (stat.) $^{+0.212}_{-0.229}$ (syst.)
$(-3.25, -3.00)$	6387 ± 105	0.191	0.055	0.052	2.830 ± 0.047 (stat.) $^{+0.253}_{-0.280}$ (syst.)
$(-3.00, -2.75)$	4229 ± 85	0.119	0.055	0.051	3.014 ± 0.061 (stat.) $^{+0.259}_{-0.294}$ (syst.)
$(-2.75, -2.50)$	1190 ± 47	0.029	0.054	0.032	3.585 ± 0.141 (stat.) $^{+0.298}_{-0.368}$ (syst.)

Table 6.1: J/ψ yields, efficiencies, f_I and f_D fractions and coherent J/ψ cross sections [46].

A study on systematic uncertainties was done in the paper [46]. Among other things it studied the effect of adding a veto for the Silicon Pixel Detector (SPD) consisting of two concentric cylindrical layers of silicon pixel chips. The veto demanded no track segments between the two detector layers. It also studied a possible missing contribution in the $\gamma\gamma$ p_T template. STARlight does not simulate photons which are emitted incoherently by the source ion. These have much wider p_T distribution. To account for them, the shape of the $\gamma\gamma$ p_T template was extracted from the side bands around the J/ψ peak in the invariant mass spectra. A summary of all systematic uncertainty contributions computed in the paper [46] can be seen in Table 6.2.

Source	Value
Lumi. normalisation	$\pm 5.0\%$
SPD, V0 and AD veto	from -3.6% to -6.0%
Branching ratio	$\pm 0.6\%$
MC rapidity shape	from $\pm 0.1\%$ to $\pm 0.8\%$
Tracking	$\pm 3.0\%$
Trigger	from $\pm 5.2\%$ to $\pm 6.2\%$
Matching	$\pm 1.0\%$
f_D fraction	$\pm 0.7\%$
Signal extraction	$\pm 2.0\%$
$\gamma\gamma$ yield	$\pm 1.2\%$
p_T shape for coherent J/ψ	$\pm 0.1\%$
b_{pd} parameter	$\pm 0.1\%$
Total	from $^{+8.3}_{-9.2}\%$ to $^{+8.9}_{-10.3}\%$

Table 6.2: Summary of systematic uncertainties. The ranges of values correspond to different rapidity bins [46].

The comparison of the rapidity distribution of the coherent J/ψ photoproduction cross section, as computed in the paper [46], compared to theoretical models is in Fig. 6.6. The measured cross section corresponds to gluon distributions at Bjorken x in the range $1.1 \cdot 10^{-5} < x < 5.1 \cdot 10^{-5}$ or $0.7 \cdot 10^{-2} < x < 3.3 \cdot 10^{-2}$ depending on the source of the photon. However, the contribution at $x \sim 10^{-2}$ is found to be dominant [51] with the contribution of ∼60% at $y = -2.5$ up to ∼95% at $y = -4$.

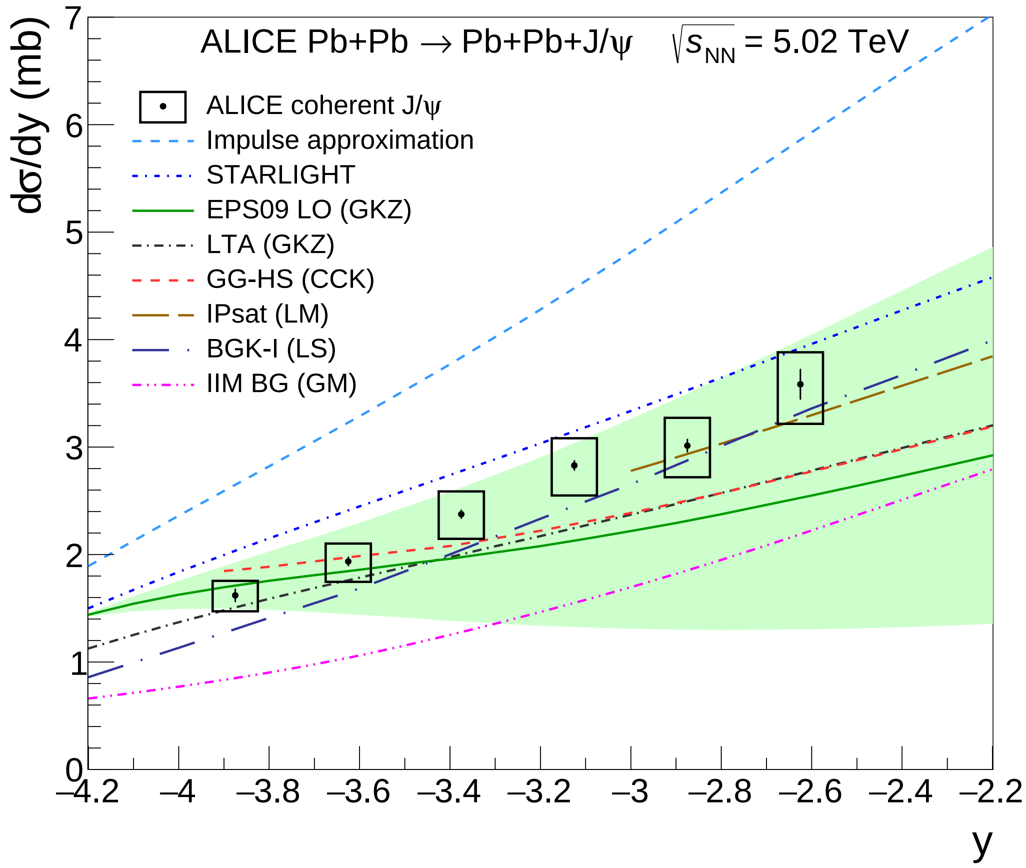

Figure 6.6: Measured coherent differential cross section of J/ψ photoproduction in ultra-peripheral Pb-Pb collisions at $\sqrt{s_{NN}}$ = 5.02 TeV. The error bars represent the statistical uncertainties, the boxes around the points the systematic uncertainties. The theoretical calculations described in the text are also shown. The green band represents the uncertainties of the EPS09 LO calculation [46].

The impulse approximation [52] is based on data of photoproduction on protons and it does not consider any nuclear effect except coherence. The STARlight [8] prediction is based on the Vector Meson Dominance model. It uses photoproduction data on protons combined with a Glauber like approach for accounting multiple scattering. Both of the above models overpredict the data, indicating the importance of gluon shadowing effects.

Guzey, Kryshen and Zhalov (GKZ) [51] provide one prediction based on the EPS09 LO parametrisation of nuclear shadowing data and a second prediction based on the Leading Twist Approximation (LTA). Gonçalves, Machado et al. (IIM BG-GM) [53, 54] and Lappi and Mäntysaari (IPsat-LM) [9, 16] provide predictions based on the colour dipole model combined with the Colour Glass Condensate (CGC) but using different parametrisation for the dipole scattering cross section. Luszczak and Schafer (LS BGK-I) [55] make predictions within the colour dipole model but using the Glauber-Gribov theory. Cepila, Contreras and Krelina (CCK) [56, 57] provide predictions based on the Hot Spot (HS) model combined with the Glauber-Gribov (GG) approach. All of these models mostly underpredict the data. Even though at some rapidity ranges the models are consistent with the data, none of them agrees with the data over the whole rapidity range.

Summary

The evolution of our understanding of the structure of proton and nucleus up to the low Bjorken x phenomenon of saturation and nuclear shadowing was presented in Chapter 1.

Ultra-peripheral collisions as a powerful tool for studying the proton and nucleus structure at high energies were introduced in Chapter 2.

Two papers making predictions for vector meson photoproduction cross section made within the colour dipole model were reviewed in Chapter 3.

The ALICE detector at the CERN LHC and its subdetectors essential for the analysis presented in this thesis were discussed in Chapter 4.

The ALICE measurement of coherent J/ψ photoproduction cross section in Pb-Pb ultra-peripheral collisions at a centre-of-mass energy per nucleon pair $\sqrt{s_{NN}}$ = 2.76 TeV was presented in Chapter 5. The comparison of the results with theoretical models indicates that nuclear shadowing is important in order to be able to describe the data.

The analysis procedure and the published results of coherent J/ψ photoproduction cross section measured in forward rapidity by ALICE in Pb-Pb ultra-peripheral collisions at a centre-of-mass energy per nucleon pair $\sqrt{s_{NN}}$ = 5.02 TeV during LHC Run 2 in 2015 and 2018 was discusses in Chapter 6. This measurement confirms the importance of nuclear gluon shadowing being included within the theoretical models in order to agree with the data. However, none of the models compared to the data was able to describe it accurately in the whole rapidity range.

In the future a study on the coherent J/ψ photoproduction cross section accompanied by a forward neutron emission may untangle the two contributions to the cross section term and provide valuable information about the gluon structure functions at Bjorken $x \sim 10^{-5}$.

Bibliography

[1] Jiří Chýla. *Quarks, partons and Quantum Chromodynamics*. Institute of Physics, Academy of Sciences of the Czech Republic, online 2019. `https://www.fzu.cz/~chyla/lectures/text.pdf`.

[2] S. Chekanov et al. A ZEUS next-to-leading-order QCD analysis of data on deep inelastic scattering. *Phys. Rev.*, D67:012007, 2003.

[3] H. Abramowicz et al. Combination of measurements of inclusive deep inelastic $e^{\pm}p$ scattering cross sections and QCD analysis of HERA data. *Eur. Phys. J.*, C75(12):580, 2015.

[4] Nestor Armesto. Nuclear shadowing. *J. Phys.*, G32:R367–R394, 2006.

[5] A. Accardi et al. Electron Ion Collider: The Next QCD Frontier. *Eur. Phys. J.*, A52(9):268, 2016.

[6] J. G. Contreras and J. D. Tapia Takaki. Ultra-peripheral heavy-ion collisions at the LHC. *Int. J. Mod. Phys.*, A30:1542012, 2015.

[7] Gerhard Baur, Kai Hencken, Dirk Trautmann, Serguei Sadovsky, and Yuri Kharlov. Coherent gamma gamma and gamma-A interactions in very peripheral collisions at relativistic ion colliders. *Phys. Rept.*, 364:359–450, 2002.

[8] Spencer R. Klein, Joakim Nystrand, Janet Seger, Yuri Gorbunov, and Joey Butterworth. STARlight: A Monte Carlo simulation program for ultra-peripheral collisions of relativistic ions. *Comput. Phys. Commun.*, 212:258–268, 2017.

[9] T. Lappi and H. Mantysaari. J/ψ production in ultraperipheral Pb+Pb and p+Pb collisions at energies available at the CERN Large Hadron Collider. *Phys. Rev.*, C87(3):032201, 2013.

[10] V. P. Goncalves and M. V. T. Machado. Vector Meson Production in Coherent Hadronic Interactions: An update on predictions for RHIC and LHC. *Phys. Rev.*, C84:011902, 2011.

[11] E. Iancu, K. Itakura, and S. Munier. Saturation and BFKL dynamics in the HERA data at small x. *Phys. Lett.*, B590:199–208, 2004.

[12] G. Soyez. Saturation QCD predictions with heavy quarks at HERA. *Phys. Lett.*, B655:32–38, 2007.

[13] Henri Kowalski and Derek Teaney. An Impact parameter dipole saturation model. *Phys. Rev.*, D68:114005, 2003.

[14] H. Kowalski, L. Motyka, and G. Watt. Exclusive diffractive processes at HERA within the dipole picture. *Phys. Rev.*, D74:074016, 2006.

[15] Cyrille Marquet. A Unified description of diffractive deep inelastic scattering with saturation. *Phys. Rev.*, D76:094017, 2007.

[16] T. Lappi and H. Mantysaari. Incoherent diffractive J/ψ-production in high energy nuclear DIS. *Phys. Rev.*, C83:065202, 2011.

[17] E. Iancu, K. Itakura, and S. Munier. Saturation and BFKL dynamics in the HERA data at small x. *Phys. Lett.*, B590:199–208, 2004.

[18] Tobias Toll and Thomas Ullrich. Exclusive diffractive processes in electron-ion collisions. *Phys. Rev.*, C87(2):024913, 2013.

[19] Carlos A. Bertulani, Spencer R. Klein, and Joakim Nystrand. Physics of ultra-peripheral nuclear collisions. *Ann. Rev. Nucl. Part. Sci.*, 55:271–310, 2005.

[20] Betty Abelev et al. Coherent J/ψ photoproduction in ultra-peripheral Pb-Pb collisions at $\sqrt{s_{NN}} = 2.76$ TeV. *Phys. Lett.*, B718:1273–1283, 2013.

[21] Christoph Mayer for the ALICE Collaboration. Cracow epiphany conference on the physics after the first phase of the LHC, 7–9.01.2013. *Conference contribution*, 2013. \http://epiphany.ifj.edu.pl/epiphany.2013/pres/day2_Mayer_ALICE_Epiphany_v4.pdf.

[22] S. Afanasiev et al. Photoproduction of J/ψ and of high mass e^+e^- in ultra-peripheral Au+Au collisions at $\sqrt{s_{\mathrm{NN}}} = 200$ GeV. *Phys. Lett.*, B679:321–329, 2009.

[23] Gerhard Baur, Kai Hencken, Dirk Trautmann, Serguei Sadovsky, and Yuri Kharlov. Coherent $\gamma\gamma$ and γA interactions in very peripheral collisions at relativistic ion colliders. *Physics Reports*, 364(5):359 – 450, 2002. \http://www.sciencedirect.com/science/article/pii/S0370157301001016.

[24] A. J. Baltz. The Physics of Ultraperipheral Collisions at the LHC. *Phys. Rept.*, 458:1–171, 2008.

[25] M. Drees and D. Zeppenfeld. Production of supersymmetric particles in elastic ep collisions. *Phys. Rev. D*, 39:2536–2546, May 1989. \https://link.aps.org/doi/10.1103/PhysRevD.39.2536.

[26] N.N. Nikolaev and B.G. Zakharov. On determination of the large-1x gluon distribution at hera. *Physics Letters B*, 332(1):184 – 190, 1994. \http://www.sciencedirect.com/science/article/pii/037026939490877X.

[27] V. P. Gonçalves and M. V. T. Machado. Nuclear exclusive vector meson photoproduction. *The European Physical Journal C - Particles and Fields*, 38(3):319–328, Dec 2004. \https://doi.org/10.1140/epjc/s2004-02044-7.

[28] J. Bartels, Krzysztof J. Golec-Biernat, and Krisztian Peters. On the dipole picture in the nonforward direction. *Acta Phys. Polon.*, B34:3051–3068, 2003.

[29] N. Armesto. A simple model for nuclear structure functions at small x in the dipole picture. *Eur. Phys. J. C*, 26(1):35–43, 2002. \https://doi.org/10.1007/s10052-002-1021-z.

[30] C. Marquet, R. Peschanski, and G. Soyez. Exclusive vector meson production at hera from qcd with saturation. *Phys. Rev. D*, 76:034011, Aug 2007. \https://link.aps.org/doi/10.1103/PhysRevD.76.034011.

[31] Anthony J. Baltz, Spencer R. Klein, and Joakim Nystrand. Coherent vector-meson photoproduction with nuclear breakup in relativistic heavy-ion collisions. *Phys. Rev. Lett.*, 89:012301, Jun 2002. \https://link.aps.org/doi/10.1103/PhysRevLett.89.012301.

[32] K. Aamodt et al. The ALICE experiment at the CERN LHC. *JINST*, 3:S08002, 2008.

[33] Esma Mobs. The CERN accelerator complex - August 2018. Complexe des accélérateurs du CERN - Août 2018. *OPEN-PHO-ACCEL-2018-005*, Aug 2018. General Photo, https://cds.cern.ch/record/2636343.

[34] Arturo Tauro. ALICE Schematics. General Photo, [Online; accessed 29-June-2017], Available at: http://cds.cern.ch/record/2263642, May 2017.

[35] Christophe Suire. Installation of station 1 of the tracking chambers of the ALICE Muon Spectrometer. ALICE Collection, http://cds.cern.ch/record/1046255, Mar 2007.

[36] Mona Schweizer. One of the two Zero Degree Calorimeter installed in the LHC tunnel near the ALICE cavern. http://cds.cern.ch/record/1087658, Jan 2008.

[37] ALICE Zero Degree Calorimeter (ZDC), General Pictures. ALICE Collection, http://cds.cern.ch/record/630193, Jun 2003.

[38] C Cicalo. ALICE Zero Degree Calorimeter(ZDC) Construction of the first proton calorimeter. ALICE Collection, http://cds.cern.ch/record/777329, Jul 2004.

[39] G. Herrera Corral. Diffractive Physics with ALICE at the LHC: the control of quantum collisions. *J. Phys. Conf. Ser.*, 624(1):012008, 2015.

[40] Vardan Khachatryan et al. Coherent J/ψ photoproduction in ultra-peripheral PbPb collisions at $\sqrt{s_{NN}} = 2.76$ TeV with the CMS experiment. *Phys. Lett.*, B772:489–511, 2017.

[41] Jaroslav Adam et al. Measurement of an excess in the yield of J/ψ at very low p_T in Pb-Pb collisions at $\sqrt{s_{NN}}$ = 2.76 TeV. *Phys. Rev. Lett.*, 116(22):222301, 2016.

[42] Tomáš Herman. Measurement of coherent J/ψ photoproduction in pb-pb collisions with alice. Research project, Czech Technical University in Prague - Faculty of Nuclear Sciences and Physical Engineering, 2018. `https://physics.fjfi.cvut.cz/publications/ejcf/VU_Tomas_Herman.pdf`.

[43] E. Abbas et al. Charmonium and e^+e^- pair photoproduction at mid-rapidity in ultra-peripheral Pb-Pb collisions at $\sqrt{s_{\mathrm{NN}}}$=2.76 TeV. *Eur. Phys. J.*, C73(11):2617, 2013.

[44] Tomáš Herman. Signal extraction in J/ψ photoproduction in the alice experiment. Bachelor's thesis, Czech Technical University in Prague - Faculty of Nuclear Sciences and Physical Engineering, 2017. `https://physics.fjfi.cvut.cz/publications/ejcf/bp_ejcf_17_herman.pdf`.

[45] Betty Abelev et al. Coherent J/ψ photoproduction in ultra-peripheral Pb-Pb collisions at $\sqrt{s_{NN}} = 2.76$ TeV. *Phys. Lett.*, B718:1273–1283, 2013.

[46] Shreyasi Acharya et al. Coherent J/ψ photoproduction at forward rapidity in ultra-peripheral Pb-Pb collisions at $\sqrt{s_{\mathrm{NN}}} = 5.02$ TeV. 2019. arXiv:1904.06272.

[47] John Erthal Gaiser. *Charmonium Spectroscopy From Radiative Decays of the* J/ψ *and* ψ'. PhD thesis, SLAC, 1982. `\http://www-public.slac.stanford.edu/sciDoc/docMeta.aspx?slacPubNumber=slac-r-255.html`.

[48] E. Kryshen K. Graham, O.V. Baillie. Forward J/ψ photoproduction in ultra-peripheral Pb-Pb collisions at $\sqrt{s_{NN}} = 5.02$ TeV. February 2017. Draft of an ALICE analysis note.

[49] C. Alexa et al. Elastic and Proton-Dissociative Photoproduction of J/ψ Mesons at HERA. *Eur. Phys. J.*, C73(6):2466, 2013.

[50] M. Tanabashi et al. Review of Particle Physics. *Phys. Rev.*, D98(3):030001, 2018.

[51] V. Guzey, E. Kryshen, and M. Zhalov. Coherent photoproduction of vector mesons in ultraperipheral heavy ion collisions: Update for run 2 at the CERN Large Hadron Collider. *Phys. Rev.*, C93(5):055206, 2016.

[52] Spencer Klein and Joakim Nystrand. Exclusive vector meson production in relativistic heavy ion collisions. *Phys. Rev.*, C60:014903, 1999.

[53] V. P. Goncalves, B. D. Moreira, and F. S. Navarra. Investigation of diffractive photoproduction of J/Ψ in hadronic collisions. *Phys. Rev.*, C90(1):015203, 2014.

[54] G. Sampaio dos Santos and M. V. T. Machado. On theoretical uncertainty of color dipole phenomenology in the J/ψ and Υ photoproduction in pA and AA collisions at the CERN Large Hadron Collider. *J. Phys.*, G42(10):105001, 2015.

[55] Agnieszka Łuszczak and Wolfgang Schäfer. Coherent photoproduction of J/ψ in nucleus-nucleus collisions in the color dipole approach. *Phys. Rev.*, C99(4):044905, 2019.

[56] J. Cepila, J. G. Contreras, and J. D. Tapia Takaki. Energy dependence of dissociative J/ψ photoproduction as a signature of gluon saturation at the LHC. *Phys. Lett.*, B766:186–191, 2017.

[57] Jan Cepila, Jesus Guillermo Contreras, and Michal Krelina. Coherent and incoherent J/ψ photonuclear production in an energy-dependent hot-spot model. *Phys. Rev.*, C97(2):024901, 2018.

Appendix A

Lists of run numbers

Lists of good runs used in the presented analysis are given below.

Good runs for period LHC15o - NanoAOD 406 20181102-2241 - muon_calo_pass1:

244918, 244980, 244982, 244983, 245064, 245066, 245068, 245145, 245146, 245151, 245152, 245231, 245232, 245233, 245253, 245259, 245343, 245345, 245346, 245347, 245353, 245401, 245407, 245409, 245410, 245446, 245450, 245496, 245501, 245504, 245505, 245507, 245535, 245540, 245542, 245543, 245554, 245683, 245692, 245700, 245705, 245729, 245731, 245738, 245752, 245759, 245766, 245775, 245785, 245793, 245829, 245831, 245833, 245949, 245952, 245954, 245963, 245996, 246001, 246003, 246012, 246036, 246037, 246042, 246048, 246049, 246053, 246087, 246089, 246113, 246115, 246148, 246151, 246152, 246153, 246178, 246181, 246182, 246217, 246220, 246222, 246225, 246272, 246275, 246276, 246390, 246391, 246392, 246424, 246428, 246431, 246433, 246434, 246487, 246488, 246493, 246495, 246675, 246676, 246750, 246751, 246755, 246757, 246758, 246759, 246760, 246763, 246765, 246804, 246805, 246806, 246807, 246808, 246809, 246844, 246845, 246846, 246847, 246851, 246855, 246859, 246864, 246865, 246867, 246871, 246930, 246937, 246942, 246945, 246948, 246949, 246980, 246982, 246984, 246989, 246991, 246994

Good runs for period LHC18q - NanoAOD 425 20190111-1316 - muon_calo_pass2:

295585, 295586, 295587, 295588, 295589, 295612, 295615, 295665, 295666, 295667, 295668, 295671, 295673, 295675, 295676, 295677, 295714, 295716, 295717, 295718, 295719, 295723, 295725, 295753, 295754, 295755, 295758, 295759, 295762, 295763, 295786, 295788, 295791, 295816, 295818, 295819, 295822, 295825, 295826, 295829, 295831, 295854, 295855, 295856, 295859, 295860, 295861, 295863, 295881, 295908, 295909, 295910, 295913, 295936, 295937, 295941, 295942, 295943, 295945, 295947, 296061, 296062, 296063, 296065, 296066, 296068, 296123, 296128, 296132, 296133, 296134, 296135, 296142, 296143, 296191, 296192, 296194, 296195, 296196, 296197, 296198, 296241, 296242, 296243, 296244, 296246, 296247, 296269, 296270, 296273, 296279, 296280, 296303, 296304, 296307, 296309, 296312, 296377, 296378, 296379, 296380, 296381, 296383, 296414, 296419, 296420, 296423, 296424, 296433, 296472, 296509, 296510, 296511, 296514, 296516, 296547, 296548, 296549, 296550, 296551, 296552, 296553, 296615, 296616, 296618, 296619, 296622, 296623

Good runs for periodLHC18r - NanoAOD 426 20190111-1316 - muon_calo_pass2:

296690, 296691, 296694, 296749, 296750, 296781, 296784, 296785, 296786, 296787, 296791, 296793, 296794, 296799, 296836, 296838, 296839, 296848, 296849, 296850, 296851, 296852, 296890, 296894, 296899, 296900, 296903, 296930, 296931, 296932, 296934, 296935, 296938, 296941, 296966, 296967, 296968, 296969, 296971, 296975, 296976, 296979, 297029, 297031, 297035, 297085, 297117, 297118, 297119, 297123, 297124, 297128, 297129, 297132, 297133, 297193, 297194, 297196, 297218, 297219, 297221, 297222, 297278, 297310, 297312, 297315, 297317, 297363, 297366, 297367, 297372, 297379, 297380, 297405, 297408, 297413, 297414, 297415, 297441, 297442, 297446, 297450, 297451, 297452, 297479, 297481, 297483, 297512, 297537, 297540, 297541, 297542, 297544, 297558, 297588, 297590, 297595